

A Near-Infrared Spectroscopic Survey of Class I Protostars

Michael S. Connelley¹

University of Hawaii, Institute for Astronomy, 2680 Woodlawn Dr., Honolulu, HI 96822

Thomas P. Greene¹

NASA Ames Research Center, M.S. 245-6, Moffett Field, CA., 94035

ABSTRACT

We present the results of a near-IR spectroscopic survey of 110 Class I protostars observed from $0.80\ \mu\text{m}$ to $2.43\ \mu\text{m}$ at a spectroscopic resolution of $R=1200$. This survey is unique in its selection of targets from the whole sky, its sample size, wavelength coverage, depth, and sample selection. We find that Class I objects exhibit a wide range of lines and the continuum spectroscopic features. 85% of Class I protostars exhibit features indicative of mass accretion, and we found that the veiling excess, CO emission, and Br γ emission are closely related. We modeled the spectra to estimate the veiling excess (r_k) and extinction to each target. We also used near-IR colors and emission line ratios, when available, to also estimate extinction. In the course of this survey, we observed the spectra of 10 FU Orionis-like objects, including 2 new ones, as well as 3 Herbig Ae type stars among our Class I YSOs. We used photospheric absorption lines, when available, to estimate the spectral type of each target. Although most targets are late type stars, there are several A and F-type stars in our sample. Notably, we found no A or F class stars in the Taurus-Auriga or Perseus star forming regions. There are several cases where the observed CO and/or water absorption bands are deeper than expected from the photospheric spectral type. We find a correlation between the appearance of the reflection nebula, which traces the distribution of material on very large scales, and the near-IR spectrum, which probes smaller scales. All of the FU Orionis-like objects are associated with reflection nebulae. The spectra of the components of spatially resolved protostellar binaries tend to be very similar. In particular both components tend to have similar veiling and H₂ emission, inconsistent with random selection from the sample

¹Visiting Astronomer at the Infrared Telescope Facility, which is operated by the University of Hawaii under Cooperative Agreement no. NNX08AE38A with the National Aeronautics and Space Administration, Science Mission Directorate, Planetary Astronomy Program.”

as a whole. There is a strong correlation between [Fe II] and H₂ emission, supporting previous results showing that H₂ emission in the spectra of young stars is usually shock excited by stellar winds.

Subject headings: surveys, stars:formation, stars: pre-main sequence, infrared: stars, techniques: spectroscopic

1. Introduction

Pre-main sequence stars have been classified by the slope of their spectral energy distributions (Adams et al. 1987, Lada 1990), which traces the temperature and distribution of circumstellar material around the young star. Among these, the T Tauri (Class II) stars are the best characterized. They are optically visible, allowing many to have been discovered and spectroscopically studied since they were first identified as pre-main sequence stars (e.g. Walker 1956, Herbig 1962). The Class I objects are characterized by having increasing flux density with wavelength in the infrared due to their circumstellar envelope and disk, and are optically obscured. Comparatively few Class I objects are known, and they have only been studied in detail with the development of infrared array detectors. Most recently, Evans et al. (2009) characterized the YSO population, including many Class I objects, in five nearby star forming regions. Similarly, Enoch et al. (2009) identified 89 Class I YSOs using 1.25 μm to 1.1 mm data. Whitney et al. (2003) and Robitaille et al. (2006) showed how observables such as the SED, color, and polarization could be used to differentiate between YSOs at different viewing angles as they physically evolve. These results are the basis of a relatively new (van Kempen et al. 2009) classification sequence based on the physical characteristics of the YSO rather than its observational properties (e.g. SED, extinction, etc.).

Although SEDs measured over a wide range of wavelengths are useful for general characterization of YSOs with their disks and envelopes, they do not probe in detail the region of the inner disk where the star and disk interact. Near-IR observations are sensitive to light from the protostellar photosphere, thermal emission from the warm (~ 1000 K) inner disk, as well as high excitation atomic and molecular transitions. Several of these transitions are used to probe the accretion onto the star (e.g. atomic hydrogen) as well as the wind and outflow (e.g. [Fe II] and H₂), whereas others are sensitive to the temperature structure of the disk (e.g. CO, Calvet et al. 1991). Greene & Lada (1996) presented the first large near-IR (1.15 μm - 2.42 μm) spectroscopic survey of pre-main sequence stars, including a number of Class I YSOs. They also observed FU Orionis-like stars, characterized by deep CO and water vapor absorption bands and without photospheric absorption lines (see section

7.4). They showed how extinction affects the appearance of the spectrum, and how gravity affects separate Class I YSOs and FU Orionis-like stars from Class II and III objects by comparing the equivalent widths of Na I + Ca I versus CO. The study by Reipurth & Aspin (1997) showed in all cases that the spectra of Herbig-Haro outflow sources are highly veiled, and in several cases the spectra are similar to FU Orionis-like stars. Recently, new instrumentation has become available to observe the near-IR spectra over a wider bandwidth at higher spectral resolution. Beck (2007) used 5 different methods to estimate the extinction from the spectrum of 10 Class I and flat-spectrum protostars, resulting in widely different solutions, and she demonstrated that estimating the extinction for embedded protostars requires great care. She also estimated the spectral types of 5 protostars, and showed that the spectra of embedded protostars are characterized by a strong water ice absorption band from $2.9\ \mu\text{m}$ - $4.0\ \mu\text{m}$. Muzerolle et al. (1998) also noted the importance and difficulty of accurately estimating the extinction to highly extincted sources.

Connelley et al. (2008a) presented a new sample of Class I YSOs selected from the IRAS database to have increasing flux with wavelength, be nearby, and be optically obscured. We observed the near-IR spectra of Class I YSOs selected from this sample to address a number of questions. What are the spectral types of Class I YSOs? What fraction of Class Is are accreting, and how does this compare to T Tauri stars? What is the extinction and veiling of these objects? Connelley et al. (2008b) found that a large fraction of these protostars are binaries. Are the spectra of protostellar binaries related, as they often are for T Tauri stars (Monin et al. 2007)? What can we learn about the interaction between the star and disk by observing the relationships between various emission lines? We discuss our sample selection and observations in §2. The atlas of Class I spectra is presented in §3. We discuss specific spectral line features of circumstellar origin in §4. We discuss our method to estimate the spectral type of each protostar in §5, and in §6 we examine our methods of estimating extinction. We discuss our results in §7, and present commentary on selected targets in §8.

2. Sample and Observations

We observed a sample of Class I YSOs selected from the sample of Connelley et al. (2008a). These objects were selected from the whole sky and not limited to previously known star forming regions. They were selected to have increasing flux density in Janskys with wavelength through the IRAS bands ¹, to be in regions of nearby high optical extinction,

¹Since spectral index is defined as $-d(\log\nu F_\nu)/d(\log\nu)$, it is possible for a source to have increasing flux density with wavelength yet still have a negative spectral index

and in most cases to have a red ($H-K \gtrsim 1$) near-IR counterpart observed by 2MASS. Since our observations were conducted at the NASA IRTF, we selected objects that are within the declination limits of the IRTF ($\delta < +70$) and that rise above 2 airmasses from Mauna Kea ($\delta > -40$), which excluded 38 of 242 targets. In contrast to the study of Connelley et al. (2008a), which is focused on imaging, spectroscopy requires brighter targets to get a high signal to noise observation in a reasonable amount of time. Our goal was to get a $S/N \approx 300$ spectrum for each target, which limited our selection of targets to sources brighter than $K \sim 12$. The remaining sample included 124 targets brighter than $K=12$ and within the telescope’s declination limits. We also observed targets that have an $H-K$ color of ~ 1 or greater to ensure that each target is deeply embedded. Our $K \sim 12$ magnitude limit excluded many of the deeply embedded, and thus very young, objects presented in Connelley et al. (2008a) as none of the objects in Connelley et al. (2008a) with a spectral index greater than 2.12 is brighter than $K=12$.

We observed a total of 110 sources, which are listed in Table 1. This is the first time that infrared spectra of many of these sources have been published. While these sources were all selected to be Class I YSOs by Connelley et al. (2008a), at least four are well known as T Tauri stars. Objects with a negative spectral index (Table 1) may be regarded as Class II (T Tauri) stars. The fact that there are a few well known T Tauri stars in this sample informs us as to the usefulness of these definitions near the Class I/II boundary. Also, Class I state is observationally defined, and does not necessarily reflect the physical state of the YSO. Since the known T Tauri stars satisfied our selection criteria, they have been left in the analysis. When applicable, results are presented in Section 6 with these four T Tauri stars removed from the sample. Some of the objects presented here are the binary companions to Class I YSOs, and may not be Class I objects themselves. Higher angular resolution mid- and far-IR surveys will better distinguish embedded YSOs from nearby T Tauri stars. Caution is advised as some targets have known close binary companions (Connelley et al. 2008a) that are unresolved with the angular resolution of IRTF/SpeX, and light from both components are included in the spectrum. Fifteen such objects are flagged in Table 1. An unknown number of targets have unresolved binary companions.

The distribution of the spectral indices of these targets, based on IRAS data from $12 \mu\text{m}$ to $100 \mu\text{m}$, is shown in Figure 1. The figure shows the spectral index distribution for targets in the Taurus-Auriga and Perseus star forming regions in red, which has a mean spectral index of +0.39. The spectral index distribution for targets in the Orion and Ophiuchus star forming regions are also shown in gray, which has a mean spectral index of +0.64. These two distributions are more than 97.5% likely to be from different parent populations. The median spectral index of this sample of Class I objects is +0.50 and the average is +0.55. In comparison, the sample observed by Connelley et al. (2008a) had a

median spectral index of +0.79 and included targets with spectral indices greater than 3. The spectroscopically observed sample presented here has a lower median spectral index and includes no objects with a spectral index greater than +2.12. The bolometric luminosities in Table 1 were calculated using the IRAS fluxes using the expression in Connelley et al. (2007). In many cases there are multiple protostars within the IRAS beam, all contributing to the observed IRAS fluxes. As such, the calculated bolometric luminosity may be greater than the bolometric luminosity of the individual protostar that we observed.

Each object was observed with the 3.0 m IRTF on Mauna Kea, Hawaii with SpeX (Rayner et al. 2003) in the short cross-dispersed mode, which covers $0.8\ \mu\text{m}$ to $2.45\ \mu\text{m}$ in each exposure. There is a gap in wavelength coverage between $1.82\ \mu\text{m}$ and $1.88\ \mu\text{m}$, corresponding to a wavelength range where the atmosphere is relatively opaque. Several of the spectra in Appendix A are shown with a gap between $1.38\ \mu\text{m}$ and $1.41\ \mu\text{m}$ where the spectra are typically very noisy due to the opacity of the atmosphere in that wavelength range. We used the $0''.5$ wide slit, which gives a resolution of $R=1200$. The star was nodded along the slit, with two exposures taken at each nod position. The individual exposure times were limited to two minutes to ensure that the telluric emission lines would cancel when consecutive images taken at alternate nod positions were differenced. An A0 telluric standard star was observed after at least every other protostellar target for telluric correction, usually within 0.1 airmasses of the target.

An argon lamp was observed for wavelength calibration and a quartz lamp for flat fielding. An arc/flat calibration set was observed for each target/standard pair. The SpeX data were flat fielded, extracted, and wavelength calibrated using *Spectool* (Cushing et al. 2004). After extraction and wavelength calibration, the individual extracted spectra were coadded with *xcombspec*. *Xtellcor* was then used to construct a telluric correction model using the observed A0 standard, after which the observed spectrum of the target was divided by the telluric model. Finally, *xmergeorders* was used to combine the spectra in the separate orders into one continuous spectrum. These are all IDL routines written by Cushing et al. (2004) to completely reduce SpeX data. Spectral line flux, equivalent width, and FWHM were measured using the SPLOT routine in IRAF.

3. Spectral Type Determination

Among the most important properties of any star is the effective temperature or spectral type. We were able to measure enough photospheric absorption lines in 50 YSOs (45% of the sample) to be able to estimate the spectral type of the star based on these photospheric features alone. We used these results to estimate the photospheric spectral type distribution,

to determine if there is any trend of spectral type with spectral index, and if there is any regional dependence on spectral types.

To estimate the photospheric spectral type of each protostar, we first measured the equivalent widths of 51 photospheric absorption lines (with uncertainties) in the spectrum of each Class I YSO. These lines were chosen so that some would have a high equivalent width for any given spectral type. We also measured the EWs of these 51 lines (with uncertainties as well) for several stars selected from the SpeX near-IR spectral library (Cushing et al. 2005). Of these 51 lines, our program only considers lines in the YSO spectrum with a signal-to-noise ratio greater than a specified value, typically 2. To take into account the effect of veiling (excess continuum emission that appears to weaken spectral lines), we de-veiled the EW measurements from each protostar by using a grid of veiling temperatures and values of r_k (the ratio of the veiling flux divided by the continuum at K-band). We modeled the veiling emission as a single-temperature blackbody. To estimate the relative likelihood that the two EW measurements (one from the YSO and the other from the library star) match for a given line, we take the integral of the product of two Gaussian functions where the median of each Gaussian is the EW measurement and the standard deviation is the uncertainty in the EW measurement. This results in a relative “goodness-of-fit” parameter between each de-veiled line and each spectral standard line. We then compared the median value of this “goodness-of-fit” parameter for all of the lines for each of the spectral types we considered. Thus the spectral type with the highest median “goodness-of-fit” parameter is the best-fit spectral type for the protostar. If the goodness-of-fit parameter for a given spectral class is greater than half of the best-fit value, then we consider that spectral class within the reasonable range of possible spectral types for that YSO. The results of this spectral type matching are presented in Table 2. This procedure takes into account the S/N ratio of the observations, how precisely we could measure each line’s EW, and the wavelength dependence of the veiling even though the amount of veiling or veiling temperature are not well known. Indeed, we use the result of this absorption line EW matching code to constrain r_k in the cases where we estimate the protostellar spectral type. We note that since the EW of a line is unaffected by extinction, the uncertainty in the extinction to each protostar does not directly affect the accuracy of our spectral type estimate.

The results presented in Table 2 show that the uncertainties in the spectral type estimates vary widely. This is caused by the spectra of the targets themselves rather than the code being unable to distinguish between stars of different spectral types. In order to test the code’s precision, we gave the code the EW values for one of the SpeX library standard stars plus an error. This error was randomly chosen from a normal distribution with a FWHM of the EW’s error bars as measured from the standard star’s spectrum observed with SpeX. The code correctly identified the spectral type of the star with an uncertainty

of ± 1 sub-class. A few of the spectral type estimates of Class I targets approach this precision, but most do not. In some cases, the “goodness-of-fit” versus spectral type curve is double peaked. The precision of the match could be affected by flux from an unresolved binary companion. There are 15 known cases where light from both components of a close binary are included in the spectrum, but there are also an unknown number of cases where the target is an unresolved binary. Since our spectral type estimating routine only uses the EWs of narrow photospheric lines and does not use broad molecular features, circumstellar material could also affect the results of our matching only if that circumstellar spectrum has narrow “photospheric” lines characteristic of a different effective temperature than the central protostar. Also, some photospheric lines, such as from alkali metals, are known to be pressure sensitive (Kirkpatrick et al. 2006). The lines they observed in a young brown dwarf had EW values different than expected based on the effective temperature of the star. Thus, pressure sensitive lines may also reduce the precision of the spectral type matches for our Class I YSOs since protostars have lower gravity than the dwarf stars in the SpeX library.

Although our spectral type estimates may have poor precision in some cases, comparison with spectral type estimates from other studies shows general agreement. White & Hillenbrand (2004) used $R=34,000$ optical spectra and Doppmann et al. (2005) used $R=18,000$ spectra at $2\ \mu\text{m}$ to estimate the spectral type of a number of embedded protostars. There are six targets where we can compare our spectral type estimate with the estimate from one of these studies. In all cases, the our spectral type estimate agrees with the estimate in one of the above mentioned papers within the mutual uncertainties.

Figures 2 and 3 show two presentations of our sample’s spectral type distribution. We created Figure 2 by simply averaging the goodness-of-fit versus spectral type results (normalized by the peak value for each star) for each YSOs where we were able to estimate the spectral type, creating the mostly likely spectral type distribution for the sample. Figure 3 shows the histogram of the best-fit spectral types for each star. Both figures show that approximately half of the YSOs in our sample are M class stars, but there are a number of stars of earlier spectral types as well. The A class was a very poor fit for most stars, resulting in the low value in Figure 2, but this is the best-fit spectral class for 3 targets (all in Orion). Since we do not have near-IR B-class stellar spectral templates for comparison, we do not know if any of our targets would be best-fit by a B-class spectrum. Although *no* star had a best-fit spectral class from M5 to M7, most stars had a low but non-zero probability of being M5 to M7, again resulting in a low value in Figure 2. The reason for having no best-fit spectral class later than M4 could be due to there being no proto-brown dwarfs in the sample, a possible effect of selecting our sample from IRAS (based on the Baraffe et al. (2002) models, a star with an M4 spectral type at 1 Myr age would have a mass of $0.2\ M_{\odot}$ and would have an apparent K magnitude without extinction of 10.1 at the distance

of the Orion star forming region, well within our $K < 12$ apparent brightness limit). Another possible reason is that the photospheric line EWs for main sequence dwarfs in the M5 to M7 spectral classes may poorly match the EWs for protostars with this range of effective temperatures due to an effect such as lower gravity.

Class I protostars are expected to be descending the Hayashi track at a nearly constant effective temperature. As such, the effective temperature is largely set by the mass of the protostar. Half (21/42) of the stars with spectral type estimates have best fit spectral types from M0 to M4 (T_{eff} from ~ 3800 K to ~ 3100 K). According to the models presented by Baraffe et al. (1998) at an age of 1 Myr (likely older than our targets), these spectral types correspond to masses from $\sim 1.0 M_{\odot}$ to $\sim 0.3 M_{\odot}$. Models presented by Baraffe et al. (2002) showed that the effective temperatures do not significantly change much in this mass range at ages earlier than 1 Myr, nor do they strongly depend on the initial gravity of the protostar.

We observed that a number of targets have CO absorption in excess of what is expected from a M4 dwarf star, which is the latest class to be a best fit to any target in the sample. To determine if the excess CO absorption we observed was due to the star belonging to a high luminosity class (I, II, or III), we compared our observations with EW measurements of M-class dwarf and giant stars. In most cases, the EWs from the dwarf stars were the best fit. Figures 4 and 5 plot the equivalent width of Na I and Ca I versus the equivalent width of CO as a probe of the gravity of each star. Most of our targets lie near the dwarf locus on this plot, and away from the giant locus. The addition of veiling pushes the equivalent width measurements towards (0,0). Due to the location of our targets on this figure, we conclude that the excess of CO absorption is not due to the targets being from a high luminosity class. Section 6.4 discusses these objects further.

4. Circumstellar Line Features

This section discusses the observed properties of emission and absorption lines of circumstellar origin. Several of these lines are associated with the mass accretion process, and thus are correlated with Br γ emission, a common mass accretion tracer (Muzerolle et al. 1998). The relationships between Br γ emission and other circumstellar lines are discussed in the sub-sections associated with those lines. The frequency of common circumstellar emission and absorption lines are summarized in Table 3. The equivalent widths of the emission lines discussed in this section are tabulated in Table 4.

The amount of veiling contributed by infrared excess emission from circumstellar material is seen to vary widely from object to object in this spectroscopic atlas. Many objects

show no evidence of veiling, whereas the veiling is so high in many others that no spectroscopic features from the protostellar photosphere are apparent. Since the amount of veiling is difficult to precisely constrain, we have divided our sample into two veiling groups for much of our following analysis. Objects where the veiling is low enough to allow photospheric lines to be observable are described as “low veiling”. Objects where the veiling is high enough so that no photospheric lines are apparent are described as “high veiling”. The amount of veiling necessary to obscure photospheric lines is dependent on the photospheric spectral type since an A-type star has deep, broad hydrogen absorption lines that are easier to see despite veiling emission compared to the narrow metal lines in the spectrum of an M-star. For example, the highest veiling measured for an M-type star is $r_k = 1.6^{+1.1}_{-1.6}$ whereas the highest veiling measured for an early type star is $r_k = 8.8^{+4.8}_{-3.2}$. Since late-type stars are the most common in this sample, objects with high veiling are likely to have $r_k \gtrsim 5$. Our procedure for determining spectral types and quantitatively measuring the veiling, when possible, are described in Section 3.

4.1. Ca II Infrared Triplet

Ca II has a well known near-infrared triplet line at 8498 Å, 8542 Å, and 8662 Å. Ca II emission is likely produced in the protostellar magnetospheric infall of gas (Azevedo et al. 2006) and thus is a useful accretion tracer. If the lines are optically thick, the line flux ratios should be 1:1:1 since these lines are very close in wavelength. Detailed modeling by Azevedo et al. (2006) shows that the line ratios are typically 1.1-1.2, but can be as large as 1.5. High resolution spectra of ~ 90 T Tauri stars, and found that the shortest wavelength line of the triplet tends to have the highest peak and also tends to be the narrowest of the lines (Hamann & Persson 1990). CiteWhi2004 presented high resolution spectra of this line for a large sample of T Tauri and Class I stars, showing the Ca II line profiles range from being very narrow to having a FWHM up to 250 kms^{-1} .

Although only 20 Class I YSOs ($18\% \pm 4\%$) showed Ca II emission, 20/33 ($61\% \pm 14\%$) targets with detectable flux in I-band have Ca II emission, making Ca II a very common (although rarely observed) emission feature for Class I YSOs. Being associated with mass accretion, and specifically magnetospheric infall, Ca II emission is strongly associated with HI Brackett (Br) γ . All targets that have Ca II emission also show emission from Br γ , but 20/25 targets with a detected continuum at I-band and Br γ emission also have Ca II emission. Thus, $\sim 20\%$ of targets have Br γ emission but no emission from Ca II. In terms of equivalent width (EW), Ca II is the strongest emission line observed from Class I protostars.

We also found that the EW ratios of the Ca II infrared triplet can deviate significantly

from 1:1:1 line ratios. The mean ratio for $EW_{8498} / EW_{8542} = 1.1$, but ranges from 1.8 to 0.8. Similarly the mean ratio for $EW_{8498} / EW_{8662} = 1.3$, but ranges from 1.9 to 0.8. Gamiero et al. (2006) observed a similar range of line ratios in the EWs of the Ca II lines for DI Cep, showing that these ratios are also variable. Azevedo et al. (2006) note that variation in the gas temperature and mass accretion rate of their models do not completely account for this variability.

4.2. He I

The He I line at $1.0833 \mu\text{m}$ is seen in both absorption and emission from many young stars. The line profile is sensitive to the kinematics of the stellar wind (Dupree et al. 1992). Edwards et al. (2006) presented observations of 38 He I line profiles from T Tauri stars observed at a spectral resolution of $R=25,000$, and demonstrated that young stars have a wide diversity of inner wind properties. In comparison, our data have much lower spectral resolution ($R=1,200$, $\delta v \sim 250 \text{ km s}^{-1}$). Details of the line profiles of He I will be discussed in a future paper.

The He I line was detected in 35 of our Class I YSOs. This comprises 32% of the whole sample, and 52% (35/67) of the targets where there was enough flux at J-band to detect the continuum. Among the He I lines detected, 69% (24/35) of the He I lines show sub-continuum absorption, and emission is seen in 77% (27/35) of them. Note that objects with He I absorption can also simultaneously have He I emission. We see deep He I absorption from the three FU Orionis-like stars where we detected the J-band continuum. Data from T Tauri stars show that the wind accelerating region is very close to the stellar photosphere, and is possibly the stellar corona (Edwards et al. 2006). However, the flux from FU Orionis-like stars is likely dominated by light from the disk (Hartmann & Kenyon 1985), yet we still see strong He I absorption, suggesting that in these cases the wind originates from the disk. The He I features for *all* of the FU Orionis-like stars in the sample show only strong blue-shifted absorption (i.e. no emission or non-blue-shifted absorption). Thus, we propose that this is a possible way to indicate if a candidate star is an FU Orionis-like star. However, some other stars also have a He I feature that shows only blue shifted absorption despite not sharing other spectroscopic features with FU Orionis-like stars, so this criterion cannot be used alone.

4.3. [Fe II] and H₂

In this analysis we consider the [Fe II] line at 1.644 μm and the H₂ line at 2.122 μm . Both [Fe II] and H₂ are well known tracers of winds via shock induced emission. Emission from these species is often seen far from the stellar source in Herbig-Haro flows. The excitation mechanism for H₂ within a few hundred AU of a young star remained poorly understood until recently. Possible excitation mechanisms include UV (either from the accretion flow onto the star or from the star itself), X-rays from the star’s corona, or shocks from the wind. Beck et al. (2008) found that the properties of the H₂ emission (e.g. the emission morphologies and spatial extent) are most consistent with shocked excitation from the wind rather than excitation of gas by radiation from the central star. [Fe II] emission is a very useful probe of winds, especially in regions where the extinction is high enough to preclude optical observations (Bally et al. 2007). [Fe II] emission probes high excitation temperature (11,000 to 12,000 K) winds, and in particular fast ($>30 \text{ km s}^{-1}$) dissociative J-shocks (Reipurth et al. 2000).

The study by Beck et al. (2008) was based on observations of 6 Classical T Tauri stars. We seek to determine if H₂ emission from Class I protostars is also shock excited. The [Fe II] and H₂ lines are also often observed in the spectra of Class I protostars, with 44/107 targets having [Fe II] emission and 47/110 having H₂ emission. Among the 44 Class I objects that show [Fe II] emission, 35 ($80\% \pm 13\%$) also have H₂ emission. The probability that a random sampling of 44 spectra from this data set would yield 35 or more objects with H₂ emission is less than 10^{-6} . Considering the strong correlation between the presence of [Fe II] and H₂ emission, we conclude that H₂ emission from Class I YSOs is also likely to be excited by shocks in winds.

Figure 6 shows that there appears to be a weak trend of increasing [Fe II] equivalent width with increasing H₂ EW. *All* targets with an H₂ EW less (stronger emission) than -3 \AA also show [Fe II] in emission, provided there was enough flux to observe the H-band continuum. With two exceptions, all targets with [Fe II] EW less than -2 \AA have H₂ emission. With one exception, only targets with high veiling have an [Fe II] EW less than -7 \AA .

Figure 7 shows that the Br γ and H₂ EWs appear to be related by a weak (the correlation coefficient is 0.03) inverse relationship. Targets with strong Br γ tend not to have strong H₂ emission and vice versa. Only targets with high veiling have strong emission from H₂ (EW $< -7 \text{ \AA}$) or Br γ (EW $< -9 \text{ \AA}$). It may be possible that higher mass accretion rates onto the star suppress the H₂ excitation mechanism. However, since H₂ emission is believed to be shock excited in the wind (Beck et al. 2008), which is accretion driven, this scenario seems unlikely. Another possibility is that the H₂ line flux is not dependent on the mass accretion rate, and that the higher veiling associated with higher Br γ EWs reduces the observed H₂

EW. However, as stated above, only targets with high veiling have strong emission from H_2 , contrary to this scenario. Increasing veiling will tend to push the EW values towards (0,0) in Figure 7 (and in Figure 6 as well). Although many data points are near the origin of the figure, they are predominantly targets with low veiling. We also note that no early type star where Br γ is seen in absorption shows H_2 emission. Spectroscopic monitoring should show if the variability of the Br γ and H_2 lines are correlated or independent of each other.

We observe that the line EWs for H_2 and [Fe II] are stronger in targets with high veiling. Objects with high veiling might be expected to have greater Br γ luminosities since both are well known accretion tracers. Since the wind is powered by accretion, it would also be expected that targets with high mass accretion would have stronger winds. However, if both Br γ and veiling are accretion tracers, then why is there an inverse relationship between H_2 and Br γ EWs? These correlations show that the H_2 and [Fe II] lines, which are from the shocks in the wind, are not proportional to the instantaneous mass accretion rate (traced by Br γ). Since atomic hydrogen is only ionized very close to the star whereas H_2 traces colder more distant gas, the source of these lines are not co-located. Also, we speculate in section 6.4 that it may be possible that the mass accretion rate is quite high in the cases where there is strong H_2 and [Fe II] emission, but that the Br γ emission mechanism has collapsed resulting in relatively lower Br γ emission with increased mass accretion rate. We stress that this result is applicable to the region immediately around the central star, and not for an extended outflow. The width of our $0''.5$ slit corresponds to a range of ~ 70 AU at the distance of the Taurus star forming region and ~ 230 AU at the distance of the Orion star forming region.

4.4. CO

We have found that $23\% \pm 5\%$ (25/110) of our targets show the CO band heads in emission. This is very close to the value for HH sources found by Reipurth & Aspin (1997) of 20%. Targets that show CO in emission tend to have high veiling such that no photospheric absorption lines are apparent. Of the targets that show CO in emission, $91\% \pm 20\%$ (21/23) have high veiling whereas $9\% \pm 6\%$ (2/23) have low veiling. Although 2 stars have CO emission and low veiling, these two stars are both early type stars, one of which has veiling that is low enough that the H I lines can be seen at shorter wavelengths but high enough to almost completely veil the Brackett series of lines ($r_k = 8.8$ for IRAS 05513–1024). Targets with CO emission more often have high veiling than the sample as a whole, for which $55\% \pm 7\%$ (61/110) show high veiling.

We have found that the CO and Br γ features are closely related (the correlation co-

efficient of their EWs is 0.44). Figure 8 plots the EW of CO versus Br γ , and is divided into three parts. Region A includes all objects where CO is seen in emission. CO equivalent widths that are consistent with absorption from the photosphere of a dwarf star are included in region B, from early type stars with no CO absorption to M4, the latest type in our sample (see Section 3). The CO absorption in region C is in excess of what is expected to be observed from the photosphere of a dwarf star. This figure shows that targets with CO in emission also *always* show Br γ emission (an important tracer of magnetospheric accretion) and almost always have high veiling (red symbols) as well. Figure 8 shows a general trend of greater CO emission with greater Br γ emission, but with significant scatter. Br γ is often seen in emission when the CO absorption is consistent with a dwarf stellar photosphere (region B) and when the veiling is low (black symbols). There is a trend of increasing Br γ emission with decreasing CO band head absorption, possibly due to CO and/or veiling emission increasing as the mass accretion rate increases. Notably, Br γ *never* shows significant emission when the CO is in absorption beyond what is consistent with the star’s spectral type. This situation is most commonly seen among FU Orionis-like stars (see section 6.4), which also have high veiling.

We interpret this relationship between CO and Br γ as follows. When CO and Br γ are in emission and the veiling is high, the accretion rate is quite high. The surface of the disk is hotter than the disk midplane, accounting for the CO emission (Najita et al. 1996) and the lack of any absorption features from the disk. At lower accretion rates, Br γ is still seen in emission. The veiling is low enough that photospheric absorption bands dominate the CO feature. The low veiling suggests that the warm (> 1000 K) emitting surface area in the disk is relatively low. In contrast, FU-Orionis like stars are believed to be experiencing a burst of mass accretion. Strong CO absorption is observed from FU Orionis-like stars. Muzerolle et al. (1998) empirically derived the well-used relationship between Br γ emission and mass accretion rate with observations of T Tauri stars. Although FU Ori-like objects have very high accretion luminosities and thus very high mass accretion rates (up to $10^{-4} M_{\odot}\text{yr}^{-1}$ (Hartmann 2000)), they lack many of the usual mass accretion signatures commonly observed from T Tauri and many other Class I YSOs (e.g. Br γ or Paschen β emission). Br γ is not detected in some of the FU Ori-like objects (04073+3800, 18270–0153W, 20568+5217, and 22051+5848) and only very marginally detected in the rest, as seen in region C of Figure 8. These observations show that the established relationship between observed Br γ emission versus mass accretion rate is not valid for these objects. As such, FU Ori-like objects may accrete mass via a different mechanism than the magnetospheric funnel flows that produce the well known Br γ emission in Class I and T Tauri stars with lower mass accretion rates. It is possible that Br γ emission is proportional to the mass accretion rate at relatively low mass accretion rates, but the proportionality breaks down as

mass accretion rate increases to the point where at very high mass accretion rates there is no observed Br γ emission. We postulate that the magnetosphere, which shapes the accretion flow for classical T Tauri stars, collapses when the accretion rate is as high as is found among FU Orionis objects. For further discussion of FU Orionis-like objects, see section 6.4.

Figures 4 and 5 show the relationship between CO emission/absorption and Na I + Ca I. The FU Orionis-like objects in our sample lie in region E, below and to the right of the luminosity class III stars. A number of objects have sufficiently high mass accretion to push CO into emission, and these objects are located in region F of Figure 5. Absorption from Na I + Ca I is photospheric. However, Na I has also been observed in emission in many of these cases when veiling is high, resulting in occasionally negative values for the EW of (Na I + Ca I). Ca I was never seen in emission.

CO emission and absorption trace gas at a moderate temperature (a few 1000 K) and high density ($n_H > 10^9 \text{ cm}^{-3}$), however there are several potential excitation mechanisms. Figure 7 in Calvet et al. (1991) shows that young stars with a mass accretion rate below $\sim 10^{-7} \text{ M}_{\odot} \text{ yr}^{-1}$ can have CO in emission due to stellar radiation heating of the disk surface or CO in absorption from the stellar photosphere. If this model is correct, then we should expect our sample to have many YSOs that are accreting mass (judging from their Br γ emission), have low veiling (suggesting a low mass accretion rate), with some YSOs showing CO in absorption and others showing CO in emission. Although we observed many examples of YSOs with low veiling and CO in absorption, CO emission is usually only observed when the veiling is high and thus presumably when the mass accretion rate is high. Also, Figure 7 in Calvet et al. (1991) predicts that early type stars should have CO emission when the mass accretion is as high as $10^{-5.5} \text{ M}_{\odot} \text{ yr}^{-1}$. Two of the eight early type stars in this study have CO in emission, whereas 6/8 have no CO emission or possible CO absorption (4 of these also have atomic hydrogen emission showing that they have a disk and are actively accreting mass). Both of the early type stars with CO emission also have high veiling, suggesting that the presence of CO emission is correlated with high veiling and not with the spectral type of the central star. Calvet et al. (1991) also predicted that high mass accretion rates push the CO into absorption, as observed with FU Orionis-like stars. Martin (1997) proposed that the CO emission could be from the magnetospheric funnel flow of mass onto the star. If this hypothesis is correct, then multi-epoch observations should show that the CO band head flux should vary in step with other mass accretion tracers related to the funnel flow, such as Br γ or Ca II emission. More recently Glassgold et al. (2004) concluded that CO emission arises in a thick layer near the surface of the disk where atomic hydrogen collisionally excites the CO. Velocity resolved observations can also help to determine the location of the source of the CO emission.

5. Extinction Estimation

An accurate estimate of the extinction along the line of sight to each protostar is very important for deriving many properties of a YSO (e.g. luminosity, emission line fluxes, and properties derived from these). This is particularly challenging in the case of Class I YSOs that suffer from very high extinction, and where much of the observed flux may be scattered light as shown by the high fraction of candidate Class I YSOs with a reflection nebula (Connelley et al. 2007). Scattered light will cause a YSO to appear bluer, potentially leading to the extinction to be underestimated. Our estimate of the extinction starts with using a power law of the extinction versus wavelength based on empirical data. We used the results from Nishiyama et al. (2009), who found that the J through K-band extinction is well fit by the power law $A_\lambda \propto \lambda^{-2.0}$. They also derived values for the extinction for the 2MASS pass bands, allowing us to use 2MASS photometry to estimate extinction. Their result is based on observations of lines of sight towards the Galactic center. We note that the extinction law in star forming dark clouds may be different (e.g. Román-Zúñiga et al. 2007).

Extinction can be estimated in several ways. We used 2MASS JHK broad-band colors, modeling of the continuum, and emission line ratios to estimate the extinction to the targets in our sample. Not all methods could be applied to every target, and no method is perfect. Shocked emission lines from the outflow can be used, but they are seen through a different line of sight than the protostar even if the shocked emission is not spatially resolved. Our derived extinction values are summarized in Table 2.

5.1. Broadband Colors

We first used 2MASS J, H, and K band photometry of our targets to estimate the extinction to our targets. We used the values of A_λ/A_K from Table 1 from Nishiyama et al. (2009). With these values, we reddened the 2MASS colors of our targets to the T Tauri locus derived by Meyer et al. (1997). 2MASS did not detect some of our targets in J or H-band, so we were not able to estimate the extinction to all sources based on 2MASS photometry.

Although this method of estimating the extinction is very simple, it has several caveats. 2MASS observations cannot resolve close binary stars, so this method is not applicable to close binaries of comparable brightness. Scattered light from circumstellar material will make the object appear bluer and affect the derived extinction to the source. If an object is hidden behind an edge-on disk, then all of the observed flux may be scattered light. As noted above, it is very common for Class I YSOs to be associated with an infrared reflection

nebula. Table 1 flags objects where the K-band flux is likely to be dominated by scattered light (no point source is observed) or where scattered light could affect the near-IR colors (the object is associated with a reflection nebula), as judged from examining K-band images of their reflection nebulae in Connelley et al. (2007).

5.2. Continuum Modeling

We used a simple procedure to model the observed spectrum of each protostar to estimate the extinction, veiling temperature, and the magnitude of the veiling. This program adds an infrared excess (i.e. veiling emission, which we simulate as a single temperature black body) to the spectrum of a star from the SpeX spectral library (Cushing et al. 2005, Rayner et al. 2008), then applies extinction to that sum using the reddening law described above. Naturally, the result of this procedure depends on the input spectral type. When possible, we used the best fit spectral type found by our equivalent width matching program; otherwise we used an M2V spectral type since that is the most common spectral type among the stars in this sample. Each model (star plus veiling behind extinction) is compared to the observed spectrum and the RMS of the fit is calculated. The code runs through a user-defined grid of veiling temperatures, veiling amplitude (r_k), and visual extinctions (A_v) to minimize the RMS difference between the observed spectrum and the model spectrum. We used veiling temperatures from 200 K to 2000 K, which is approximately the formation temperature of chondrules and refractory inclusions in meteorites (Boss & Grahm 1993, Alexander et al. 2007). Contour plots of the RMS residual of the fit versus veiling temperature and extinction show the confidence intervals for the fitted parameters. An example of the output of our modeling code is shown in Figure 9. Our 1σ uncertainties for veiling temperature and extinction are determined by the amount by which these parameters have to change from the best fit values for the RMS of the model to be twice the best fit RMS. In many cases, we removed strong emission lines (most often atomic and molecular hydrogen, and CO) from the observed spectrum to improve the RMS fit.

The ability of our modeling code to precisely derive the extinction to the source varies greatly from target to target, and also depends on the spectral type of the template spectrum. This is reflected in the uncertainties presented in Table 2. We find that there is a degeneracy between the veiling temperature and the amount of extinction if the spectrum is dominated by a continuum that smoothly increases with wavelength, which is quite common among Class I YSOs. The amount of extinction is often very well constrained at a given veiling temperature, but good fits can often be found for a wide range of veiling temperatures and corresponding extinctions. We also find that among stars with late type spectra, the code

can often fit the observed spectrum using different amounts of veiling for different template spectra, and thus this procedure is a poor discriminator of spectral type.

Figure 10 shows the histograms for extinction based on both near-IR broadband colors and continuum modeling. Figure 11 shows that the extinction estimates based on near-IR colors tend to be $\sim 30\%$ lower than the estimates based on continuum modeling. This discrepancy may be caused by the use of different photometric systems on very red objects, or scattered light from an associated reflection nebula affecting the observed colors more than the spectra. Another difference is that the 2MASS colors deredden to the T Tauri locus whereas the continuum modeling routine more accurately takes into account the contribution of the stellar photosphere and veiling emission without scattering. Although it would not account for this systematic offset, the large uncertainties in the extinction calculated from continuum modeling mean that these estimates are often consistent with the extinction estimates based on the near-IR photometry. The median value of the extinction distribution based on continuum modeling is $12.7 A_v$ magnitudes, whereas the median value of the extinction distribution based on 2MASS photometry is $9.8 A_v$ magnitudes.

Our continuum modeling program also allowed us to derive a distribution for the veiling temperature, which peaks near 1500 K. This result is likely influenced by wavelength coverage of our data, since the peak of a 1500 K blackbody is at $1.9 \mu\text{m}$, near the middle of our wavelength coverage.

We found it very difficult to precisely constrain the amount of veiling (r_k) for most of the stars in the sample. For objects whose spectrum is dominated by veiling, we can only say that the veiling is high, likely greater than $r_k \sim 5$ since $r_k=8.8$ is the highest veiling value that we were able to meaningfully constrain. In the cases where the spectrum shows clear photospheric lines, these lines are used to constrain the veiling. In these cases, uncertainty in the estimate of the spectral type of the star limits the uncertainty of the veiling. Therefore, for much of the analysis regarding veiling, we have simply divided this sample into two groups: targets with “high” veiling and targets with “low” veiling, as defined in section 4.0.

5.3. Emission Line Ratios

If the intrinsic line ratio of a given pair of emission lines is known, the observed line flux ratio can be used to calculate the extinction to the source. Lines that have the same upper state are particularly useful since the line flux ratio only depends on the transition probabilities to the two lower states. In this case, there are no assumptions about the emitting gas being in LTE or concerns that the two lines may be being emitted by gas with

different properties (temperature, density, distance from the source, etc.). In other cases it is reasonable to assume LTE, and thus the intrinsic line ratio can be calculated.

[Fe II] emission lines at $1.644\ \mu\text{m}$ and $1.257\ \mu\text{m}$ are often seen in the spectra of young mass accreting stars. The ratio of these line fluxes has previously been used to estimate the extinction to the Cas A supernova remnant (Eriksen et al. 2009) and to make an extinction map towards an AGN (Storchi-Bergmann et al. 2009) since these two lines also share the same upper level. Reipurth et al. (2000) also discussed the use of these lines to estimate extinction. Since these lines are forbidden, they should be optically thin. As such, this pair of lines is a useful tool to estimate the extinction to a wind source. The intrinsic line ratio is not yet well constrained, as noted by Eriksen et al. (2009). Eriksen et al. (2009) used a value of $[\text{Fe II}]_{1.257} / [\text{Fe II}]_{1.644} = 1.49$, based on observations of P Cygni by Smith & Hartigan (2006). Storchi-Bergmann et al. (2009) used a value of 1.36 based on calculations (Nussbaumer & Storey 1988) verified by observations (Bautista & Pradhan 1998). For the purpose of this paper, we adopt a value of $[\text{Fe II}]_{1.257} / [\text{Fe II}]_{1.644} = 1.36$.

We observed both the $1.257\ \mu\text{m}$ and the $1.644\ \mu\text{m}$ [Fe II] lines in 25 targets. Our extinction estimation used the same reddening law as with all of the other methods we used. Generally, our extinction estimates based on the [Fe II] line ratios are consistent with the estimates based on continuum modeling, taking into account the mutual uncertainties. In the case of IRAS 04286+1801, the [Fe II] lines were the only reliable way to estimate the extinction to this target among the methods we used. In this case, the near-IR flux is dominated by scattered light, making the object appear bluer and thus leading to an underestimated extinction. Furthermore, being an FU Orionis-like object, there is no apparent flux from the photosphere or atomic hydrogen emission (see Section 6.4). Since the [Fe II] emission is from the wind, the extinction calculated from the [Fe II] line ratio may be different from the true extinction to the protostar itself. However, considering that the slit was $0''.5$ wide, the [Fe II] emission in our spectrum is very near the location of the protostar, and not from a distant part of the outflow. We note that the $1.644\ \mu\text{m}$ was occasionally on the edge of a comparably strong Br 12 absorption line or emission line. Such cases are designated with an asterisk in Table 2. Higher spectral resolution would be useful in separating these features to get a better flux measurement of the [Fe II] line.

The Br γ ($2.16612\ \mu\text{m}$) to Paschen β ($1.28216\ \mu\text{m}$) line ratio can be used as an extinction tracer assuming Case B recombination. In this case, the intrinsic line ratio is 5.75 ± 0.15 (Storey & Hummer 1995). Although most of our targets show some Br γ emission, the Pa β emission line was detected in only about a third of them, usually because of high J-band extinction and as such there being no detectable continuum at J-band. We did not extract orders for which there was no continuum flux, so in these cases we did not measure the Pa β

equivalent width. In those cases where both lines were measured, we used them to calculate the extinction to the target, and these values are listed in Table 2.

In the case of embedded protostars, the H_2 $v=1-0$ Q(3) ($2.42373 \mu\text{m}$) to S(1) ($2.12183 \mu\text{m}$) lines have been used (Beck 2007) since these two lines share the same upper state. Many of our Class I YSOs have strong H_2 emission, and we attempted to use these lines to estimate the extinction to these sources. We found that the extinction derived from these H_2 lines often greatly differed from the extinction estimates based on broad band colors or continuum modeling, and was occasionally negative. We determined that this line ratio is an unreliable extinction estimator since in 4/10 cases, this line ratio was observed to be variable. By coincidence, the $v=1-0$ Q(3) line is very close to a narrow ($\delta\lambda = 7.1 \text{ \AA}$) but opaque telluric absorption line at $2.42412 \mu\text{m}$ (in vacuum). The Doppler shift due to the Earth’s orbital motion moves this telluric line such that the $v=1-0$ Q(3) line can be either on the blue wing of the line (and thus the Q(3) line would be partially absorbed) or completely clear of it. This telluric feature as well as the H_2 lines are not resolved at the spectral resolution ($R=1200$) of our data. Thus, a significant amount of the flux of the $v=1-0$ Q(3) line may be lost to this telluric absorption feature and *not recovered* when the telluric correction is carried out during the data reduction ². This problem may be ameliorated by using sufficiently high spectral resolution to resolve this telluric absorption feature to accurately compensate for it. In the cases where the $v=1-0$ Q(3) to S(1) line ratio did not vary, the observed line ratio was used to estimate the extinction with the understanding that the extinction may be underestimated if a significant amount of the flux of the Q(3) line is lost to this telluric absorption feature.

6. Discussion

We now discuss several results revealed in the preceding analysis. We particularly examine the physical implications for our observed sample of embedded protostars.

²Consider a telluric absorption line that is narrow (and thus unresolved) but very deep. If the telluric line transmits 10% of the incident flux, then the telluric correction at that wavelength should be a factor of 10. However, since the line is unresolved, the observed depth of this line will be much less (for example, 70% transmission) and the telluric correction will be similarly less (1.4 rather than a factor of 10).

6.1. Effect of Nebulosity

Having noticed that many of the stars with FU Orionis-like spectra (see section 6.4) were associated with reflection nebulae, we investigated the connection between reflection nebulosity and the near-IR spectrum. We used the K-band images presented in Connelley et al. (2007) to classify the nebulae into three groups: strong nebulosity (no K-band point source is seen), some nebulosity (a K-band point source is seen along with a reflection nebula), or no nebulosity. The reflection nebulae have an average size of ~ 10000 AU or $\sim 20''$ on the sky. The spectra as a whole were divided into three parts: spectra with “high” veiling (no photospheric lines apparent), spectra with “low” veiling (the spectrum shows photospheric absorption lines), and spectra that are similar to FU Orionis-like stars with deep water and CO absorption and without photospheric absorption lines.

The results of our analysis are gathered in Table 5. We found that although there are only 10 targets with FU Ori-like spectra (9% of the sample), 40% of the YSOs with strong nebulosity have this type of spectrum. Furthermore, all objects in our sample with FU Ori-like spectra are associated with a reflection nebula. An exception is IRAS 06297+1021W, which we consider to be an FU Orionis-like object despite having emission lines uncharacteristic of such an object, and which is not associated with a reflection nebula. YSOs with strong nebulosity have a higher fraction of FU Ori-like spectra (6/15) than objects without nebulosity (0/54) with greater than a 99.9% confidence. We found that the fraction of objects with high veiling has no dependence on the presence or absence of a reflection nebula. However, objects with low veiling are less likely to be found among targets with strong nebulosity than objects without nebulosity with a 99.9% confidence. These binomial confidence intervals were calculated using the expressions presented by Brandeker et al. (2006) in their appendix B2. Targets without nebulosity and those with some nebulosity have similar fractions of objects with high veiling, low veiling, and FU Ori-like spectra, so these two nebulosity groups are difficult to distinguish based on their spectra. In summary, targets in this sample with strong nebulosity are less likely to have low veiling and more likely to be an FU Orionis-like star than targets with some nebulosity or no nebulosity.

These relationships show that there is a correlation between the appearance of the YSOs on large scales (> 1000 AU) and the properties of the star and inner disk at very small scales. Objects with strong nebulosity could be objects with edge-on disks that block the central star from view, in which case we would see no K-band point source and all of the light we see is scattered off of circumstellar material. This is indeed the case for many of the objects observed by White & Hillenbrand (2004), who observed objects apparently more embedded than T Tauri stars (many objects were only seen in scattered light) and observed photospheric features in all of them. If objects with strong nebulosity are merely

seen edge-on, then we would expect to observe the same fraction of objects with low veiling or FU Orionis-like spectra in all of the nebulosity groups. However, this is not what we observe. In order to not see a K-band point source, these objects must therefore be more deeply embedded on average, and presumably less evolved, than objects with some or no nebulosity. Among the objects with no reflection nebula, there may be no objects with FU Orionis-like spectra because either objects with no nebulosity are too evolved or because the increase in the luminosity of the object in the FU Orionis phase would illuminate nearby circumstellar material, creating a reflection nebula that previously was not visible.

Why are there so few objects with low veiling among objects with strong nebulosity, and so many objects with low veiling that have some or no nebulosity? The circumstellar material responsible for veiling also scatters and absorbs light, and can also obscure the central star. Objects with low veiling are most common among targets without a reflection nebula and quite rare among targets with strong nebulosity. If objects with low veiling were simply less luminous and thus do not illuminate a reflection nebula as often, then we would not see an equal number of low veiling objects among targets with some nebulosity and without nebulosity. One possible explanation is that objects with some or no nebulosity are simply more evolved, with less circumstellar material in the envelope (accounting for the optically thinner cloud, allowing us to see the central star) and less material in the inner disk (accounting for the lack of veiling emission). This would then suggest that FU Orionis objects, which are most common among targets with strong nebulosity, would be relatively less evolved.

6.2. Spectral Type Dependence on Star Forming Region

The spectral type distributions of pre-main sequence stars has been shown to have a strong dependence on the star forming region (Luhman et al. 2003). Hillenbrand (1997) compared the spectral type distributions for the Ophiuchus, Chamaeleon, Taurus/Auriga, Lupus, L1641, and Orion Nebula Cluster (ONC) star forming regions. Both the ONC and the Ophiuchus star forming regions have a number of early type stars, extending to OB in Orion and B type in Ophiuchus. However, the spectral type distribution of the ONC peaks at M3 whereas the spectral type distribution of Ophiuchus peaks earlier than M-class. The spectral type distribution for the Taurus star forming region (e.g. Briceño et al. 2002, Luhman et al. 2003, Luhman et al. 2006) peaks near K7, with most stars having spectral types from K0 to M8. While these studies found no stars in the Taurus star forming region with a spectral type earlier than G, Kenyon & Hartmann (1995) found 3 young stars in the Taurus/Auriga clouds with spectral types earlier than G.

To determine if our sample of Class I YSOs shows a spectral type dependence versus star forming region similar to the pre-main sequence studies described above, we divided our sample into two groups of roughly equal size. Group 1 consists of targets in the Taurus, Auriga, and Perseus star forming regions, and has 21 objects. These clouds are nearby, have a low stellar density and are not forming massive stars. Group 2 consists of targets in the Orion and Ophiuchus clouds, and also has 21 objects. The distributions of the best-fit spectral types are shown in Figure 3. The spectral type distributions are overall very similar. The two-sample K-S test shows that the best-fit spectral type distributions have less than a 90% chance of being drawn from different parent populations. However, Group 1 has no star with a best fit spectral type earlier than F5. In contrast, 6/21 (29%) of the stars in Group 2 are A or F stars. If the 4 known T Tauri stars are excluded, it remains true that Group 1 still has no star with a spectral type earlier than F5. Group 2 would then have 5/20 (25%) of stars with an A or F spectral type. The regions in which we found A and F type stars (Orion and Ophiuchus) are associated with well known populations of early type stars, in this case the Orion Nebula cluster and the Sco-Cen OB association. We stress that these results are based on those stars for which we could determine a spectral type, and are only applicable to the clouds as a whole assuming that protostars of each spectral type are equally likely to have low enough veiling to allow a spectral type to be estimated. We also note that the Serpens clouds have very few targets for which a spectral type could be estimated. Of the eleven targets in that region, the spectra of only two targets have photospheric absorption lines, and we could get a spectral type estimate for only one target.

6.3. Class I Accretion Fraction

An important question to address is the fraction of Class I YSOs that are actively accreting mass. Unfortunately, the fraction of mass accreting T Tauri stars has not been well characterized, in part because the result depends on the age of the T association. The fraction of T Tauri stars with IR excesses, and thus warm disks, drops from $\sim 50\%$ to $\sim 3\%$ in a survey of star clusters ranging in age from 2.5 to 30 Myr (Haisch et al. 2001a, Hernández et al. 2008). Haisch et al. (2001b) found that 65% of young stars in IC 348 have disks, whereas the younger NGC 2264 and Trapezium clusters have disk fractions of 86% and 80%. Luhman et al. (2010) found that the disk fraction of the Taurus star forming region ($N(\text{Class II})/N(\text{Class II and III})$) is $\sim 75\%$ based on 348 objects observed by Spitzer. Using this metric, the results presented by Evans et al. (2009) show that the disk fraction in Chamaeleon II is $78\% \pm 18\%$, in Lupus is $66\% \pm 9\%$, in Perseus is $89\% \pm 6\%$, in Serpens is $81\% \pm 7\%$, and in Ophiuchus is $81\% \pm 6\%$. The presence of a disk does not mean that all of these stars are accreting matter, but only that they could.

We used the presence of Br γ emission (Muzerolle et al. 1998) or high veiling (when the veiling is high enough that no photospheric absorption lines are observed, $r_k \gtrsim 5$, characteristic of a warm inner disk close to the star) to determine the fraction of our targets that are accreting matter. 93 stars show Br γ emission, whereas 8 more have high veiling but no Br γ emission (these are mostly FU Orionis-like objects). Thus $92\% \pm 9\%$ (101/110) of Class I YSOs are actively accreting matter at any given time. Excluding the 4 known T Tauri stars, the fraction of Class I YSOs accreting matter remains $92\% \pm 9\%$ (98/106).

The histogram of Br γ equivalent widths (EW) in Figure 12 has been divided between targets with high and low veiling. Targets with high veiling have a mean EW of -4.21 and a median EW of -2.93 , whereas targets with low veiling have a mean EW of -1.20 and a median EW of -1.63 . Equivalent widths are measured relative to the continuum flux, which is elevated by the veiling in the case of targets with high veiling. Thus, targets with high veiling on average have much higher Br γ line fluxes and presumably high mass accretion rates as well. For comparison, the Br γ EW histogram for the T Tauri stars with Br γ emission observed by Muzerolle et al. (1998) has been overlaid in Figure 12. The two-sample K-S test shows that there is less than a 90% chance that the T Tauri Br γ EW distribution is drawn from a different parent population than Br γ equivalent width distribution of the whole sample of Class I YSOs. Thus, the Br γ EW distributions for accreting T Tauri stars and accreting Class I protostars are indistinguishable with these data. We note that Muzerolle et al. (1998) selected T Tauri stars with previously measured mass accretion rates, so the targets they selected are not representative of T Tauri stars as a whole considering the large number of non-accreting weak line T Tauri stars. Although the Br γ EW distributions are consistent, Class I YSOs generally have higher veiling than T Tauri stars (Doppmann et al. 2005), so therefore Class I YSOs likely have a higher average Br γ line flux and presumably higher mass accretion rates.

There are 9 targets in this sample without Br γ emission or high veiling, and thus do not appear to be currently accreting matter. We have estimated the spectral types of 8 of these. Among the non-accreting Class Is, early type stars are over represented and late type stars are under represented. The two-sample K-S test shows that there is a 90% chance that the spectral type distributions for accreting and non-accreting Class I YSOs are drawn from different parent populations. Three of these 9 stars are A or F type stars. An infrared excess or Br γ emission that would be readily apparent for a late type star may be overwhelmed by the greater photospheric flux from these stars. Thus, these apparently non-accreting stars may still be accreting some matter. All targets, including the apparent non-accretors, were selected to have increasing flux with wavelength as observed by IRAS, so they all have significant circumstellar material. Non-accretors (excluding targets where there was another YSO in the IRAS beam) also tend to have a higher median spectral index than the sample

as a whole (1.3 vs. 0.5 from $\lambda = 12 \mu\text{m}$ to $100 \mu\text{m}$), suggesting that the non-accretors tend to have relatively less warm dust and more cool dust than the accretors, consistent with the scenario of a cleared disk hole.

We expected that the accretion luminosity ($L_{\text{bolometric}} - L_{\text{star}}$) would be proportional to the veiling. Accretion luminosity could only be estimated for those stars for which we have estimated the photospheric spectral type. Analysis of the bolometric luminosity (determined from IRAS observations) or the accretion luminosity showed no trend with our derived values of the veiling (r_k). There are several objects with a late type spectral classification, very high accretion luminosities, and negligible veiling. For many of these cases there are other deeply embedded YSOs within the broad IRAS beam. To show how the veiling is related to the accretion luminosity, high angular resolution mid- and far-IR data are needed to spatially resolve these YSOs and higher spectral resolution near-IR spectra may be needed to more accurately determine the photospheric spectral types.

6.4. FU Orionis-like Stars and Excess CO Absorption

Several targets have spectra that cannot be well modeled by adding extinction and veiling to a stellar photosphere. The most common of these are targets with FU Orionis-like spectra, characterized by having a near-IR spectrum dominated by water vapor absorption, without clearly defined narrow photospheric absorption lines, few if any emission lines, and deep CO absorption in excess of what is observed in the spectra of late type dwarf photospheres. Flux from these objects is dominated by emission from the disk (presumably due to accretion luminosity) with negligible flux from the stellar photosphere (Hartmann & Kenyon 1996). Since the heating of the disk is dominated by viscous dissipation versus stellar irradiation, the disk interior is hotter than the surface. Cooler material above the disk photosphere imprints the observed water and CO absorption bands on the spectrum. One object (04073+3800) has a highly veiled spectrum without excess water absorption and has been identified as a FU Orionis-like star (Sandell & Aspin 1998). FU Orionis-like objects are found in region E of Figures 4 and 5. As a group, these targets are much more luminous than the rest of the observed sample. The median bolometric luminosity for targets with FU Orionis-like spectra is $28 L_{\odot}$ whereas the median bolometric luminosity for targets in region D (with dwarf like spectra and gravities) of Figures 4 and 5 is $4.0 L_{\odot}$. The two-sample Kolmogorov-Smirnov test shows that those targets with FU Orionis-like spectra have a higher bolometric luminosity than those targets with dwarf like spectra with 99.5% confidence. Although the bolometric luminosities are higher, the spectral index distributions (both of which are measured using IRAS fluxes from $12 \mu\text{m}$ to $100 \mu\text{m}$) for region D and E

are statistically indistinguishable. Since these targets have deep CO absorption and tend to be excessively luminous, these are likely to be examples of FU Orionis-like objects. Indeed, two targets in our sample with this kind of spectrum, IRAS 04287+1801 (L1551 IRS5) and IRAS 21454+4718 (V1735 Cygni) are well known FU Orionis-like objects.

Of the ten FU Ori and FU Ori-like stars in our sample, two (and possibly a third) are newly identified FU Ori-like candidates and these are the first near-IR spectra of them. FU Orionis-like objects are relatively rare. Previously, ~ 21 have been identified (Reipurth & Aspin 2010) and only $9.1\% \pm 2.9\%$ (10/110) of the sample targets have this type of spectrum. Thus, the fraction of Class I YSOs that pass through a FU Orionis phase times the average duty cycle of the FU Orionis phase is roughly 9%. It is significant to find such a large fraction of FU Orionis-like stars among a sample of Class I YSO. Identifying two new embedded FU Orionis-like stars is particularly important since these observations have significantly increased the number of known *embedded* FU Orionis-like objects. Previously, only ~ 8 have been identified. Table 6 lists the FU Ori and FU Ori-like stars in our sample, as well as other stars that show excess CO absorption.

In addition to FU Orionis-like stars, seven other stars show CO absorption greater than what would be expected from the star’s spectral type. All of these show photospheric absorption lines, and in four cases the CO EW is only marginally greater than the M4 value and we do not consider these four to be candidate FU Orionis-like objects. IRAS 06393+0913 has strong CO absorption but lacks the high veiling and deep water absorption bands that are commonly observed in the spectra of FU Orionis-like objects, and thus we do not classify it as an FU Orionis-like object. Three targets (IRAS 05327–0457W, 05404–0948, and 16235–2416) have an A or F-type photosphere with weak CO band-head absorption. IRAS 05404–0948 also appears to have weak water absorption bands. In these cases, the CO band-head and water absorption may be caused by circumstellar material or an unresolved late type companion. The absolute K-band magnitudes (simply the observed K-band magnitude of these objects corrected for distance, and not corrected for accretion or extinction) of the K and M-type stars in this sample are on average 2.5 magnitudes fainter than the absolute K-band magnitudes of the A and F-type stars (in comparison, the bolometric luminosities of main-sequence A0 and M0 stars are different by ~ 8 magnitudes). However, the brightest K and M-type stars have the same absolute K-band magnitude as the faintest A and F-type stars, most likely due to a combination of accretion and extinction related effects. As such, for Class I YSOs it is reasonable to expect to see a contribution from a late type companion star in the spectrum of an early-type primary star. The other three stars (04292+2422W, 04591–0856, 18341–0113N) are best fit with G or K type spectra but have CO absorption in excess of the latest type star that is a good fit. Remarkably, these six objects also tend to not have emission lines. IRAS 04591–0856 has H₂ emission lines, which may be associated

with a wind (Beck et al. 2008), and 05327–0457W shows weak Br γ emission at the bottom of that deep absorption feature. Considering that these six objects share some properties in common with FU Ori-like stars (excess CO absorption, a dearth of emission features), these objects may be experiencing weak FU Orionis-like activity. Thus *the shape of the continuum and the depth of the CO band-heads in the spectrum of a Class I protostar may not always be representative of the true spectral type of the stellar photosphere.*

6.5. Herbig Ae/Be Stars

Herbig Ae/Be stars (Herbig 1960) were identified as stars with spectral type earlier than F0 with Balmer emission lines and associated with a dark cloud. Hillenbrand et al. (1992) showed that these are intermediate mass pre-main sequence stars with massive accretion disks. This spectroscopic survey of Class I YSOs found 3 targets with an A class best-fit spectral type (see Table 2), as determined by our spectral line matching routine. Since these objects satisfied our criteria to be Class I YSOs, and since the spectra of two of these stars show emission features, all three show veiling, we believe that these are embedded Herbig Ae stars. In this case, only $2.7\% \pm 1.6\%$ of the Class I YSOs are embedded Ae type stars.

6.6. Spectra of Binaries

Many T Tauri binary systems have been spectroscopically observed, and Table 1 in Monin et al. (2007) lists the number of T Tauri binary systems with classical T Tauri (possessing a disk and accreting matter) and weak line T Tauri (non-accreting) components. We used the number of T Tauri binaries in the center column of Table 1 in Monin et al. (2007) to exclude objects with very close companions, and excluded the three systems with a passive disk. Table 1 in Monin et al. (2007) includes 59 ($74.6\% \pm 9.7\%$) T Tauri binary systems where both components are classical T Tauri stars or both are weak line T Tauri stars, whereas 20 ($25.3\% \pm 5.7\%$) are mixed systems. Has this correlation been established by the Class I phase?

Over the course of this survey, we observed the spatially resolved spectra of both of the components of 9 previously identified multiple protostars included in Connelley et al. (2008a). This includes 1 triple system, for a total of 10 pairs. In order to be clearly resolved, these objects are well separated on the sky, with a median angular separation of $4''.5$. These objects have a median projected separation of 2700 AU, with a minimum separation of 400 AU and maximum separation of 4500 AU. Both components of each pair also had to

be brighter than $K=12$ to get a high S/N observation. The properties of these binaries are given in Table 7.

We noticed that the spectra of Class I binaries tend to have the same veiling, i.e. both components have high veiling or both have low veiling. Are the veiling of the binary components consistent with randomly pairing spectra from the whole sample? In the whole sample, 57.4% of targets have high veiling, whereas 42.6% have low veiling. Among the binary spectra, both components of 8/10 pairs ($80\% \pm 28\%$) either both have high veiling or both have low veiling. The probability that less than 3 out of 10 pairs would have different veilings, having been randomly selected from this atlas of protostellar spectra, is 4.6%. Thus, we can state at the $\sim 95\%$ confidence level that binary protostars are not randomly paired and that their spectra tend to have the same veiling. Excluding the FS Tau system, which includes a well known T Tauri star, both components of 8/9 pairs ($89\% \pm 31\%$) either both have high veiling or both have low veiling. Subjectively, the spectra of binary components often look remarkably similar. For example, the spectra of the components of IRAS 18383+0059 and the components of IRAS 05375–0040 are quite difficult to tell apart. We have shown that the trend of T Tauri binary components to both be accreting (or not) extends to the Class I phase at much higher accretion rates, for targets selected across the sky. We note that 8/11 of the components with low veiling show Br γ emission, and thus are accreting.

Interactions between the circumstellar disks could explain the dearth of mixed Class I binary systems. For example, a close passage between two stars could trigger higher accretion and/or higher veiling in both systems. The projected separations between the stars of these binaries is within an order of magnitude of the expected size of a circumstellar disk, so interactions between the disks are plausible. If this scenario is true, then we would expect that closer binaries would tend to have higher veiling. Based on the values in Table 7, there is no trend of increasing veiling with decreasing projected separation.

If interactions between the disks are not responsible for these stars having the same veiling, and if we assume that these protostellar binaries are coeval, then another explanation is that the veiling systematically changes with time within the Class I phase. Presumably, younger objects have higher veiling and more evolved objects have lower veiling. If the veiling of a given protostar were not to systematically change with time, but rather changed randomly on a timescale much less than the Class I life time, then the number of binary pairs with the same (or different) veilings would be indistinguishable from a random selection from the whole sample.

H_2 emission is seen from 42.7% of the targets in the whole sample. Similarly, Doppmann et al. (2005) found that 44% of Class I and flat spectrum YSOs have H_2 emission in their smaller sample. Among the binary spectra, both components of 9/10 pairs ($90\% \pm 30\%$) either have

H₂ emission or both do not have H₂ emission. The probability that only 1 out of 10 pairs would have different H₂ emission, having been randomly selected from this atlas of protostellar spectra, is 2.8%. The presence of H₂ emission in both components of protostellar binaries is correlated with $\sim 97\%$ confidence. We also note that only 5 of 19 binary components (26.3%) have H₂ emission, less than the 42.7% for the whole sample.

6.7. Gravity and Late Type Continuum Profiles

Lucas et al. (2001) found that a number of young (~ 1 Myr) low mass ($< 0.1 M_{\odot}$) sources in the Trapezium cluster have an H-band continuum spectrum that is characterized by a triangular profile with a peak near $1.68 \mu\text{m}$. They attribute this to the expected lower gravity of younger sources, and that this is an independent way to verify that these are substellar sources. A field dwarf observed by Kirkpatrick et al. (2006) also has a triangular shaped H-band continuum spectrum which they interpret as a sign of low gravity and thus youth since regular field dwarfs (Cushing et al. 2005) do not exhibit this feature. Several other young brown dwarfs have been identified (e.g. Gizis et al. 2002, Looper et al. 2007) with this feature. The surface gravities of protostars and young brown dwarfs are very similar. The average $\log(g)$ for protostars from Table 3 of Doppmann et al. (2005) is 3.98, whereas average $\log(g)$ for 5 Myr brown dwarfs from Table 4 of Rice et al. (2010) is 3.87. The triangular shape of the H-band continuum spectrum is caused by the reduction of the pressure induced opacity in H₂ in the atmosphere of the star (Marley et al. 2010). The spectrum of pressure induced opacity in H₂ is very broad, which has the effect of smoothing the opacity spectrum of the stellar atmosphere as a whole. Without this opacity source, the shape of the continuum near H-band is dominated by the opacity spectrum of water.

We used our continuum fitting routine described above to determine which objects in our sample with a late type continuum (excluding FU Orionis-like objects) that also have a triangular H-band continuum. These objects are flagged in Table 1. As an input to this routine, we used the best-fit spectral type as well as the latest spectral type within the uncertainties. Of the 27 objects in our sample with a well matched late spectral type, 15 ($55.5\% \pm 14.3\%$) have a triangular H-band continuum. Of the 21 objects in our sample of the M class spectral type, 10 ($47.6\% \pm 15.1\%$) have a triangular H-band continuum. These results show that the triangular H-band is common among Class I YSOs with late type spectra, yet only about half of them show this feature. Among all Class I YSOs, only about 14% of them have a triangular H-band. Although our sample of objects are certainly all very young (indeed much younger than the brown dwarfs discussed above), they are likely to be much more massive than brown dwarfs. The objects in our sample may have evolved

enough (towards higher gravities) so that only about half of the late type spectra in the sample show this triangular H-band structure. Also, high extinction and high veiling make it more difficult to identify which targets have a triangular shaped H-band continuum, so this result should be interpreted as a lower limit.

Greene & Lada (1996) used the EW of Na I (2.206 μm and 2.208 μm) plus Ca I (2.263 μm and 2.266 μm) versus the EW of CO as a gravity sensitive indicator. On this plot, most YSOs fall closer to the line formed by luminosity class V than luminosity class III stars, with FU Orionis-like stars below the line made by luminosity class III stars. Figures 4 and 5 show the locations of our Class I protostars on this plot. The EWs for the luminosity class III (dwarf) and V (giant) stars were measured from stars in the SpeX spectral library in the same way as our YSOs. Similar to the result in Greene & Lada (1996), most of our Class I YSOs also lie closer to the line formed by luminosity class V than luminosity class III stars (region D), with increasing veiling pushing the location of stars on this plot towards (0,0). Class I YSOs tend to have slightly lower gravity than dwarf stars, but not as low as giants. YSOs with triangular H-band continua are shown in red in Figures 4 and 5, and tend to be found to the upper right of the remaining YSOs.

7. Conclusions

We have presented the results of a spectroscopic survey of 110 Class I young stellar objects covering $\lambda = 0.80 \mu\text{m}$ to $2.43 \mu\text{m}$ selected from the Connelley et al. (2008a) imaging survey. This atlas demonstrates the great diversity of spectroscopic properties among embedded protostars. We estimated the spectral types, extinction, veiling, and veiling temperatures of these protostars as the data allowed. Extinction was estimated using broadband colors from 2MASS, emission line ratios, and modeling of the spectrum. The median estimated extinction is $A_v = 14.7$ with a median uncertainty of 3.7 magnitudes based on continuum fitting, with the estimated extinctions ranging from $A_v = 0.0$ to $A_v = 57.8$. Scattered light can lead to the extinction values being underestimated. Veiling ranges from being negligible to completely veiling the photospheric emission. When we were able to constrain the veiling, the median veiling was $r_k = 0.48$ with a median uncertainties of +1.32 and -0.24 . Spectral types were estimated by matching photospheric line equivalent widths with values measured from library spectra of dwarf stars, and we present the distribution of derived spectral types. The median best-fit spectral type is K5 with a median uncertainty of 4 sub-classes. The best fit spectral types in this sample range A0 to M4. Our main conclusions are:

1) $\sim 92\%$ of embedded protostars show some sign of active accretion: Br γ emission and/or high veiling.

2) Having divided our sample between targets with low veiling and high veiling, we found that targets with high veiling are over represented among targets with strong reflection nebosity whereas targets with low veiling are over represented among targets with a weak reflection nebula or no reflection nebula.

3) There are no embedded early type stars in the Taurus-Auriga and Perseus star forming regions and a relative excess of embedded early type stars in the Orion and Ophiuchus regions. This is consistent with what has been previously found among T Tauri stars.

4) Observations showed that this sample includes ten FU Orionis-like objects, including two new embedded objects with FU Orionis-like near-IR spectra. All three FU Orionis-like stars with data near $1\ \mu\text{m}$ show deep He I absorption. Although FU Orionis-like stars have high accretion luminosities, they are never observed to clearly show Br γ emission. We speculate that the relationship between Br γ line flux and mass accretion collapses at very high mass accretion rates.

5) The presence of the [Fe II] and H_2 emission lines are highly correlated, suggesting that H_2 is also shock excited.

6) CO was observed in emission in 27 sources. CO emission was usually only seen when the veiling was high, and such targets *always* show Br γ emission as well. Although all FU Orionis-like stars showed strong CO absorption, several other stars showed CO absorption in excess of what is expected based on the photospheric spectral type of the star.

7) Both components of 10 binaries were observed, with a median projected separations ranging from 45 AU to 4500 AU. The veiling of the components of binaries are correlated, with both components tending to have either low or high veiling. This is also consistent with what has been identified previously among T Tauri stars, but this is now observed at higher accretion rates and younger ages. Also, in several cases the spectra of the components of a binary are so similar as to be difficult to visually tell apart.

8) Roughly half of the M-type stars in this sample have a H-band continuum with a triangular profile, a signature of low gravity.

We acknowledge support from NASAs Origins of Solar Systems program via WBS 811073.02.07.01.89. We are grateful for the professional assistance from Bill Golish, Dave Griep, Paul Sears, and Eric Volquardsen. We thank the referee and Bo Reipurth for their helpful and constructive comments. This research has made use of the SIMBAD database, operated at CDS, Strasbourg, France, and NASA’s Astrophysics Data System. This publication makes use of data products from the Two Micron All Sky Survey, which is a joint project of the University of Massachusetts and the Infrared Processing and Analysis Cen-

ter/California Institute of Technology, funded by the National Aeronautics and Space Administration and the National Science Foundation. This research has made use of NASA’s Astrophysics Data System. This research was supported by an appointment to the NASA Postdoctoral Program at the Ames Research Center, administered by the Oak Ridge Associated Universities through a contract with NASA.

A. Class I YSO Spectral Atlas

Figure 13 presents the spectrum of each of the targets that we observed from $0.8\ \mu\text{m}$ to $2.45\ \mu\text{m}$, although many objects are too faint and/or red to have any detectable flux shortward of H-band. The locations of significant absorption and emission features are shown across the top of each page. The vertical axis is normalized by the maximum flux value in the spectrum of each target. Of the 110 targets that we observed, we detected the spectrum of all of them at K-band. We were able to detect the continuum in H-band for 107 (97%) targets and in J-band for 67 (61%) targets.

B. Comments on Individual Objects

IRAS 03220+3035 (N) L1448 IRS 1, RNO 13. This is a close ($1''.37$) binary with IRAS 03220+3035 (S) (Connelley et al. 2008a). This component shows strong [Fe II] ($1.644\ \mu\text{m}$) emission which the spectral image shows to be spatially extended. Among other species, we observed emission from He I ($1.083\ \mu\text{m}$, $2.058\ \mu\text{m}$), O I ($1.129\ \mu\text{m}$), [Fe II] ($1.257\ \mu\text{m}$), Fe II ($1.688\ \mu\text{m}$, $1.742\ \mu\text{m}$), and Na I ($2.206\ \mu\text{m}$, $2.209\ \mu\text{m}$)

IRAS 03220+3035 (S) The binary companion to IRAS 03220+3035 (N), separated by $1''.37$ (Connelley et al. 2007). Although this object is likely as young as any other Class I YSO (being the companion of a Class I YSO and also having low gravity), the spectrum otherwise remarkably shows few signs of youth. The spectrum is consistent with there being no veiling and the only emission line (Br γ) is very weak. Were this object not embedded and the companion of a mass accreting protostar, its spectrum could have lead to this object being classified as a T Tauri star.

IRAS 03260+3111 (E) SVS 3. This is a close ($0''.55$) binary (Connelley et al. 2008a). Light from both stars contributed to this spectrum. We estimate a spectral type of F4-G0, Doppmann et al. (2005) estimate a $T_{eff}=5600\ \text{K}$, approximately G4.

IRAS 03260+3111 (W) This is source 205 Per in Evans et al. (2009) and Per-emb50 in Enoch et al. (2009), which they classify as a Class I YSO.

IRAS 03301+3111 The best-fit spectral type is M2, but the spectrum has a stronger break at $1.32\ \mu\text{m}$ than a K7 star, suggesting low gravity. This is source 289 Per in Evans et al. (2009) and Per-emb64 in Enoch et al. (2009), which they classify as a Class I YSO.

IRAS 03445+3242 HH 366 VLA 1 and Barnard 5 IRS. This is source 505 Per in Evans et al. (2009) and Per-emb53 in Enoch et al. (2009), which they classify as a Class I YSO.

IRAS 03507+3801 Source of HH 462. The CO band heads run together, and are not distinctly separate band heads, similar to IRAS 04073+3800. This object shows He I in absorption. Pa β is strongly seen in absorption, but Br γ is not.

IRAS 04016+2610 L1489 IRS and the source of HH 360, and a well known bipolar reflection nebula (Padgett et al. 1999). The H₂ emission is spatially extended and has been mapped with H₂ imaging (Lucas et al. 2000).

IRAS 04073+3800 PP 13S, source of HH 463. This object has an unusual reflection nebula with a ring-like morphology (Connelley et al. 2007). Sandell & Aspin (1998) identify this as an FU Orionis-like star. The near-IR spectrum is dominated by a featureless continuum and deep CO absorption. However, the CO band heads for this target are unusual in that they do not show the usual saw-tooth pattern, but rather appear blended together and the band heads are not distinct.

IRAS 04108+2803 (W) The spectrum has a stronger break at $1.32\ \mu\text{m}$ than an M2 star and a triangular H-band, suggesting low gravity.

IRAS 04113+2758 (S) This YSO’s spectrum shows a stronger break at $1.32\ \mu\text{m}$ than a M2 star as well as a triangular H-band, suggesting low gravity. White & Hillenbrand (2004) estimate a spectral type of $M3.5\pm1$ for this object.

IRAS 04181+2655 Designated as IRAS 04181+2655 B in Beck (2007), who estimated the spectral type to be $K7\pm1$, $r_k=0.0$, and $A_v=40$. Our results for the spectral type of $M1_{M1}^{K5}$, $r_k = 0.24_{0.24}^{0.00}$, and $A_v = 51.4_{7.5}^{2.0}$ are consistent.

IRAS 04181+2655 (S) Designated as IRAS 04181+2655 A in Beck (2007), who estimated the spectral type to be M3, $r_k=1.3$, and $A_v=17.8$. We derived a higher A_v , a lower r_k , and estimate that the spectral type can be from G0 to M3.

IRAS 04189+2650 (E) FS Tau A. This is a very close binary star (Chen et al. 1990). The H₂ emission is also found to be spatially extended.

IRAS 04239+2436 HH 300 VLA 1. The spectrum shows high veiling, with a wide variety of species in emission (e.g. H, H₂, [Fe II], Na, Mg, CO)

IRAS 04240+2559 DG Tau. Strong atomic H and Ca II emission lines. The best fit spectral type from photospheric lines is G3, but we also observed water absorption and weak CO absorption. An M2 spectrum provides a better continuum fit in the H-band region. We estimate a spectral type of G1-K2, whereas White & Hillenbrand (2004) estimate K1-K5 and Doppmann et al. (2005) estimate a $T_{eff}=4000$ K, approximately K7.

IRAS 04248+2612 HH 31 IRS 2. The spectrum has stronger break at $1.32 \mu\text{m}$ than an M3 star and also has a triangular H-band, suggesting low gravity. We estimate a spectral type of M0-M4, whereas White & Hillenbrand (2004) estimate $M5.5 \pm 1$.

IRAS 04292+2422 (E) V806 Tau, Haro 6-13. We estimate a spectral type of G7 (with acceptable fits from G0 to M3), whereas White & Hillenbrand (2004) estimate $M0 \pm 0.5$.

IRAS 04292+2422 (W) V806 Tau, Haro 6-13. Spectral type fitting finds a best match of G7 (from G0 to M3), however the CO absorption is in excess of what is expected from a K5 dwarf star.

IRAS 04295+2251 L1536 IRS. Has a double peaked spectral type goodness-of-fit curve: either K0-K7 or M1-M4, both need some veiling. Doppmann et al. (2005) estimate a $T_{eff}=3400$ K, approximately M3. Values in Table 2 are based on fits to an M2 star, which had the best RMS continuum fit to the data. Beck (2007) estimated the spectral type to be K7, $r_k=0.9$, and $A_v=28$. We derived similar values for r_k and A_v .

IRAS 04315+3617 This spectrum shows strong He I absorption. The calcium triplet near $0.85 \mu\text{m}$ is also strongly seen.

IRAS 04530+5126 V347 Aur, RNO 33. The spectrum has a stronger break at $1.32 \mu\text{m}$ than an M2 star and it also has a triangular H-band, suggesting low gravity. We also observed very strong blue shifted He I absorption as well as emission near rest velocity.

IRAS 04591–0856 Gy 2-13 1. Spectral type fitting finds a best match of K7 (from K4 to M3), however the CO absorption is in excess of what is expected from an M3 dwarf star. The H-band continuum is better fit with an M2 spectrum than a K7 spectrum. The spectrum of this object has prominent H_2 emission lines, as well as broad ($\text{FWHM}=640 \text{ km s}^{-1}$) and red-shifted (315 km s^{-1}) Br γ emission.

IRAS 05327–0457 (W) The best-fit spectral class is A5, and the spectral classes of acceptable fits range from A0-F7. Despite this, CO bands are weakly seen in absorption. Adaptive optics observations (Connelley et al. 2008a) have shown that this is a close ($0''.14$) binary star, raising the possibility that the water and CO absorption features could be from the companion having a late-type spectrum.

IRAS 05404–0948 The best-fit spectral class is F0, and the spectral classes of acceptable fits range from A5-F3. Despite this, water and CO bands are weakly seen in absorption. Adaptive optics observations (Connelley et al. 2008a) have shown that this is a close ($0''.16$) binary star, raising the possibility that the water and CO absorption features could be from the companion having a late-type spectrum.

IRAS 05450+0019 A new FU Orionis-like star, and the illuminating source of a large bipolar reflection nebula (Connelley et al. 2007).

IRAS 05513–1024 V1818 Ori. This object has an early type stellar spectrum where veiling dominates the spectrum at H and K-band, with CO in emission. This object also has strong He I absorption near rest velocity. Best fit veiling from photospheric line matching is $r_k = 8.8$.

IRAS 06297+1021 (W) This object has a spectrum that is unique in this sample. The spectrum of this object has several features in common with spectra from other FU Ori and FU Ori-like objects in this sample (e.g. high veiling, strong water absorption bands, strong blue shifted He I absorption). However, the spectrum also shows several strong emission lines, including CO and many metals (e.g. Mg & Na) that is uncharacteristic of other FU Ori and FU Ori-like objects in this sample. Due to these anomalies, we do not consider this to be a candidate FU Ori-like object.

IRAS 06393+0913 Our photospheric line matching code found a best-fit spectral type of G7, with acceptable fits from G0 to M0. As with other FU Orionis-like stars, the spectrum shows no emission lines and deep CO absorption. However, the spectrum lacks the deep water vapor absorption bands commonly seen in the spectra of FU Ori-like stars, and thus we do not classify it as such.

IRAS 16235–2416 ρ Oph S1, Elias 2-25. Spectral type fitting finds a best match of F0 (from A3 to F4), however the CO absorption is in excess of what is expected from an F4 dwarf star.

IRAS 16240–2430 (E) This is also known as EL29, GY214, 871 Oph in Evans et al. (2009) and Oph-emb16 in Enoch et al. (2009), which they classify as a Class I YSO.

IRAS 16240–2430 (W) This is also known as WL16, GY182, 857 Oph in Evans et al. (2009) and Oph-emb21 in Enoch et al. (2009), which they classify as a Class I YSO. This object is an early type star and shows very strong CO emission.

IRAS 16288–2450 (E) This is also known as L1689 IRS 5, IRS67, 1003 Oph in Evans et al. (2009) and Oph-emb10 in Enoch et al. (2009), which they classify as a Class I YSO.

IRAS 16288–2450W ρ Oph S, near the position of the source Oph-emb7 in Enoch et al. (2009). Their position is at the same RA, but is $1'$ to the south.

IRAS 16289–4449 HH 57 IRS and V346 Normae. This object is considered to be an FU Orionis type object since it was observed to erupt. In common with other FU Ori and FU Ori-like objects, its spectrum has strong blue shifted He I absorption with no other component to the line. Unlike several other FU Ori and FU Ori-like objects, the spectrum of this object shows strong CO emission. The Paschen β line has a P Cygni profile with weak blue shifted absorption.

IRAS 18250–0351 NZ Serpensis. This star shows very strong atomic hydrogen emission, including emission from the H I Pfund series.

IRAS 18270–0153 (6) A new FU Orionis-like star, and a member of a close binary in a small group of young stars (Connelley et al. 2008a).

IRAS 18341–0113 (N) Spectral type fitting finds a best match of M2 (with acceptable fits from K0 to M4), however the CO absorption is in excess of what is expected from an M4 dwarf star. The water vapor absorption bands are much stronger than expected for a K5 star (the best-fit type), suggesting that the true spectral type may be later. Indeed, the narrow photospheric lines of a M3 type spectrum was nearly as good of a fit as the lines from a K5 spectrum. The H-band continuum is strongly peaked, suggesting low gravity. This is one of the few objects where the photospheric lines from luminosity class III stars (giants) are a better match to the YSO's photospheric lines than photospheric lines from luminosity class V stars (dwarfs).

IRAS 18341–0113 (S) The spectrum of this source has deep water vapor absorption bands and lacks narrow photospheric features, in common with other FU Ori and FU Ori-like stars. However, the characteristically strong CO band head absorption of FU Ori objects is observed to be quite weak.

IRAS 19266+0932 Parsamian 21 and source of HH 221. Our spectral type matching code finds a best-fit G3 spectral class, with a range of uncertainty from F5 to K2. However, this source also shows water and excess CO absorption. Continuum fit results in Table 2 are based on an M4 input spectrum, which was the best continuum fit. Staude et al. (1992) identified this object as an FU Orionis-like source.

IRAS 20568+5217 HH 381 IRS, a known FU Orionis-like object (Reipurth & Aspin 1997). Continuum fit results in Table 2 are based on an M8 input spectrum, which was the best continuum fit.

IRAS 21352+4307 In Barnard 158. The spectral image shows that the H_2 emission

is spatially extended to the north by $\sim 1''.2$.

IRAS 21454+4718 V1735 Cyg. This one of the few targets with an FU Orionis-like spectrum, and only one of three where we observed strong He I absorption. Skinner et al. (2009) found that this FU Orionis type star is the source of hard X-rays from very hot plasma, uncharacteristic of accretion shocks. They note that cooler plasma from accretion shocks could be present and heavily obscured. An embedded Spitzer source $24''$ to the WNW, detected as an $L'=10.7$ source in images taken by Connelley et al. (2008a), was also detected in X-rays. Continuum fit results in Table 2 are based on an M8 input spectrum.

IRAS 22051+5848 HH 354 IRS, a known FU Orionis-like object (Reipurth & Aspin 1997).

IRAS 22324+4024 LkH α 233. F3 is the best-fit spectral type based on matching the photospheric absorption lines. Veiling based on continuum fitting is $r_k = 8.4^{+2.2}_{-1.3}$, whereas $r_k = 6.2^{+0.0}_{-3.2}$ is the best result from photospheric line fitting. However, the H and K band regions of the spectrum are best-fit by a warm (920^{+100}_{-100} K) veiling emission. The early photospheric spectral type combined with the relatively cool dust suggests that there is a significant gap between the star and the inner edge of the dust disk. However, the presence of Ca II, Pa β and Br γ emission shows that gas is being accreted onto the star. A solution to this problem is to propose that this is a close binary system with an early type primary star and a lower mass Class I YSO or T Tauri star with a strong IR excess as a companion. Early type stars are commonly in such binary systems (e.g. Baines et al. 2006, Corporon & Lagrange 1999). Although stars with high veiling tend to have fainter absolute K-band magnitudes than A or F type stars, the brighter high veiling stars have similar absolute K-band magnitudes as the fainter A or F-type stars. As such, it is possible for the K-band flux of a companion with high veiling to rival the flux from the early-type primary star.

REFERENCES

- Ábrahám, P., Kóspál, Á., Csizmadia, Sz., Kun, M., Moór, A., & Prusti, T., 2002, *A&A*, 428, 89
- Adams, F., Lada, C., & Shu, F., 1987, *ApJ*, 312, 788
- Alexander, C., Boss, A., Keller, L., Nuth, J., & Weinberger, A., in *Protostars and Planets V*, eds. B. Reipurth, D. Jewitt, & K. Keil, University of Arizona Press, 2007, p.801
- Azevedo, R., Calvet, N., Hartmann, L., Folha, D., Gameiro, F., & Muzerolle, J., 2006, *A&A*, 456, 225
- Baines et al., 2006, *MNRAS*, 367, 737
- Bally, J., Reipurth, B., & Davis, C., in *Protostars and Planets V*, eds. B. Reipurth, D. Jewitt, & K. Keil, University of Arizona Press, 2007, p.215
- Baraffe, I., Chabrier, G., Allard, F., & Hauschildt, P., 1998, *A&A*, 337, 403
- Baraffe, I., Chabrier, G., Allard, F., & Hauschildt, P., 2002, *A&A*, 382, 563
- Bautista, M., & Pradham, A., 1998, *ApJ*, 650
- Beck, T. 2007, *AJ*, 133, 1673
- Beck, T., McGregor, P., Takami, M., & Pyo, T.S., 2008, *ApJ*, 676, 472
- Boss, A., & Grahm, J., 1993, *LPI*, 24, 153
- Brandeker, A., Jayawardhana, R., Khavari, P., Haisch, K., & Mardones, D., 2006, *ApJ*, 652, 1572
- Briceño, C., Luhman, K., Hartmann, L., Kirkpatrick, J., 2002, *ApJ*, 580, 317
- Calvet, N., Patino, A., Magris, G., & D’Alessio, P., 1991, *ApJ*, 380, 617
- Chen, W., Simon, M., Longmore, A., Howell, R., & Benson, J., 1990, *ApJ*, 357, 224
- Connelley, M., Reipurth, B., & Tokunaga, A., 2007, *AJ*, 133, 1528
- Connelley, M., Reipurth, B., & Tokunaga, A., 2008a, *AJ*, 135, 2496
- Connelley, M., Reipurth, B., & Tokunaga, A., 2008b, *AJ*, 135, 2526

- Connelley, M., Reipurth, B., & Tokunaga, A., 2009, *AJ*, 138, 1193
- Corporon & Lagrange, 1999, *A&AS*, 136, 429
- Cushing, M., Vacca, W., & Rayner, J., 2004, *PASP*, 116, 362
- Cushing, M., Rayner, J., & Vacca, W., 2005, *ApJ*, 623, 1115
- Doppmann, G., Greene, T., Covey, K., & Lada, C., 2005, *AJ*, 130, 1145
- Dupree, A., Sasselov, D., & Lester, J., 1992, *ApJ*, 387, L85
- Edwards, S., Fischer, W., Kwan, J., Hillenbrand, L., & Dupree, A., 2003, *ApJ*, 599, L41
- Edwards, S., Fischer, W., Hillenbrand, L., & Kwan, J., 2006, *ApJ*, 646, 319
- Enoch, M., Evans, N., Sargent, A., & Glenn, J., 2009, *ApJ*, 692, 973
- Eriksen, K., Arnett, D., McCarthy, D., & Young, P., 2009, *ApJ*, 697, 29
- Evans, N., et al. 2009, *ApJS*, 181, 321
- Gamiero, J., Folha, D., & Petrov, P., 2006, *A&A*, 445, 323
- Gizis, J., 2002, *ApJ*, 575, 484
- Glassgold, A., Najita, J., & Igea, J., 2004, *ApJ*, 615, 972
- Greene, T., Aspin, C., & Reipurth, B., 2008, *AJ*, 135, 1421
- Greene, T., & Lada, C., 1996, *AJ*, 112, 2184
- Haisch, K., Lada, E., & Lada, C., 2001, *ApJ*, 553, L153
- Haisch, K., Lada, E., & Lada, C., 2001, *AJ*, 121, 2065
- Hamann, F., & Persson, S., 1990, *ASPC*, 9, 304
- Hartmann, L., *Accretion Processes in Star Formation*, Cambridge, UK, Cambridge University Press, 2000
- Hartmann, L., & Kenyon, S., 1985, *ApJ*, 299, 462
- Hartmann, L., & Kenyon, S., 1996, *ARA&A*, 34, 207
- Herbig, G., 1960, *ApJS*, 4, 337

- Herbig, G., 1962, in "Advances in Astronomy and Astrophysics", ed. Zdeněk Kopal, Academic Press, New York, p.47
- Hernández, J., Hartmann, L., Calvet, N., Jeffries, R., Gutermuth, R., Muzerolle, J., & Stauffer, J., 2008, *ApJ*, 686, 1195
- Hillenbrand, L., 1997, *AJ*, 113, 1733
- Hillenbrand, L., Strom, S., Vrba, F., & Keene, J., 1992, *ApJ*, 397, 613
- Kenyon, S., & Hartmann, L., 1995, *ApJS*, 101, 117
- Kirkpatrick, J., Barman, T., Burgasser, A., McGovern, M., McLean, I., Tinney, C., & Lowrance, P., 2006, *ApJ*, 639, 1120
- Lada, C., 1990, in "The Physics of Star Formation and Early Stellar Evolution", eds. Lada, C., & Kylafis, N., Kluwer Academic Publishers, p. 343
- Looper, D., Burgasser, A., Kirkpatrick, J., & Swift, B., 2007, *ApJ*, 669, L97
- Lucas, P., Blundell, K., & Roche, P., 2000, *MNRAS*, 318, 526
- Lucas, P., Roche, P., , Allard, F., & Hauschildt, P., 2001, *MNRAS*, 326, 695
- Luhman, K., Allen, P., Espinallat, C., Hartmann, L., & Calvet, N., *ApJS*, 186, 111
- Luhman, K., Stauffer, J., Muench, A., Rieke, G., Lada, E., Bouvier, J., & Lada, C., 2003, *ApJ*, 593, 1093
- Luhman, K., Whitney, B., Meade, M., Babler, B., Indebetouw, R., Bracker, S., & Churchwell, E., 2006, *ApJ*, 647, 1180
- Marley, M., Saumon, D., Lodders, K., & Cruz, K., 2010 in prep
- Martin, S., 1997, *ApJ*, 478, L33
- Meyer, M., Calvet, N., Hillenbrand, L. 1997, *AJ*, 114, 288
- Monin, J., Clarke, C., Prato, L., & McCabe, C., in *Protostars and Planets V*, eds. B. Reipurth, D. Jewitt, & K. Keil, University of Arizona Press, 2007, p.395
- Muzerolle, J., Hartmann, L., & Calvet, N., 1998, *AJ*, 116, 2965
- Najita, J., Carr, J., Glassgold, A., Shu, F., & Tokunaga, A., 1996, *ApJ*, 4652, 919

- Nishiyama, S., Tamura, M., Hatano, H., Kato, D., Tanabe, T. Sugitani, K., Nagata, T., 2009, *ApJ*, 696, 1407
- Nussbaumer, H., & Storey, P., 1988, *A&A*, 193, 327
- Padgett, D., Brandner, W., Stapelfeldt, K., Strom, S., Terebey, S., & Koerner, D., 1999, *AJ*, 117, 1490
- Rayner, J., Toomey, D., Onaka, P., Denault, A., Stahlberger, W., Vacca, W., Cushing, M., & Wang, S., 2003, *PASP*, 15, 362
- Rayner, J., Cushing, M., & Vacca, W. 2009, *ApJS*, 185, 289
- Rice, E., Barman, T., McLean, I., Prato, L., & Davy Kirkpatrick, J., 2010, *ApJS*, 186, 63
- Reipurth, B., & Aspin, B., 1997, *AJ*, 114, 6
- Reipurth, B., & Aspin, B., in *Evolution of Cosmic Objects through their Physical Activity*, eds. H. Harutyunyan, A. Mickaelian, & Y. Terzian, Gitutyun Publishing House, Yerevan, Armenia, 2010
- Reipurth, B., Aspin, C., Beck, T., Brogan, C., Connelley, M., & Herbig, G., 2007, *AJ*, 133, 1000
- Reipurth, B., Yu, K., Heathcote, S., Bally, J., & Rodríguez, L., 2000, *AJ*, 120, 1449
- Robitaille, T., Whitney, B., Indebetouw, R., Wood, K., & Denzmore, P., 2006, *ApJS*, 169, 328
- Román-Zúñiga, C., Lada, C., Muench, A. & Alves, J., 2007, *ApJ*, 664, 357
- Rydgren, A., & Vrba, F., 1981, *AJ*, 86, 1069
- Sandell, G., & Aspin, C., 1998, *A&A*, 333, 1016
- Skinner, S., Sokal, K., Gudel, M., & Briggs, K., 2009, *ApJ*, in press
- Smith, N., & Hartigan, P., 2006, *ApJ*, 638, 1045
- Storchi-Bergmann, T., McGregor, P., Riffel, R., Simões Lópes, R., Beck, T., & Dopita, M., 2009, *MNRAS*, 394, 1148
- Storey, P., & Hummer, D., 1995, *MNRAS*, 272, 41
- Staude, H., & Neckel, T., 1992, *ApJ*, 400, 556

- Takami, M., Chrysostomou, A., Bailey, J., Gledhill, T., Tamura, M., & Terada, H., 2002, ApJ, 568, L53
- van Kempen, T., van Dishoeck, E., Salter, D., Hogerheijde, M., Jørgensen, J., & Boogert, C., 2009, A&A, 498, 167
- Walker, M., 1956, ApJS, 2, 365
- White, R., & Hillenbrand, L., 2004, ApJ, 616, 998
- Whitney, B., Wood, K., Bjorkman, J., & Cohen, M., 2003, ApJ, 598, 1079

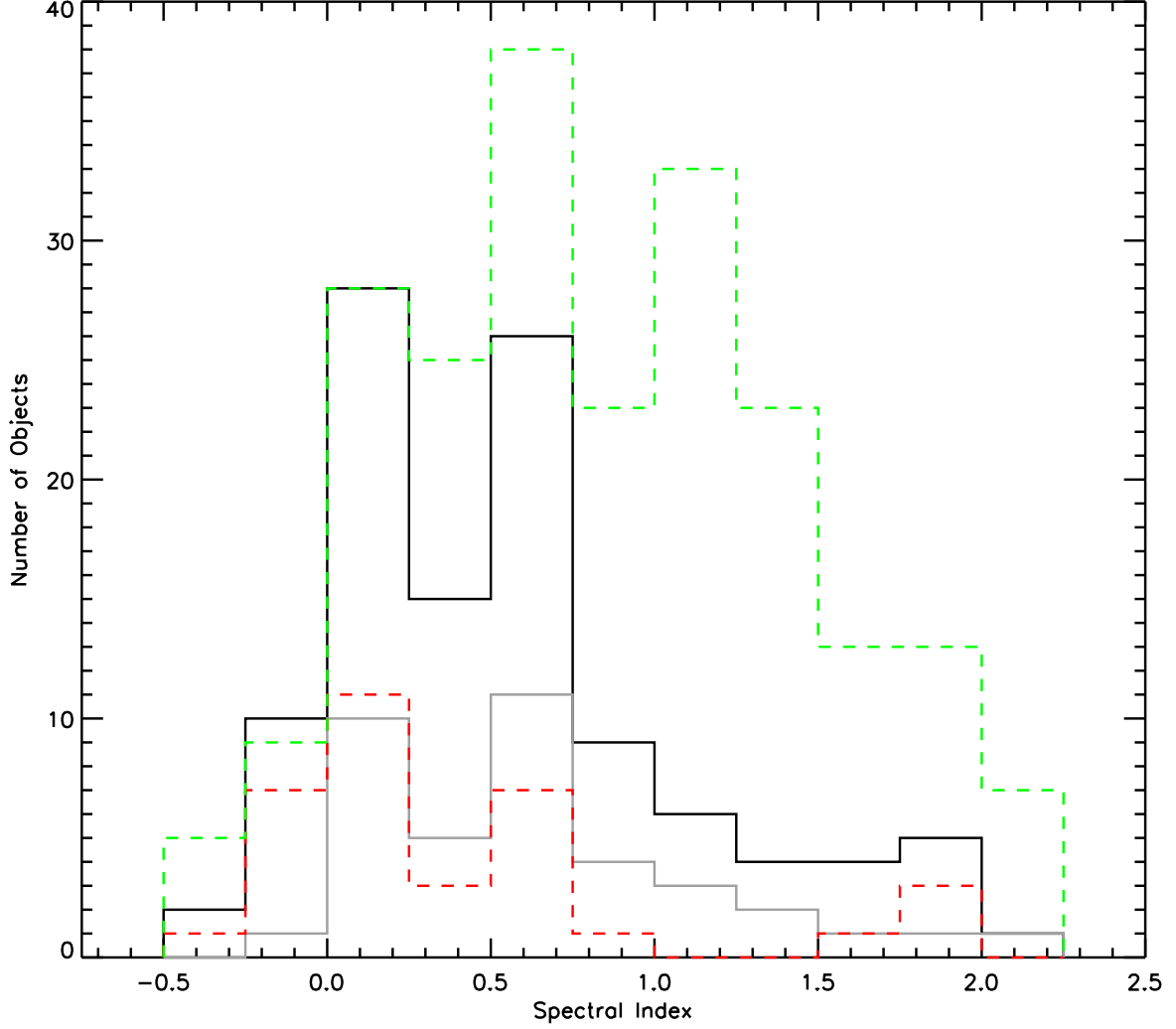


Fig. 1.— The spectral index distribution of this sample of Class I protostars based on $12\ \mu\text{m}$ to $100\ \mu\text{m}$ IRAS data. The median spectral index for the spectroscopically observed sample (in black) is $+0.5$. The red dashed histogram only includes spectroscopically observed targets in the Taurus, Perseus, and Auriga star forming regions. The solid gray histogram only includes spectroscopically observed targets in the Orion and Ophiuchus star forming regions. The green dashed histogram includes all objects presented in Connelley et al. (2008a). That sample has a median spectral index of $+0.79$, suggesting that the spectroscopically observed sample is more evolved.

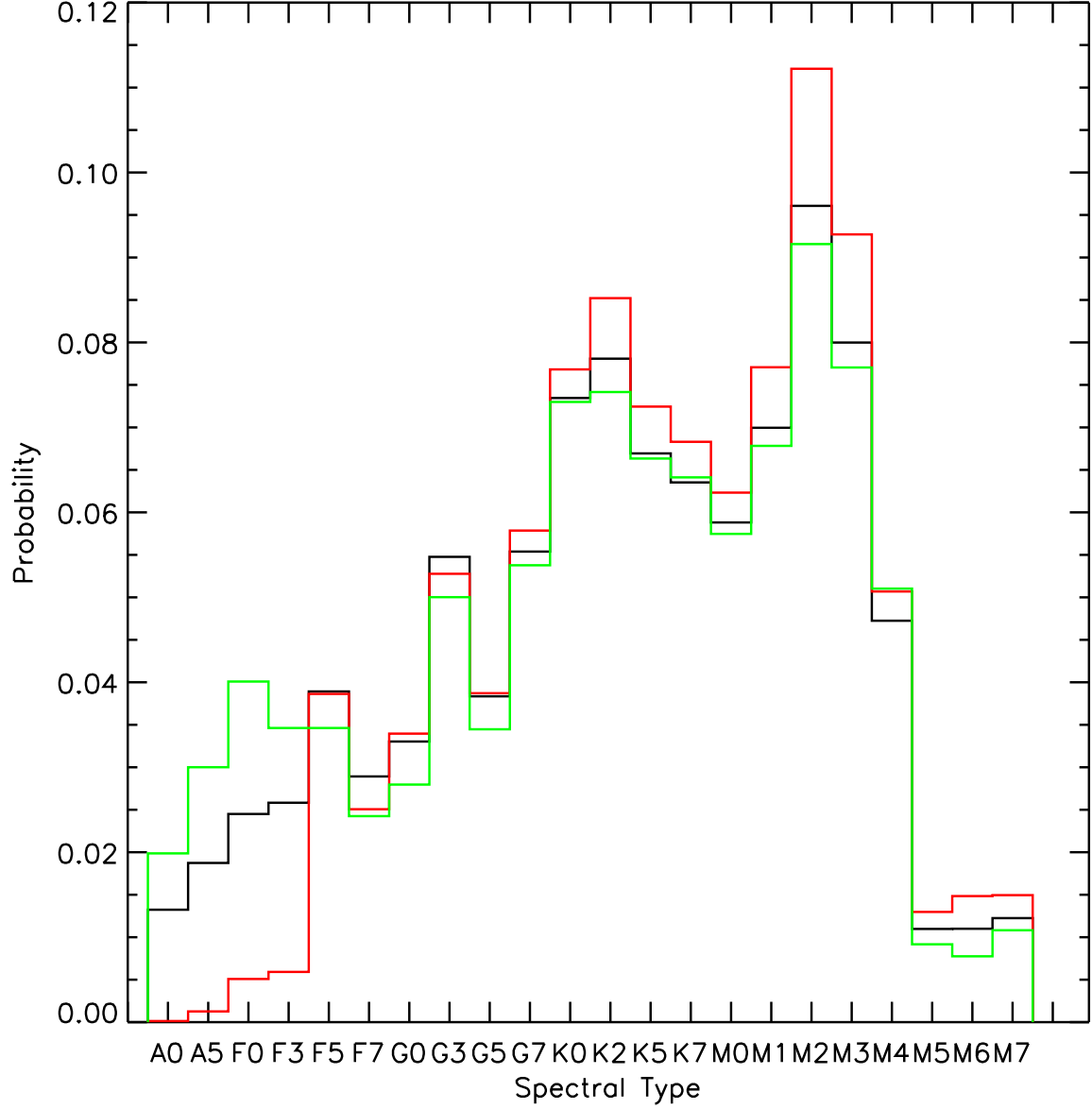


Fig. 2.— For Figures 2 and 3, the black histogram includes all targets, the red histogram only includes targets in the Taurus-Auriga and Perseus star forming regions, and the the green histogram only includes targets in the Orion and Ophiuchus star forming regions. This is an approximation of the distribution of photospheric spectral types for this sample of Class I YSOs. These histograms are the average the normalized goodness-of-fit curves from the spectral type fitting routine for all of the stars for which a photospheric spectral type could be estimated.

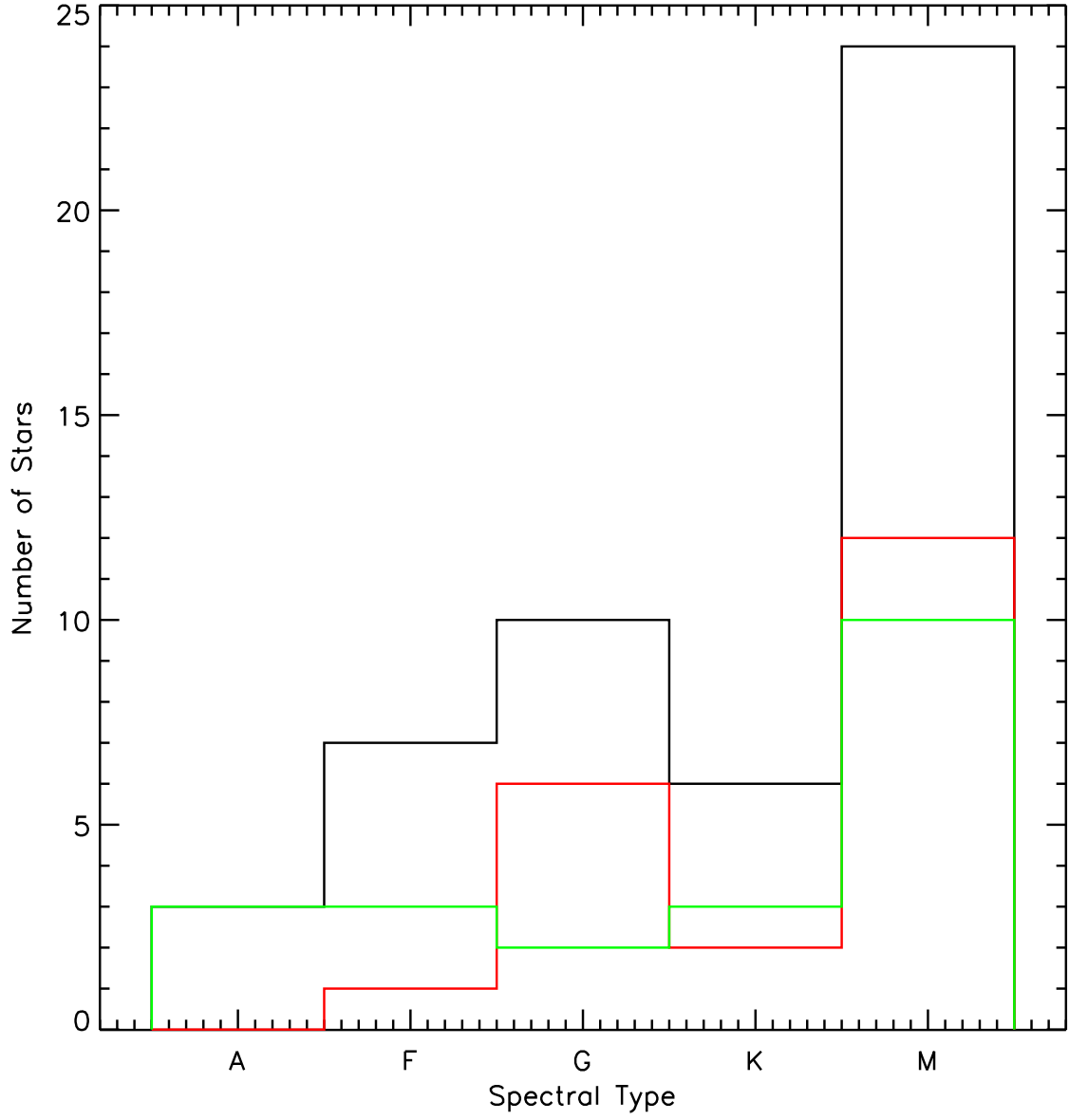


Fig. 3.— The distribution of the best-fit spectral types. This figure also clearly shows the dearth of early type Class I stars in the Taurus-Auriga and Perseus regions.

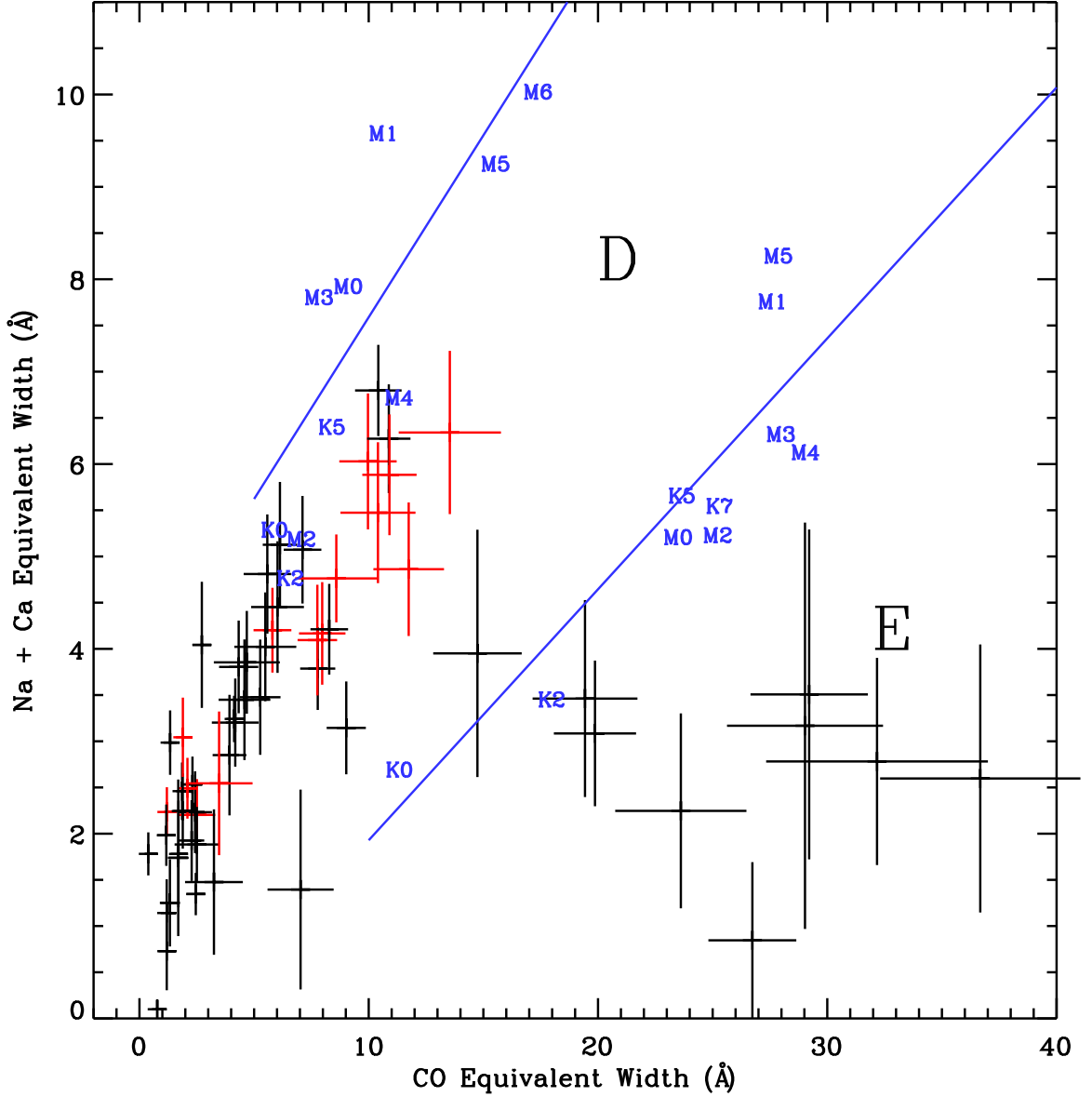


Fig. 4.— The equivalent width (EW) of lines of Na (2.206 μm and 2.209 μm) and Ca (2.263 μm and 2.266 μm) versus the CO band head starting at 2.294 μm . The upper spectral class designations are the data for dwarf (luminosity class V) stars, and the lower spectral class designations are for giant (luminosity class III) stars taken from the SpeX spectral library. The data for the YSOs are most consistent with dwarf stars (region D) with some additional CO absorption, possibly due to lower gravity. Veiling tends to push the EW values towards zero, leading to the trail of data points towards (0,0). The location of YSOs which have a triangular H-band continuum, an indicator sensitive to low gravity, are shown in red. There are also a number of YSOs with strong CO absorption, found to the right of the figure (region E), which are FU Orionis-like stars.

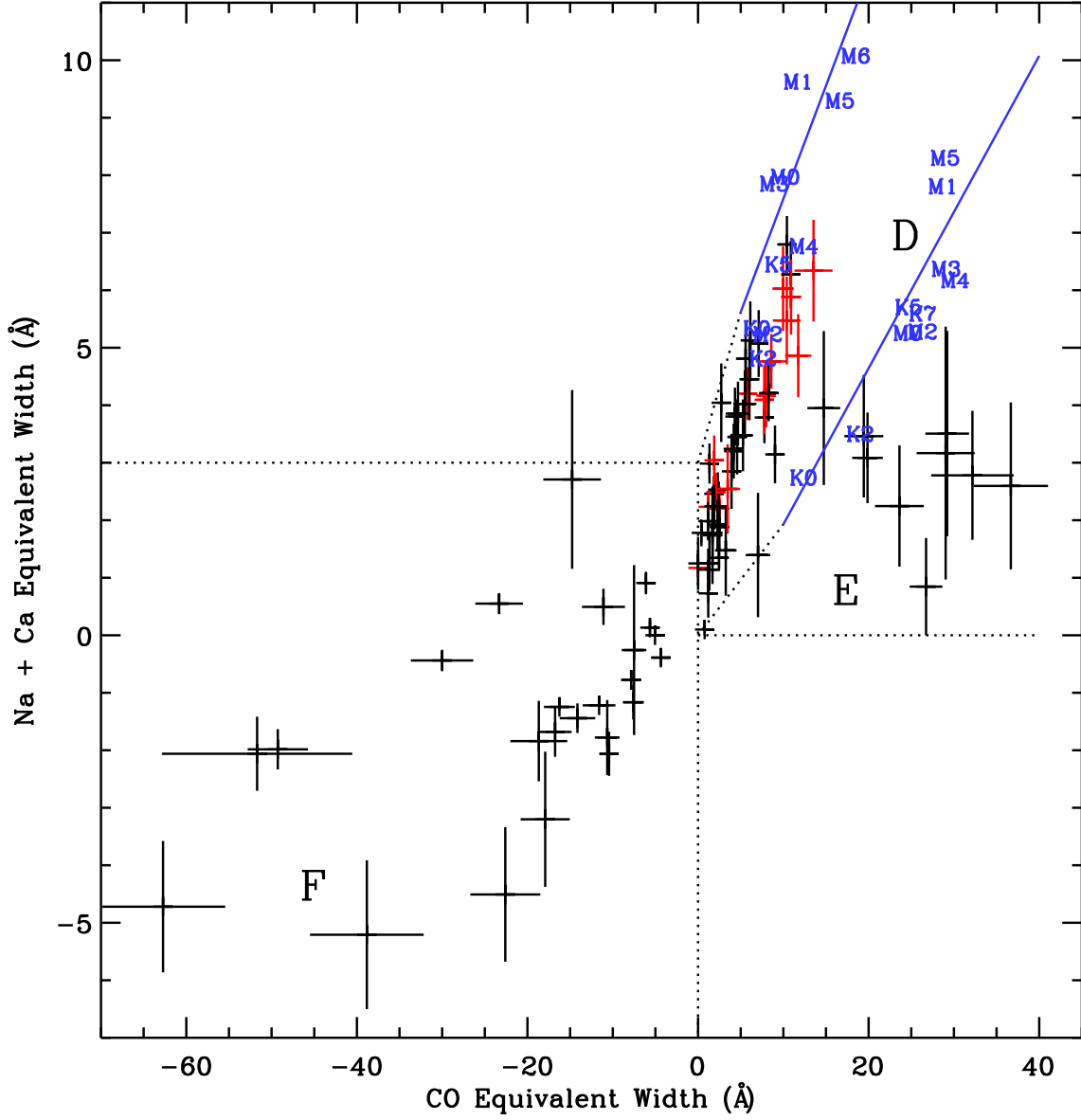


Fig. 5.— This shows the full range of CO values, including those objects where CO is in emission (region F). When CO is seen in emission, then Na is usually also in emission. Calcium is not seen in emission, but in these cases the veiling is too high to see it in absorption.

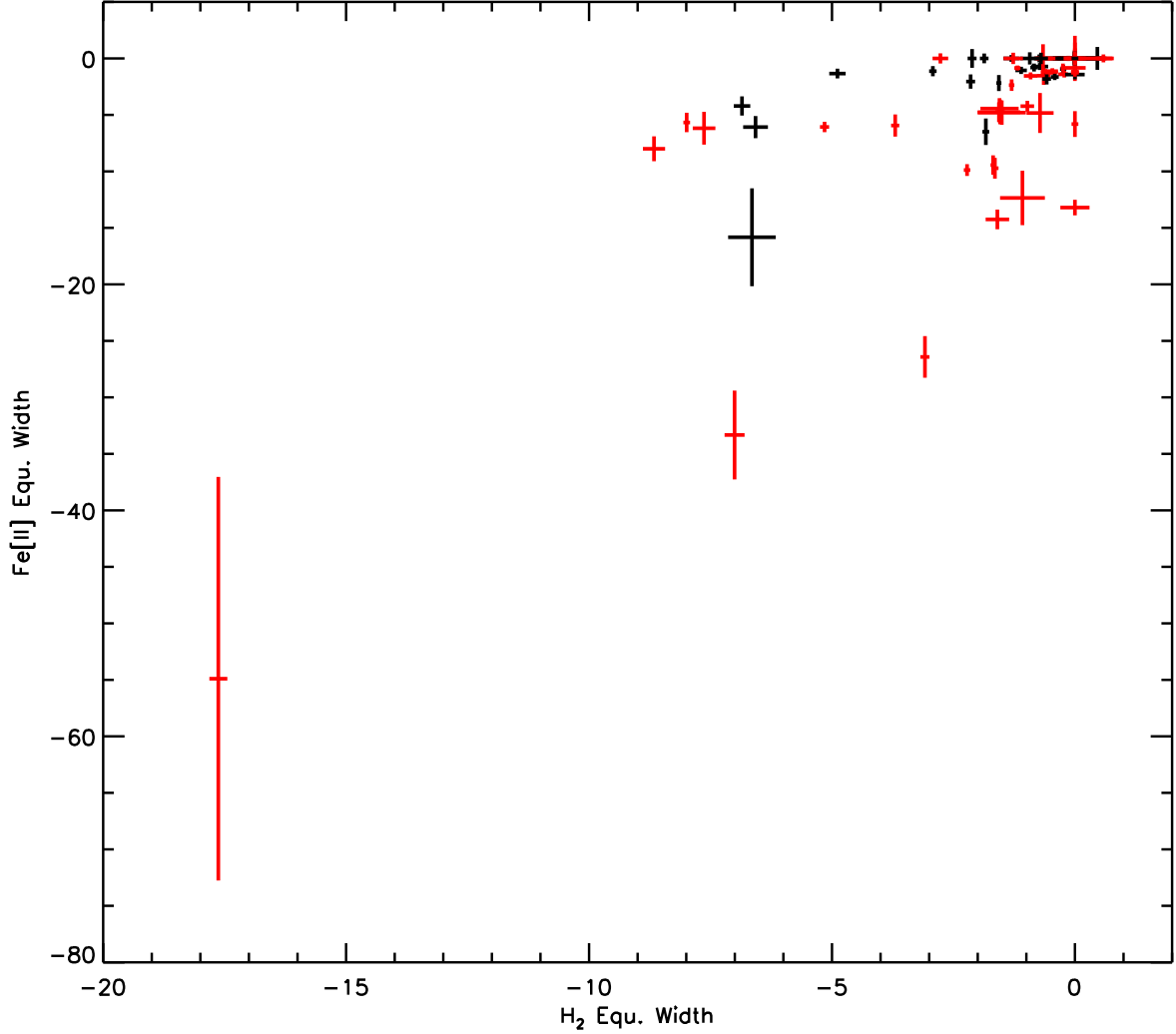


Fig. 6.— The equivalent width of the [Fe II] line at 1.644 μm versus the H₂ S(1) v=1-0 line at 2.122 μm . The red error bars are for targets with high veiling and the black error bars are for targets with low veiling. Targets with low veiling have a lower average [Fe II] and H₂ EWs compared to targets with high veiling. For targets with low veiling, few targets have a [Fe II] EW less than -6 Å and the H₂ EW less than -3 Å. We detected [Fe II] emission from all targets with H₂ EW less than -3 Å.

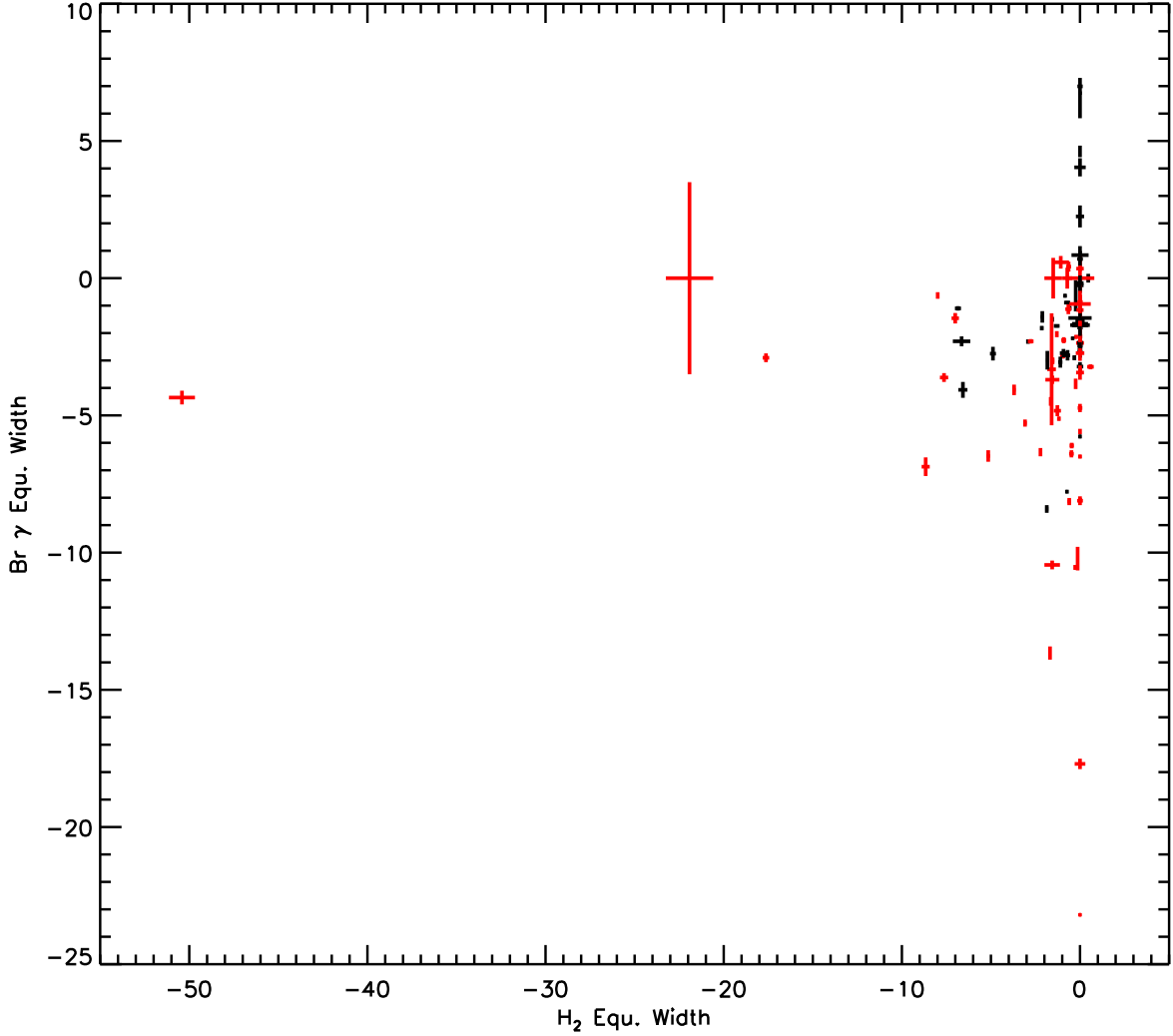


Fig. 7.— The equivalent width of the Br γ line versus the H₂ S(1) v=1-0 line at 2.122 μ m. The red error bars are for targets with high veiling and the black error bars are for targets with low veiling. For targets with low veiling, few targets have a Br γ EW less than -5 Å and the H₂ EW less than -3 Å. The limit of the Br γ line EW versus the H₂ EW appears to be bound by a hyperbolic relation, where the maximum Br γ line EW is roughly 50 divided by the H₂ EW. This suggests that these emission lines, and thus their excitation mechanisms, may be inversely correlated to each other.

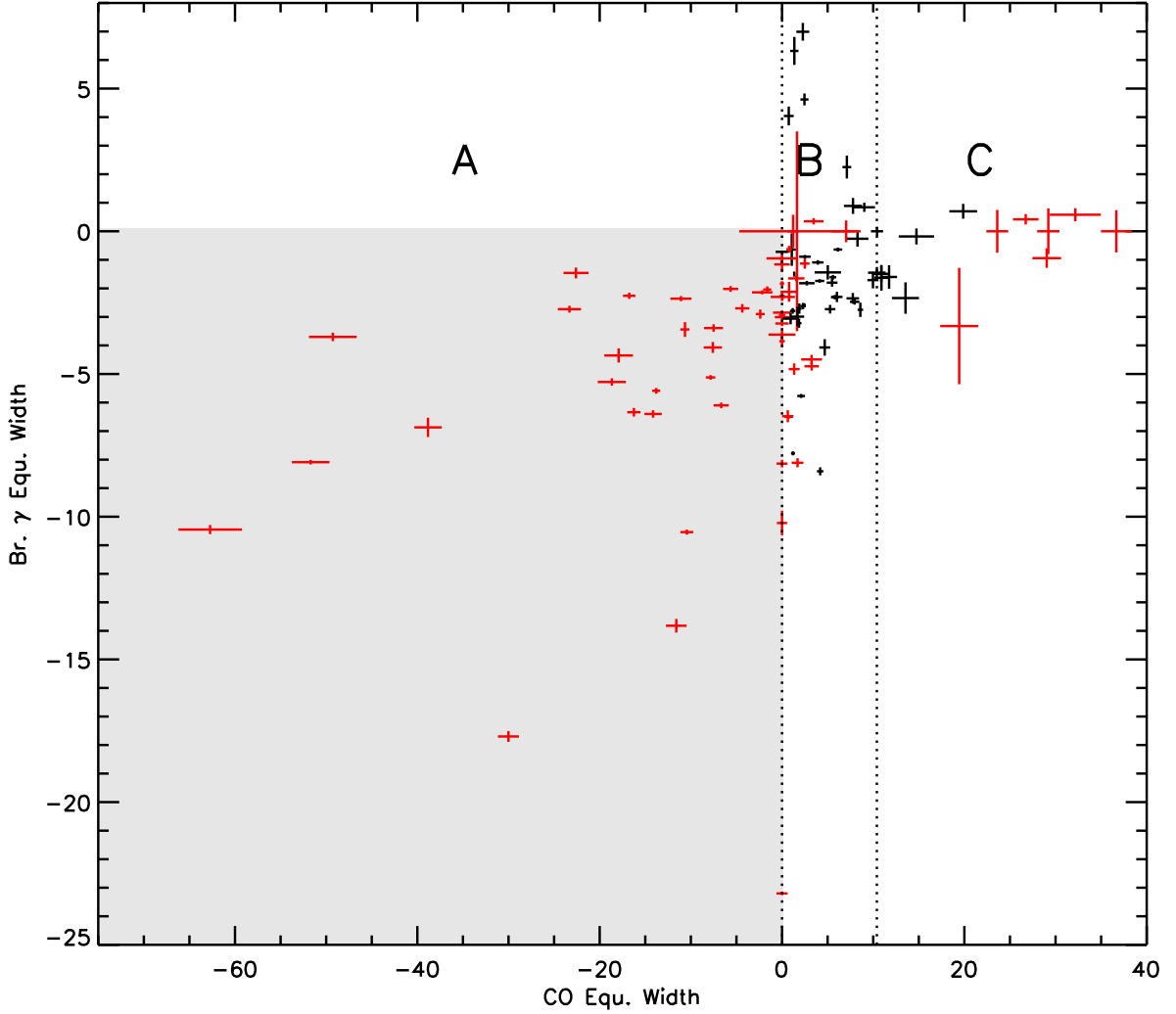


Fig. 8.— This figure shows the relationship between the equivalent widths of the Br γ line and the first CO band head at $2.293 \mu\text{m}$. These lines are close enough that differences in veiling and extinction effects are ignored. The dotted lines divide the figure into three regions. Region A is where the CO band heads are in emission. In this region, Br γ is *always* seen in emission (the gray shaded area), and never in absorption. Region B is where the CO equivalent widths are consistent with main-sequence photospheric absorption. In this region, Br γ is often seen in emission, but it can be undetected or seen in absorption. Region C is where the CO equivalent widths are greater than is expected from a photosphere. In this region, Br γ is very rarely seen in emission, and only very weakly. Targets with high veiling (red) are clearly segregated from targets with low veiling (black), such that only targets with high veiling have CO emission or strong CO absorption (i.e. FU Orionis-like objects).

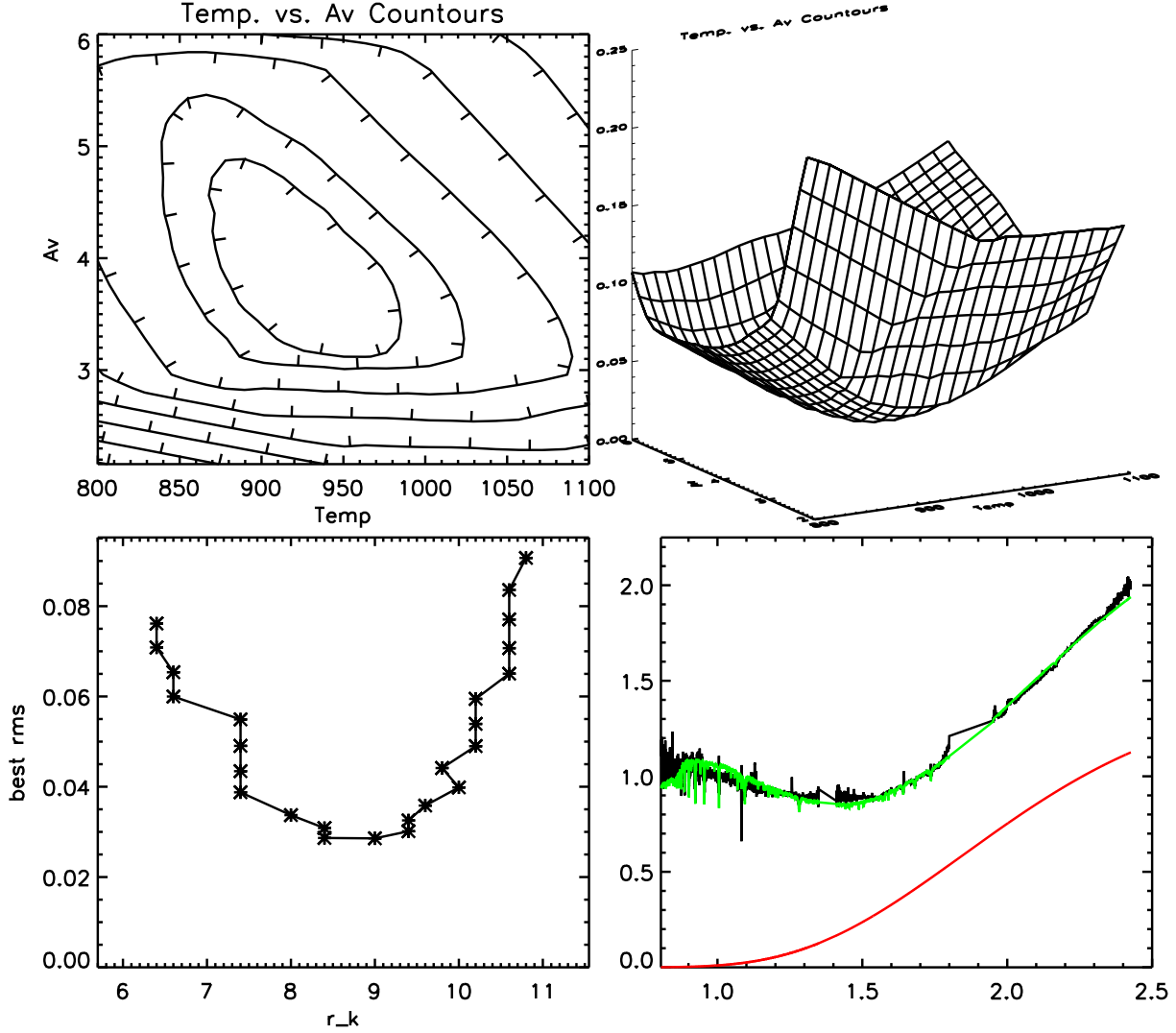


Fig. 9.— An example of the output of our continuum modeling code. The upper left panel shows the RMS fit contours as a function of extinction (A_v) and veiling temperature. The upper right panel shows the same data as a surface. The lower left panel shows the best fit's RMS value versus the amplitude of the veiling (r_k). The lower right panel shows the observed spectrum (black) with the modeled spectrum (green) overlaid. The red curve is a single temperature blackbody using the best fit veiling temperature, but not scaled according to the best fit r_k . This is the result for IRAS 22324+4024.

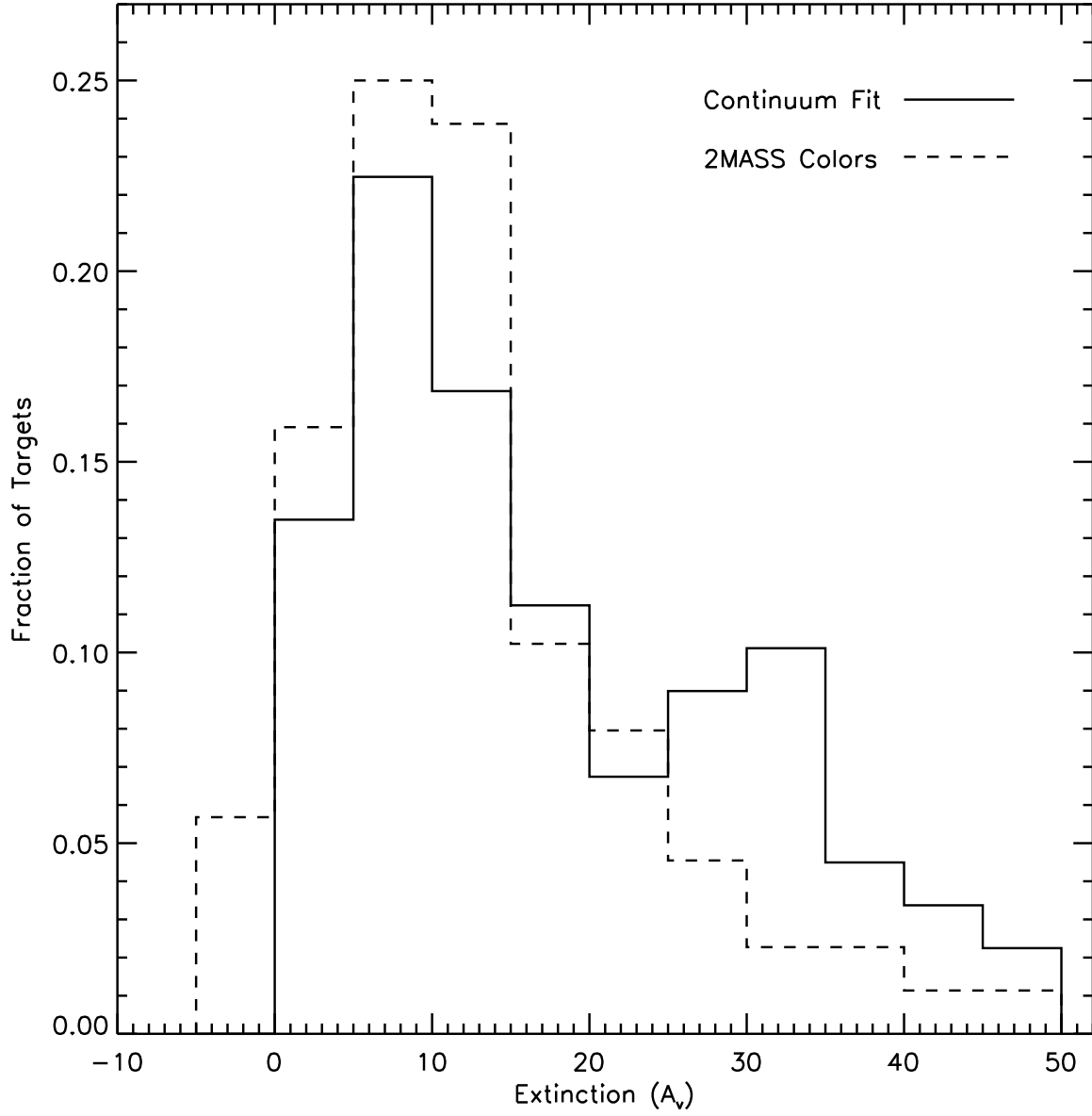


Fig. 10.— Histogram of our extinction estimates (A_v) based on our continuum modeling routine (solid line) and 2MASS photometry (dashed line).

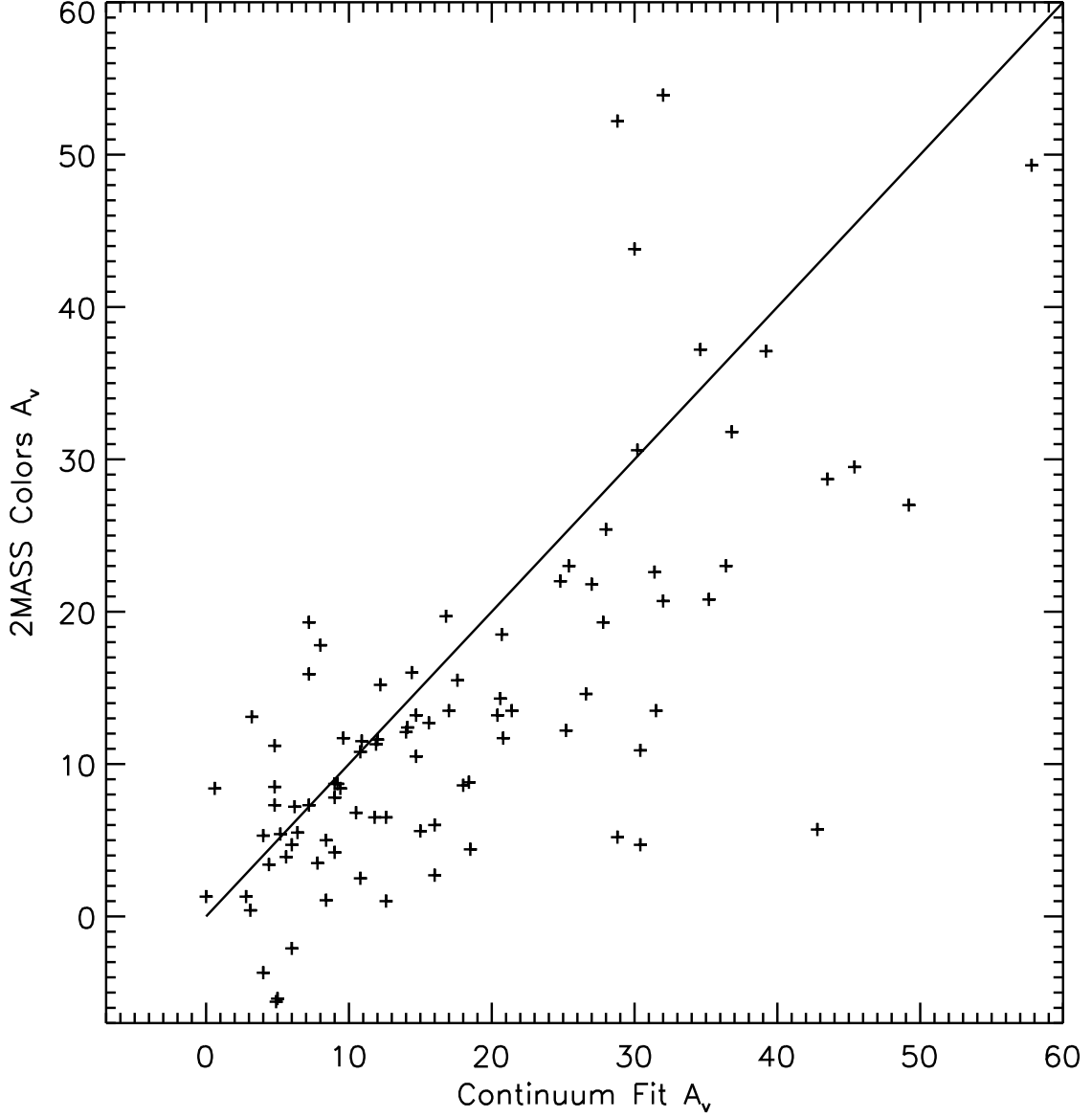


Fig. 11.— Plotting our A_v estimates based on continuum modeling and 2MASS colors against each other. The solid line has a slope of 1 and represents the ideal location of the data points on this plot. The extinction estimates based on 2MASS photometry tends to be $\sim 30\%$ lower than the extinction estimate based on continuum modeling. Error bars are not shown for clarity.

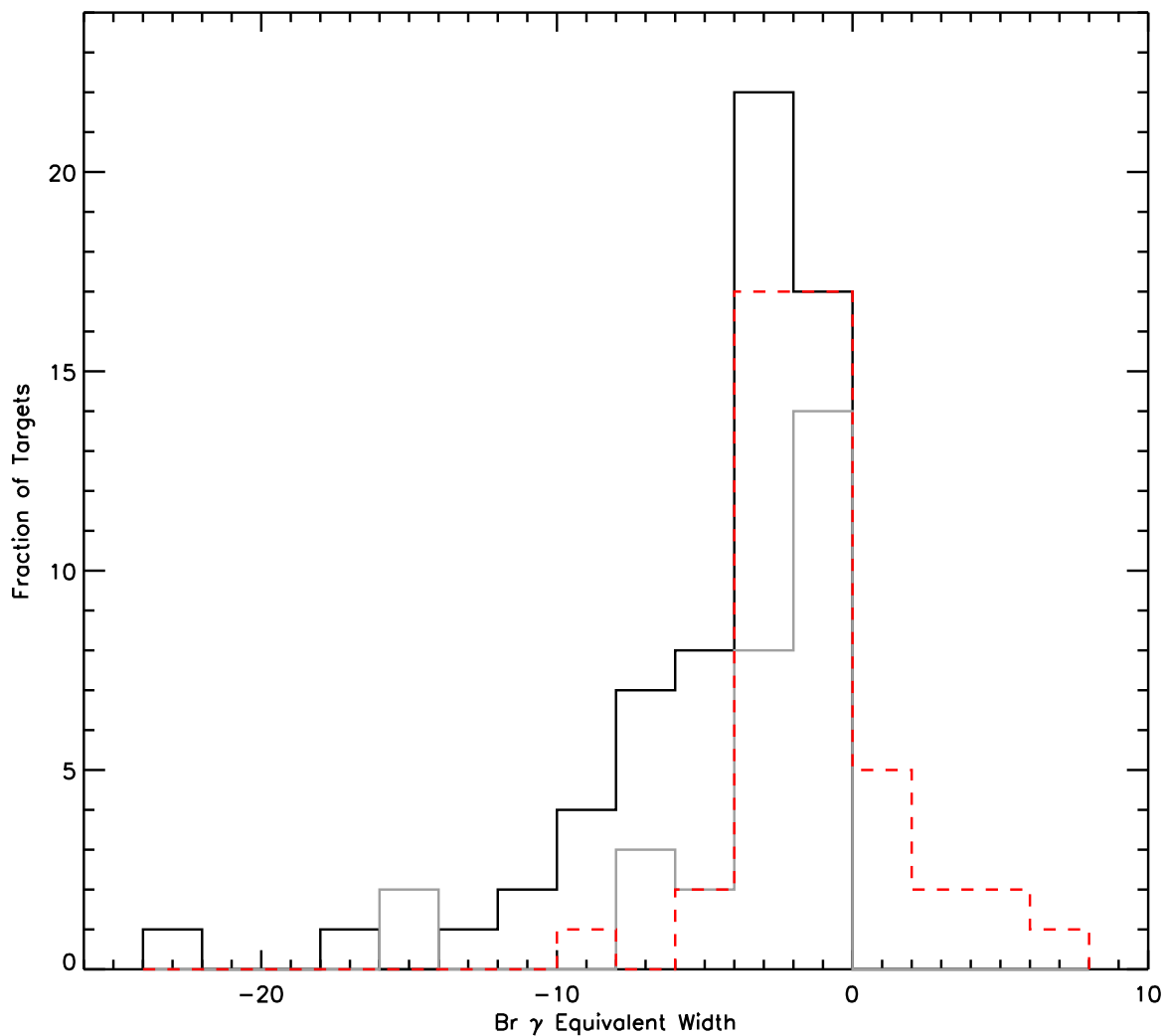


Fig. 12.— The distribution of the Br γ equivalent widths, divided between targets with high veiling (black solid line) and low veiling (red dashed line). The grey solid line shows the Br γ equivalent width histogram for the T Tauri stars in Muzerolle et al. (1998) for comparison.

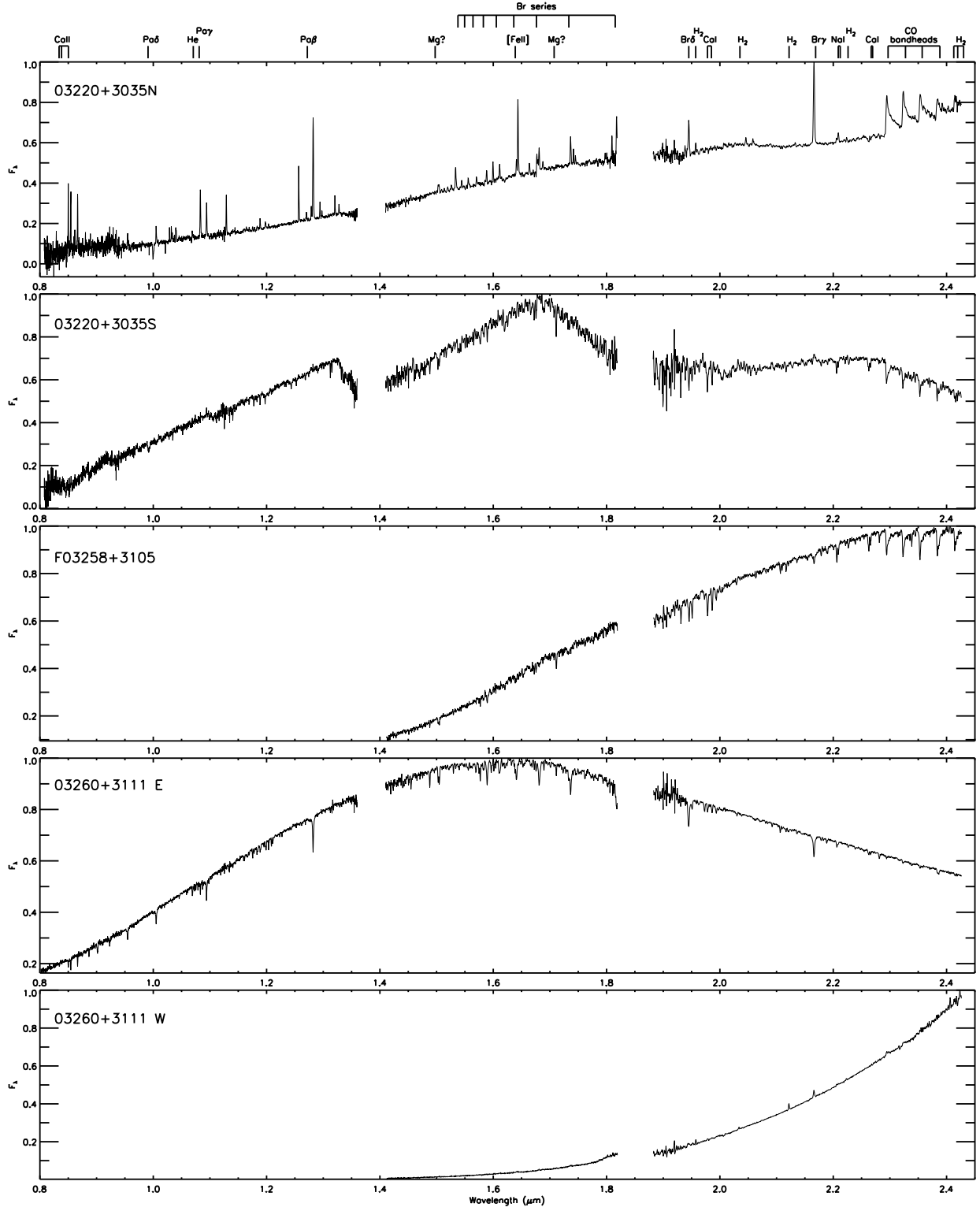


Fig. 13.— 0.80 to 2.43 μm spectra of our sources.

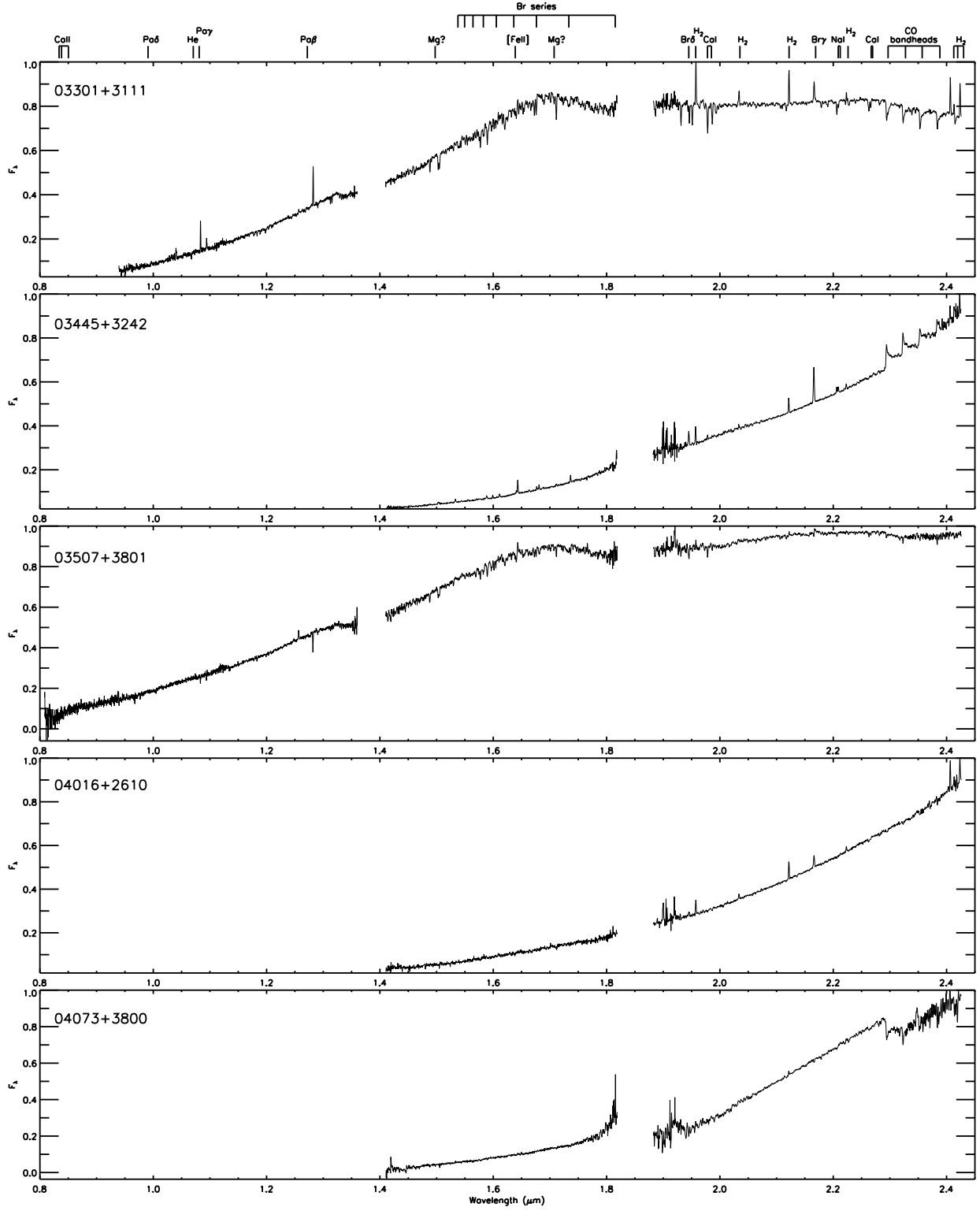


Fig. 13.— 0.80 to 2.43 μm spectra of our sources.

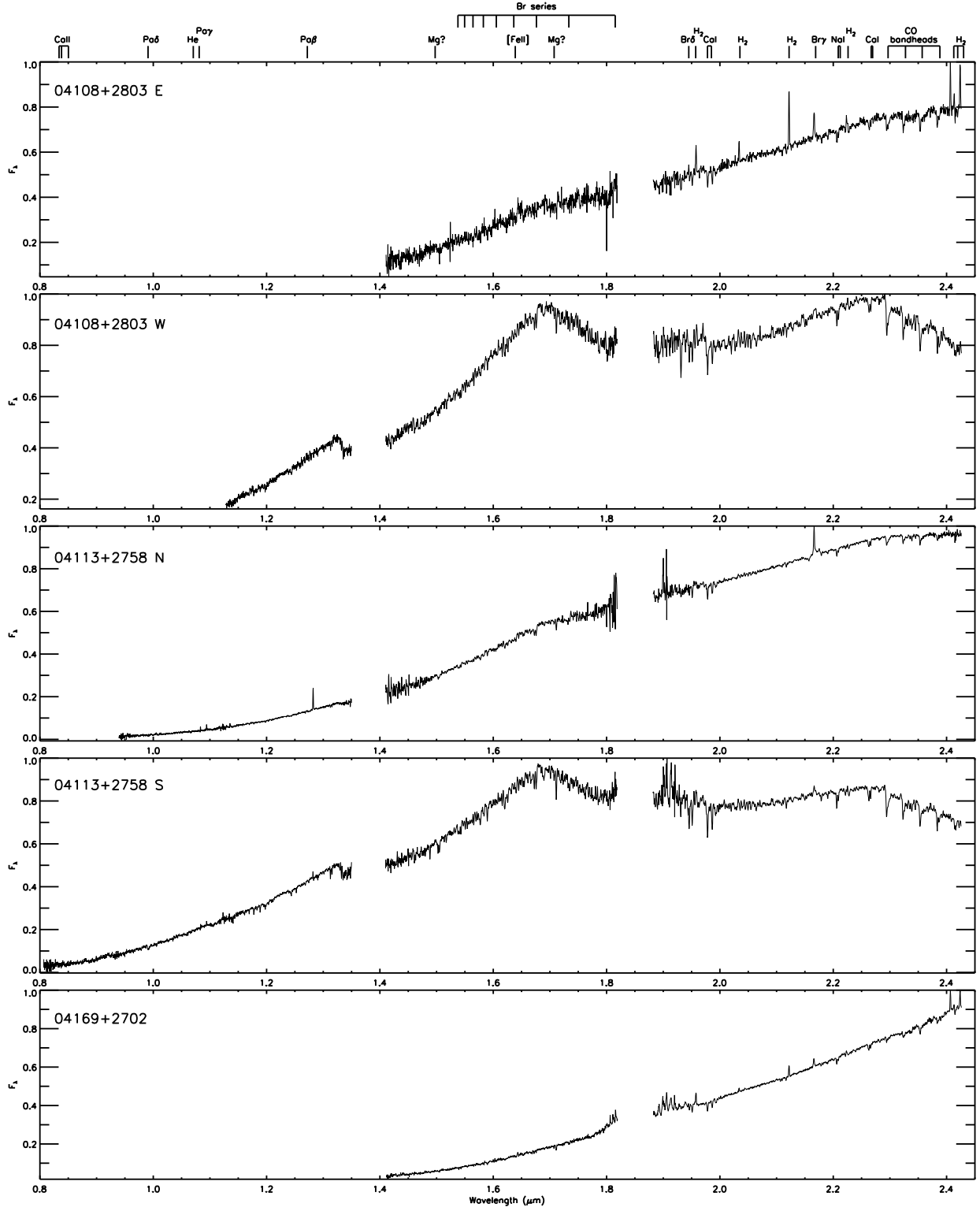


Fig. 13.— 0.80 to 2.43 μm spectra of our sources.

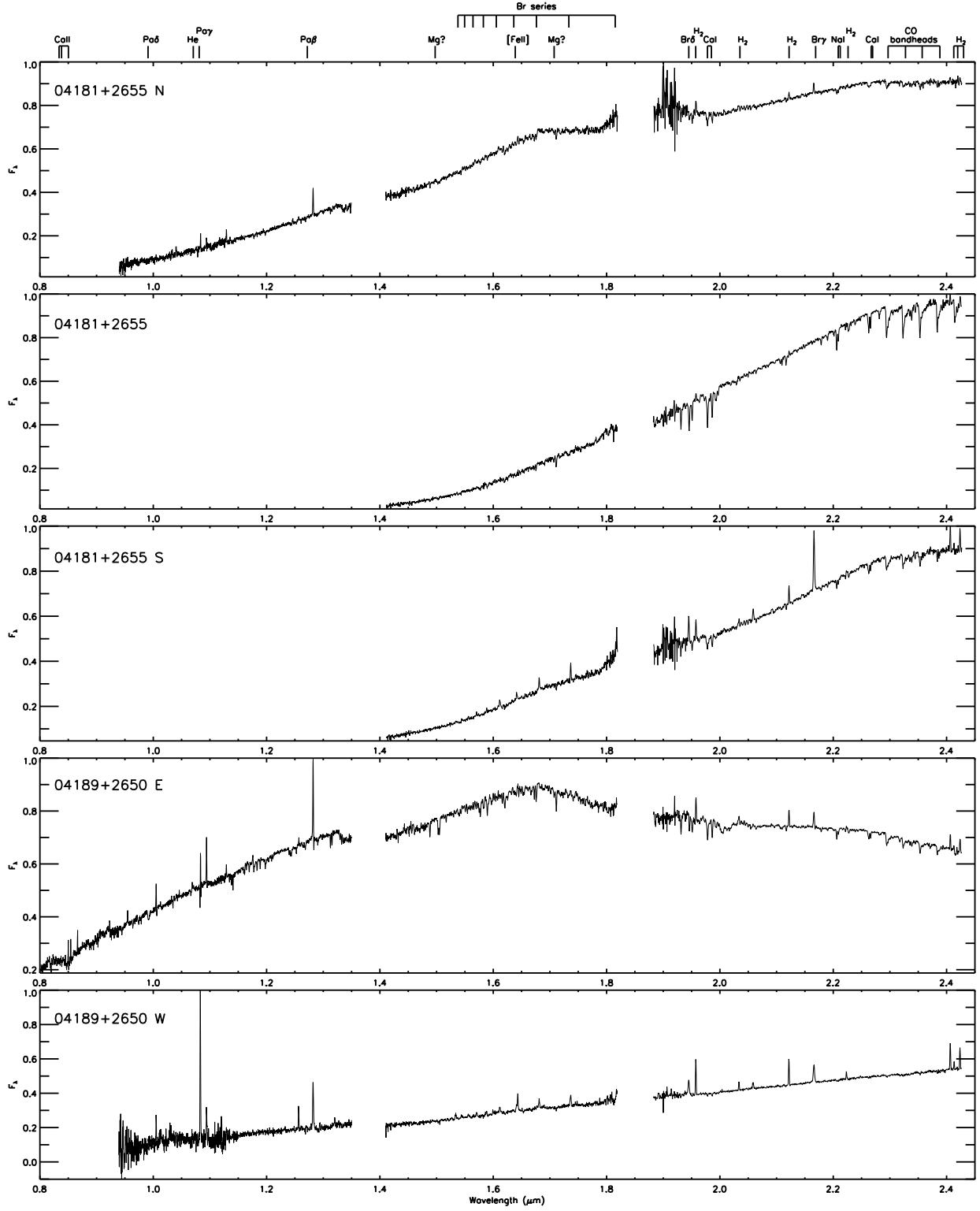


Fig. 13.— 0.80 to 2.43 μm spectra of our sources.

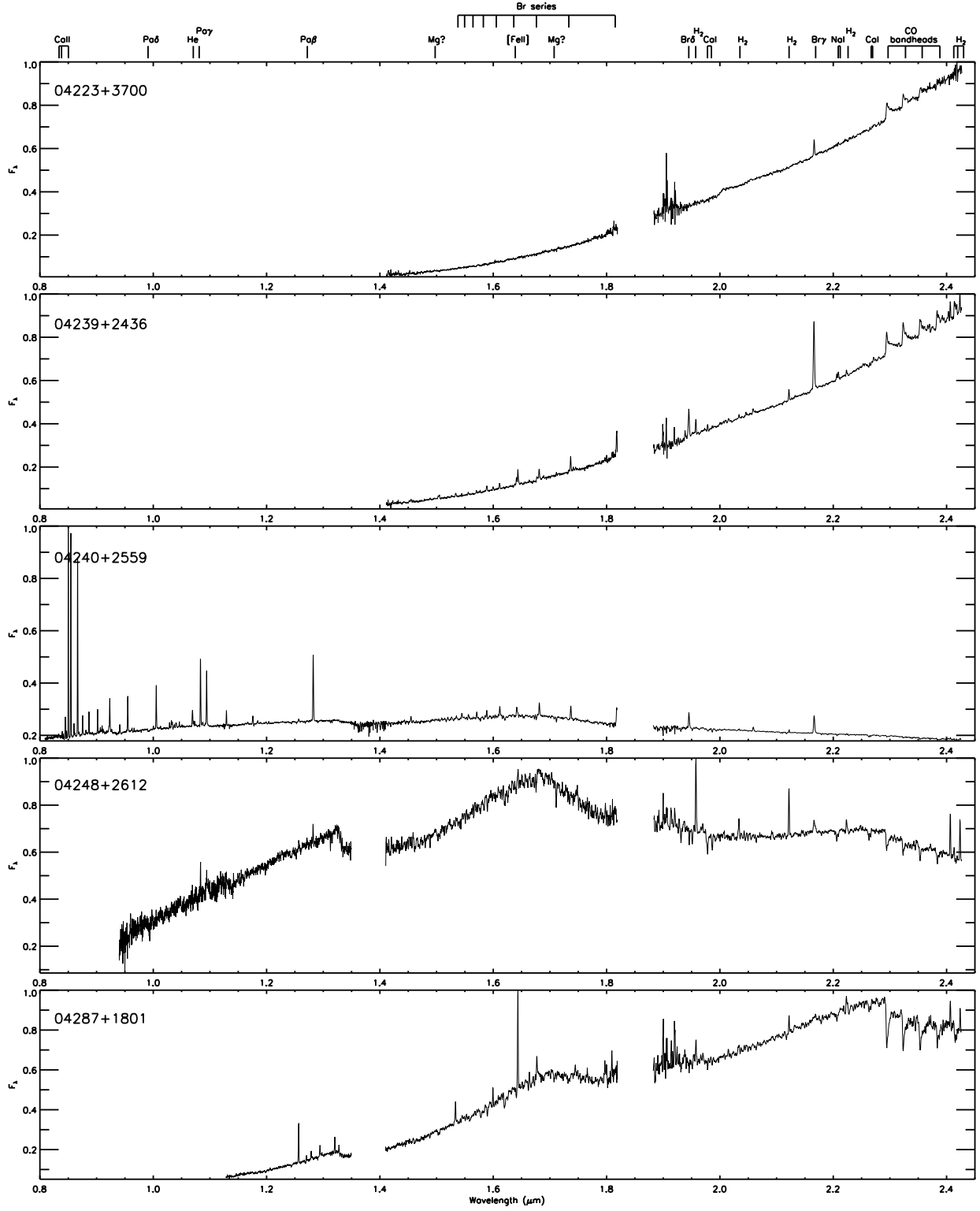


Fig. 13.— 0.80 to 2.43 μm spectra of our sources.

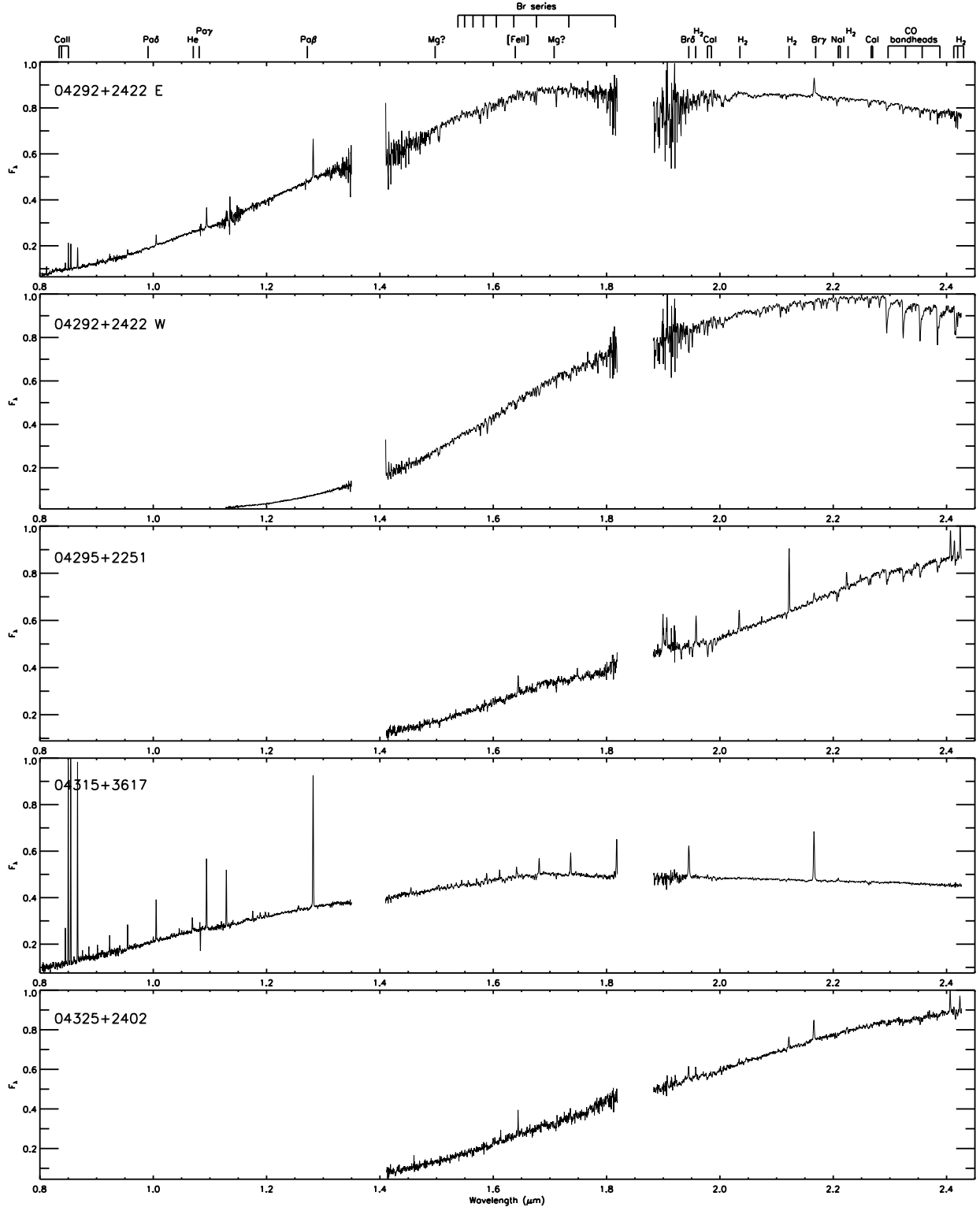


Fig. 13.— 0.80 to 2.43 μm spectra of our sources.

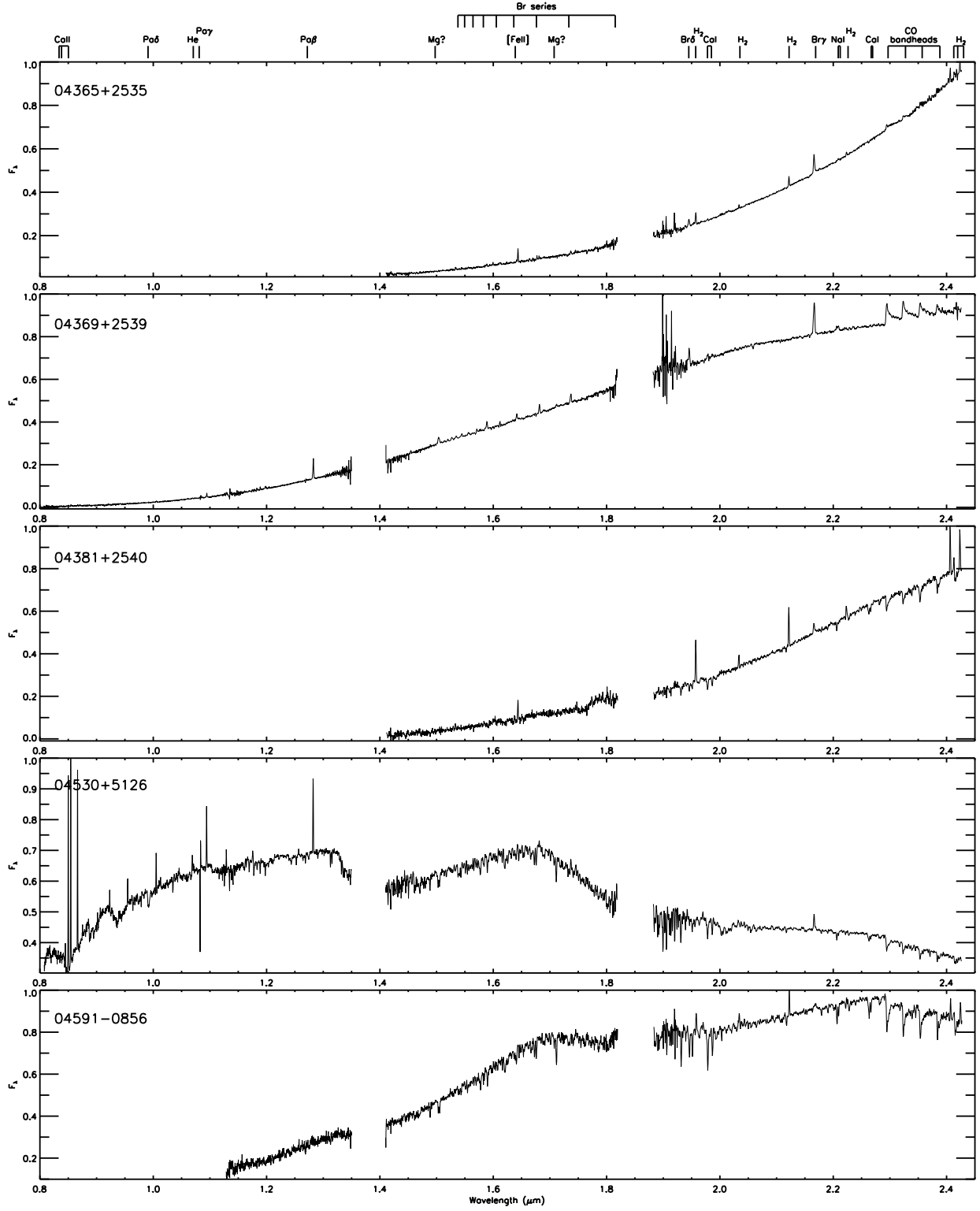


Fig. 13.— 0.80 to 2.43 μm spectra of our sources.

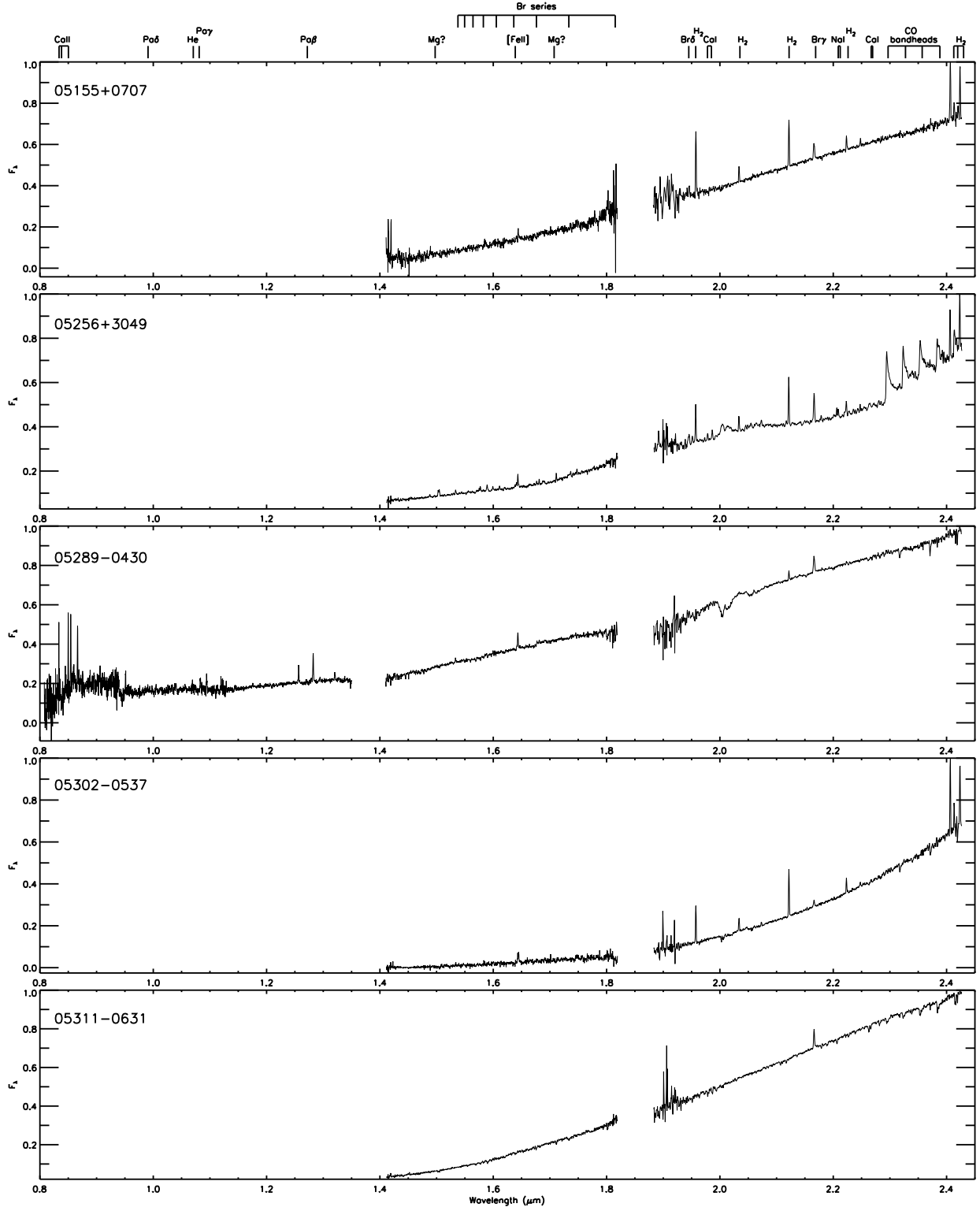


Fig. 13.— 0.80 to 2.43 μm spectra of our sources.

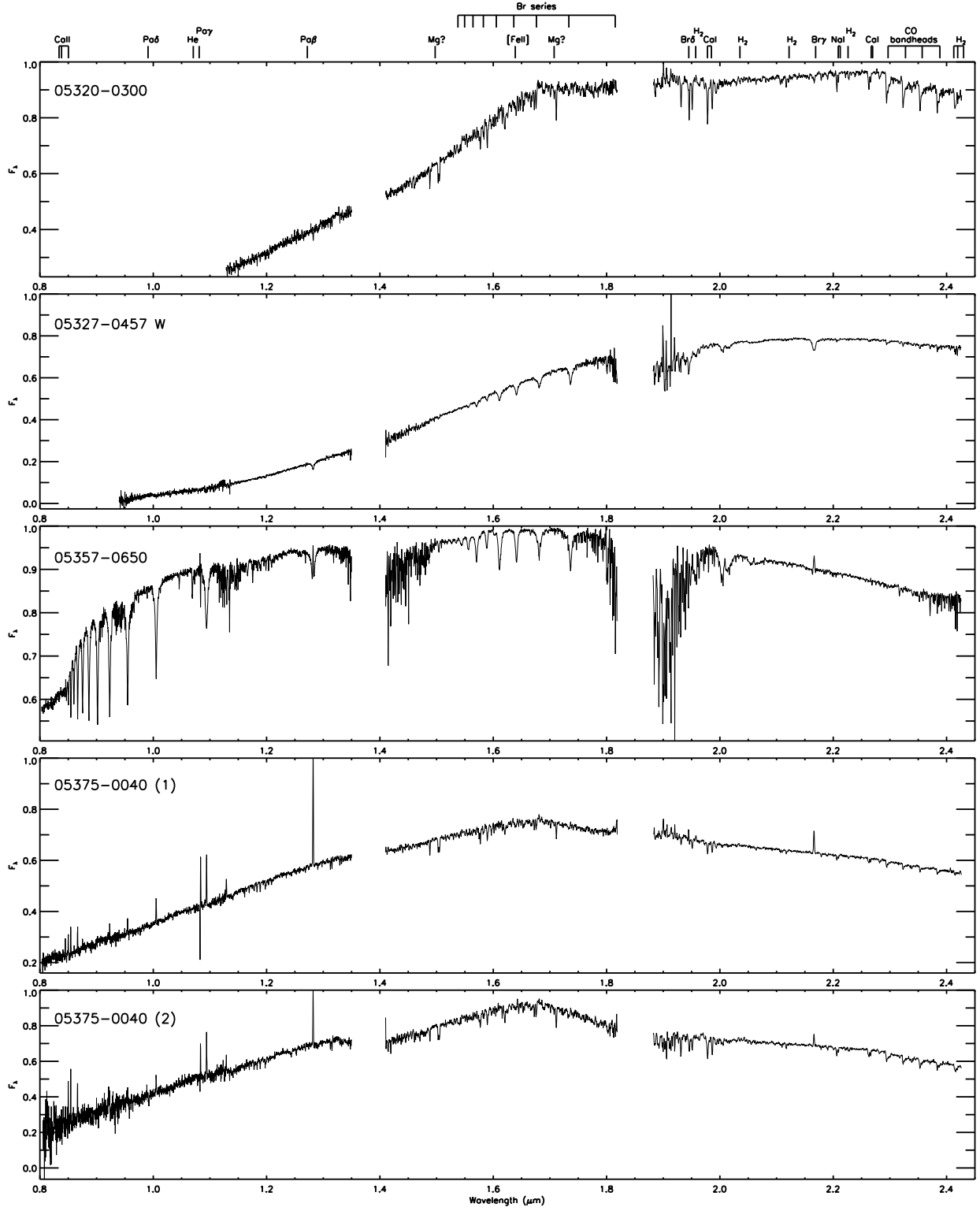


Fig. 13.— 0.80 to 2.43 μm spectra of our sources.

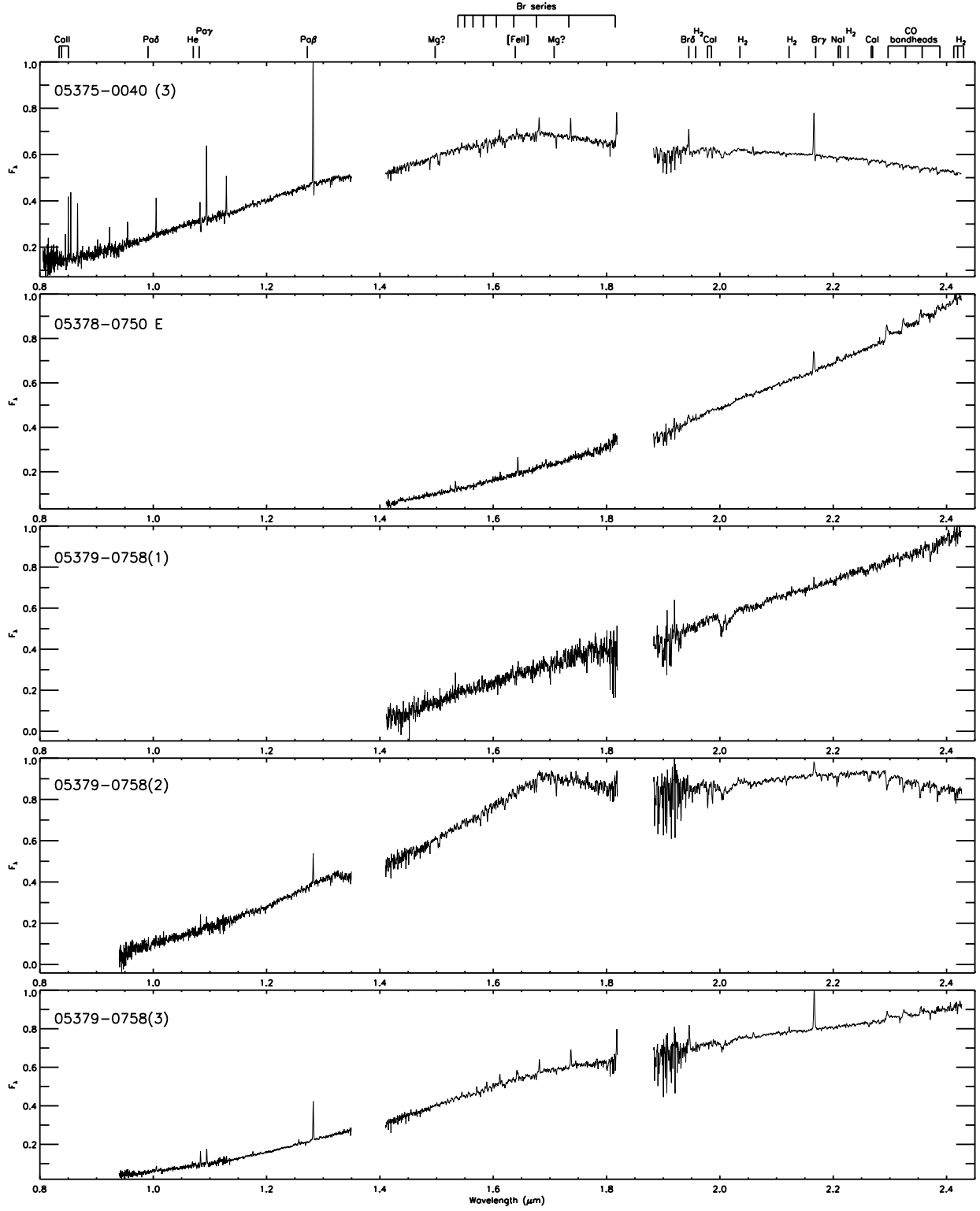


Fig. 13.— 0.80 to 2.43 μm spectra of our sources.

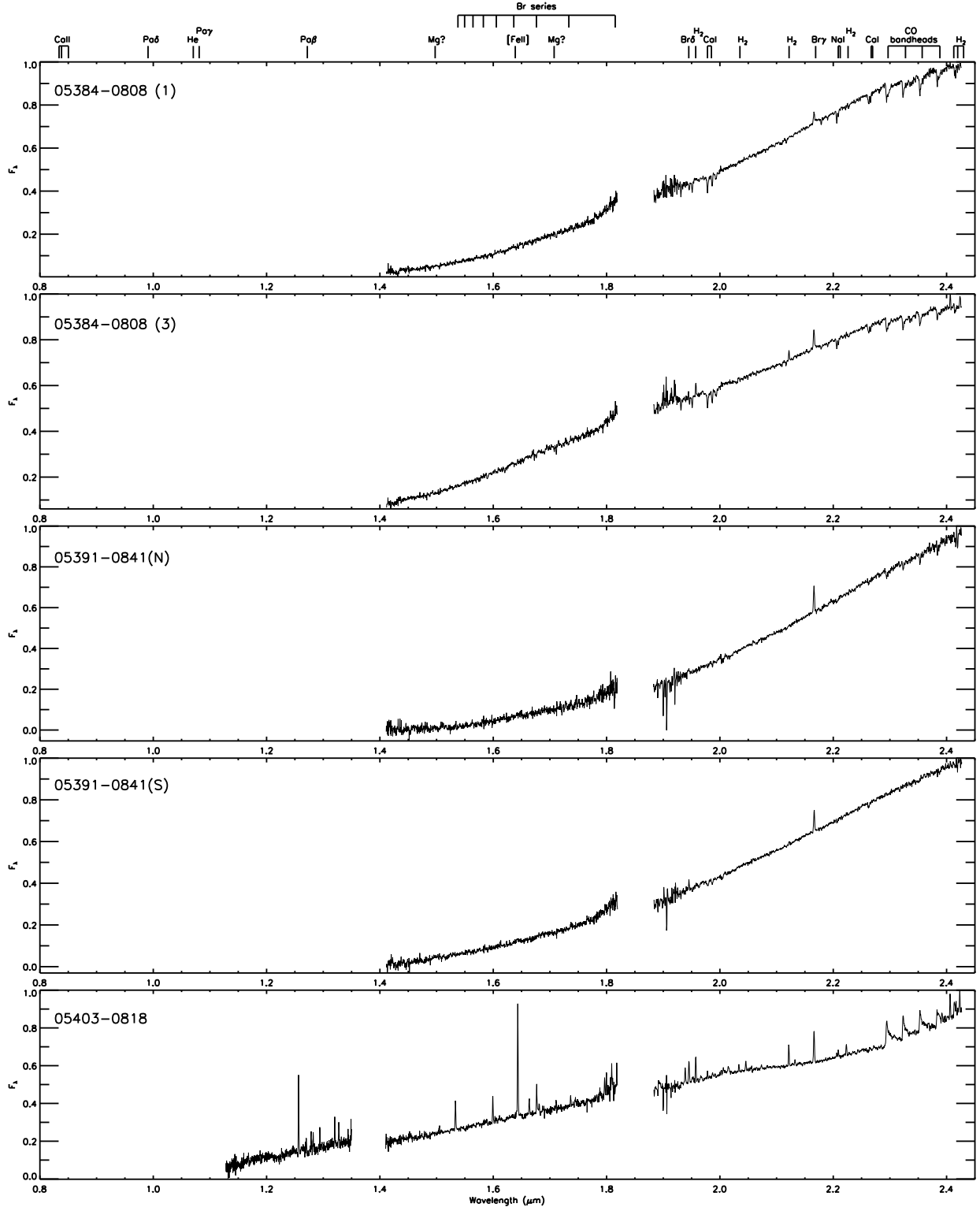


Fig. 13.— 0.80 to 2.43 μm spectra of our sources.

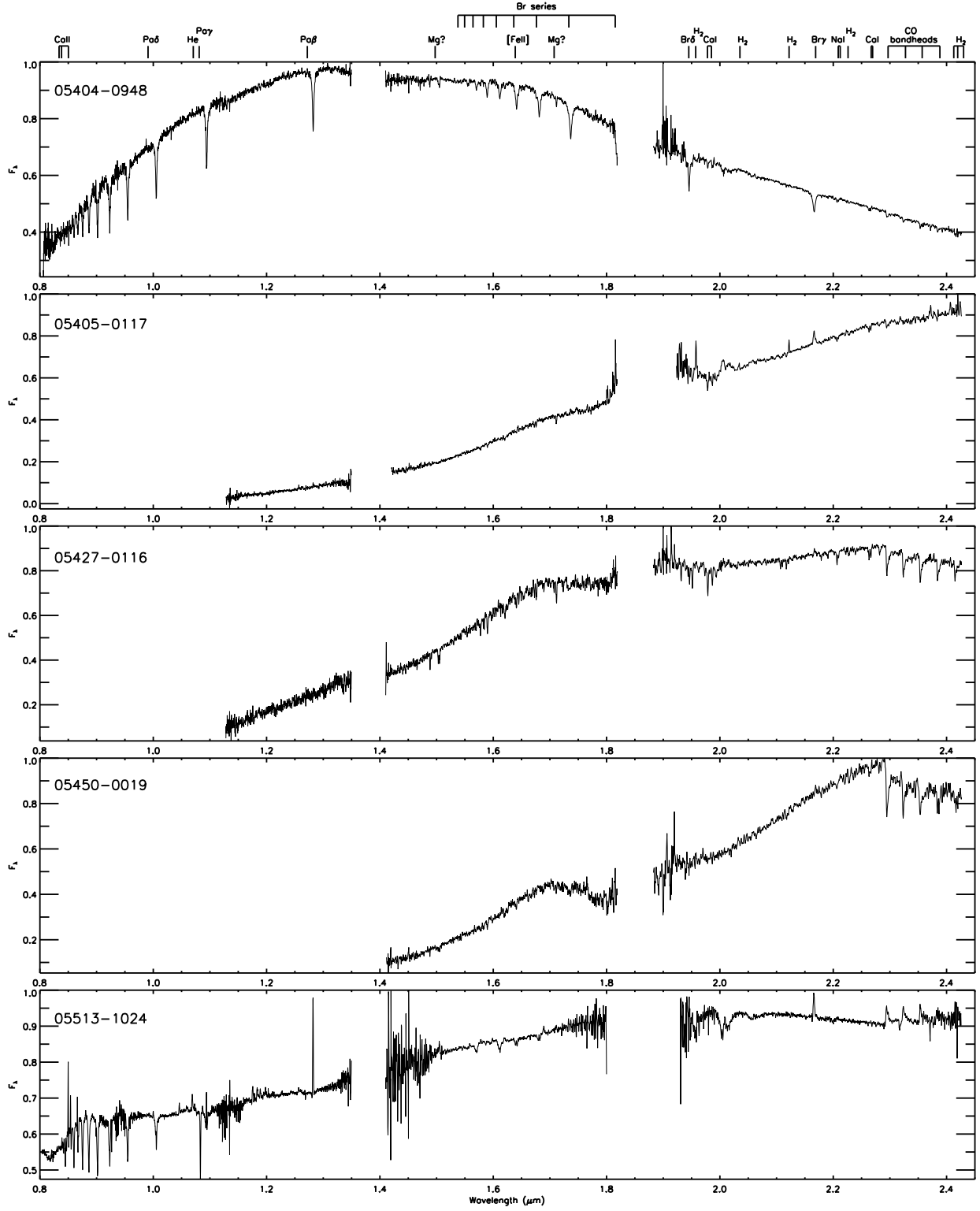


Fig. 13.— 0.80 to 2.43 μm spectra of our sources.

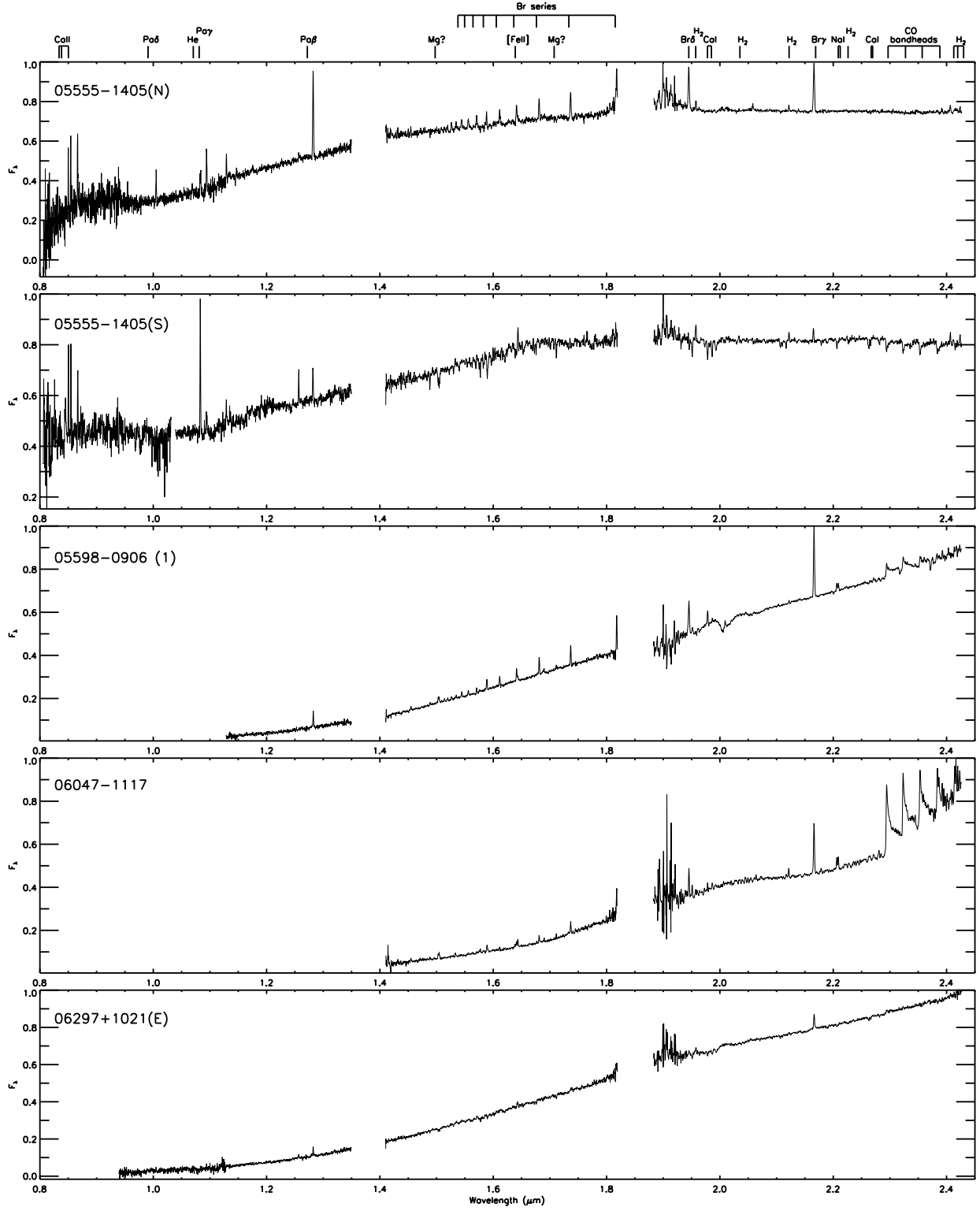


Fig. 13.— 0.80 to 2.43 μm spectra of our sources.

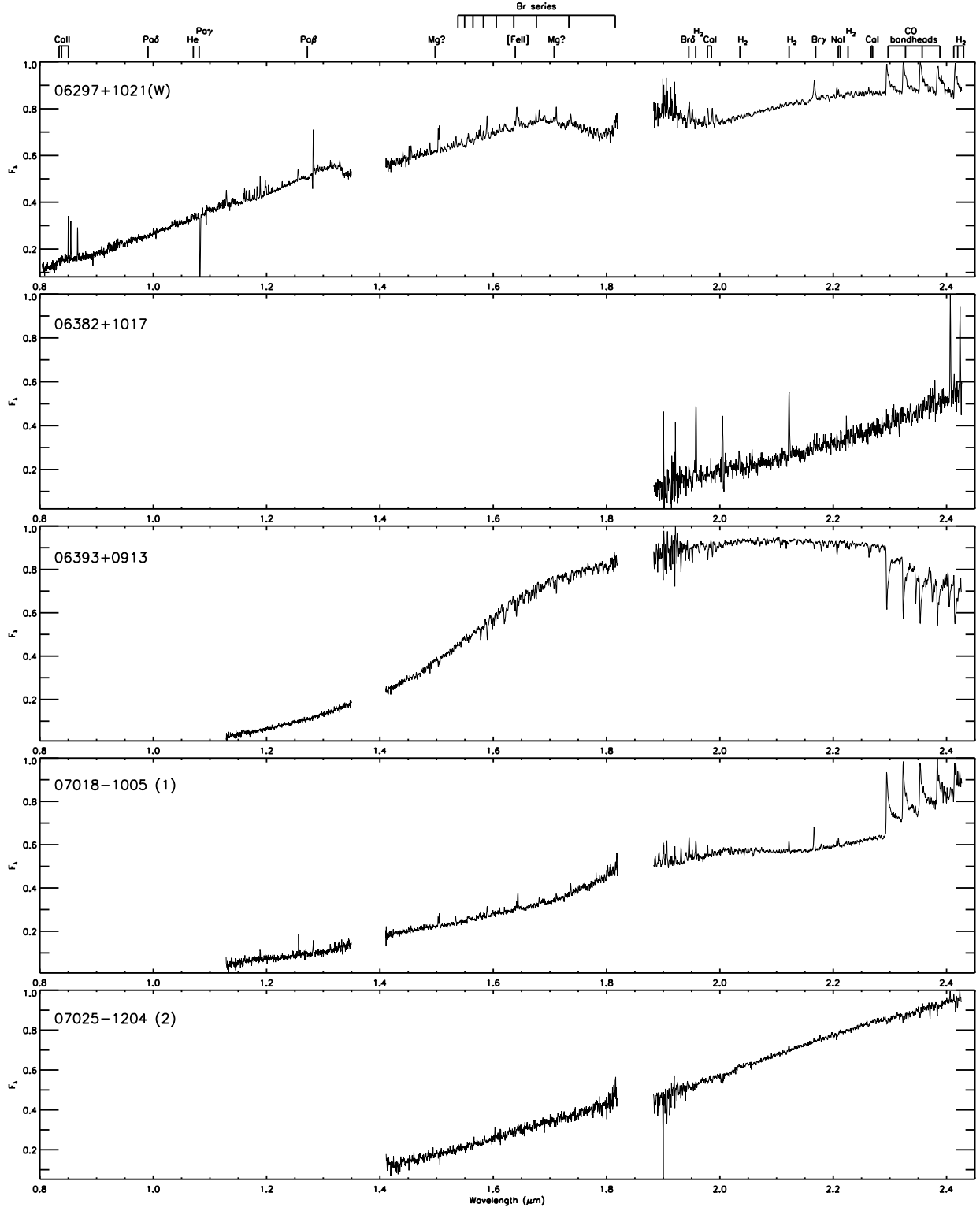


Fig. 13.— 0.80 to 2.43 μm spectra of our sources.

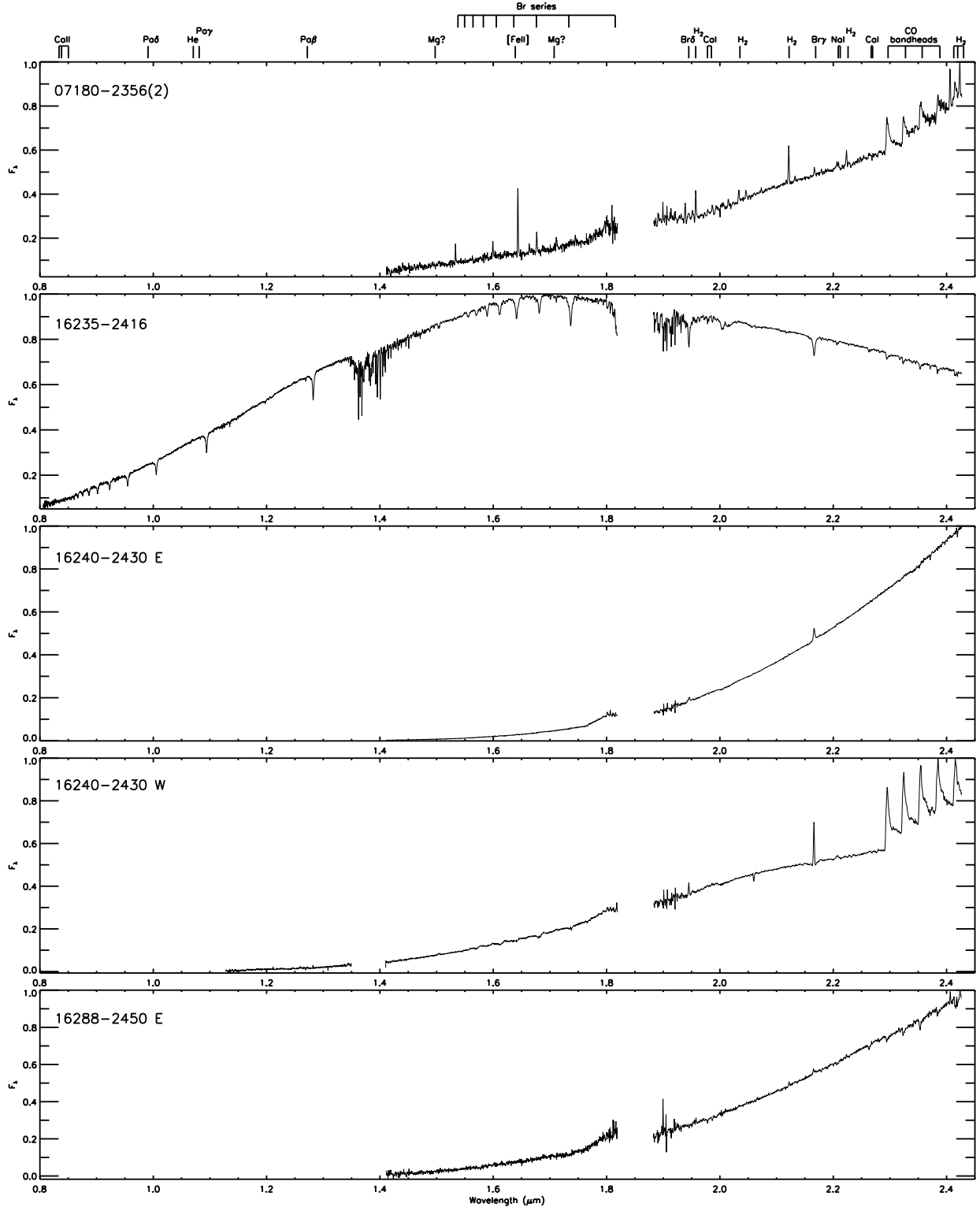


Fig. 13.— 0.80 to 2.43 μm spectra of our sources.

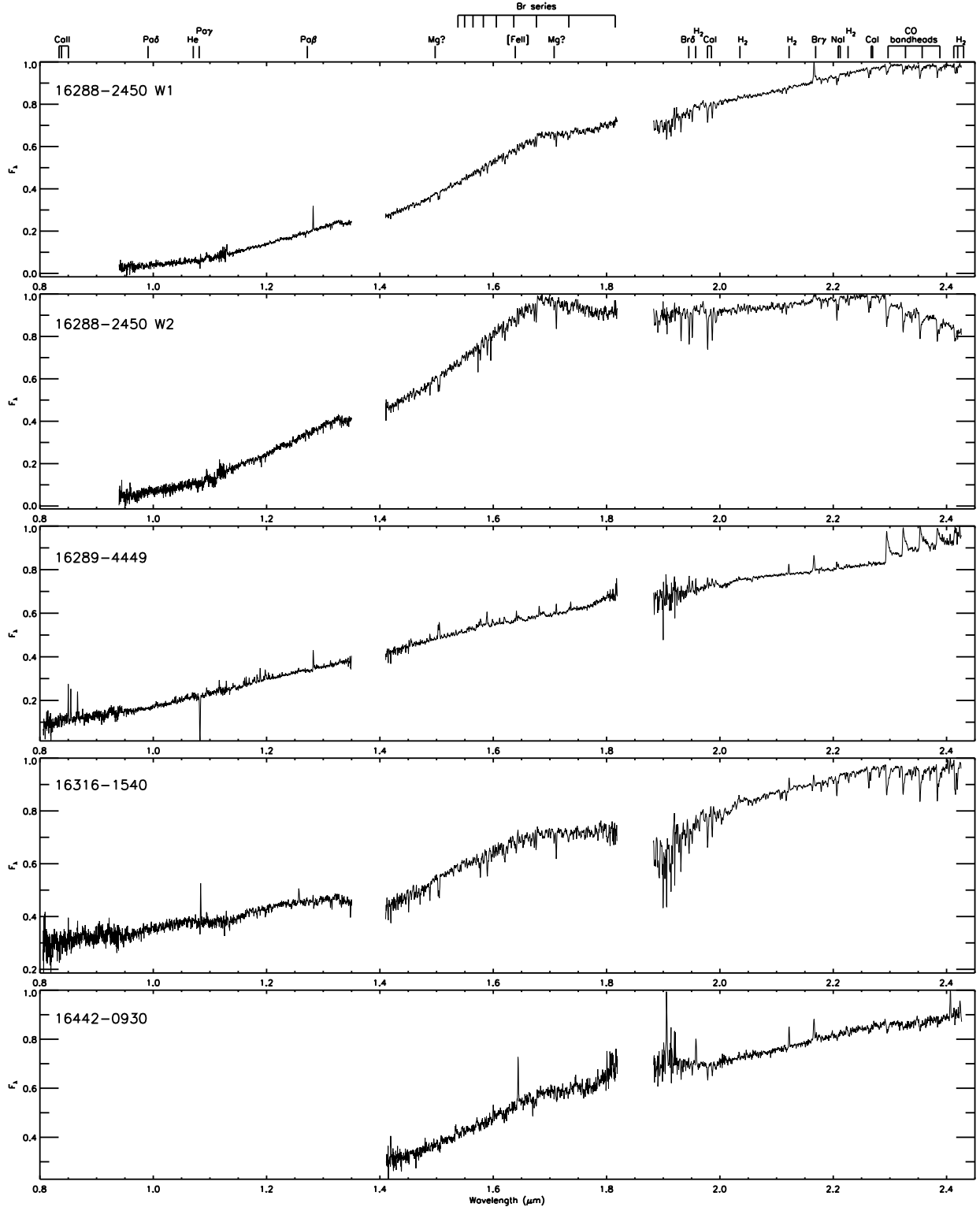


Fig. 13.— 0.80 to 2.43 μm spectra of our sources.

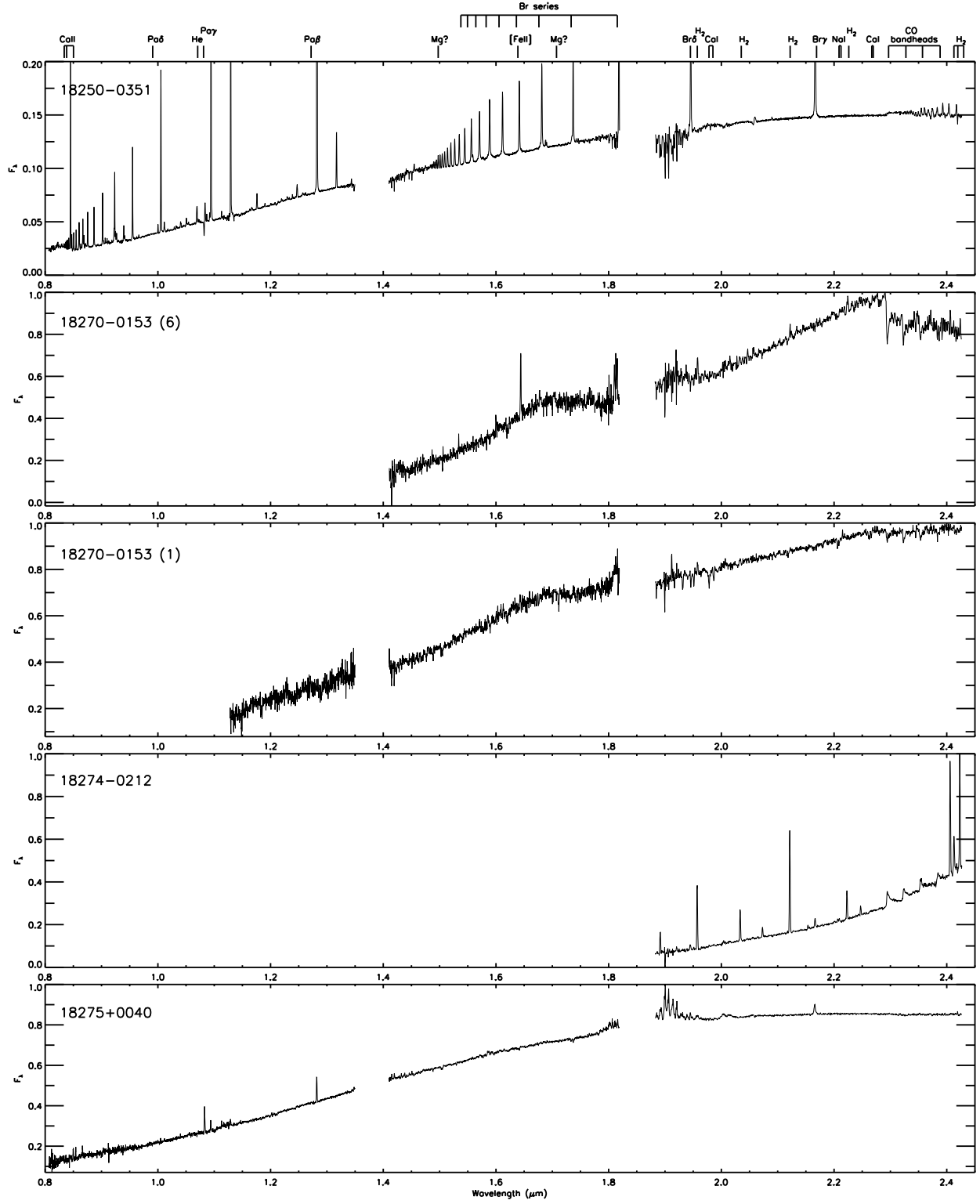


Fig. 13.— 0.80 to 2.43 μm spectra of our sources.

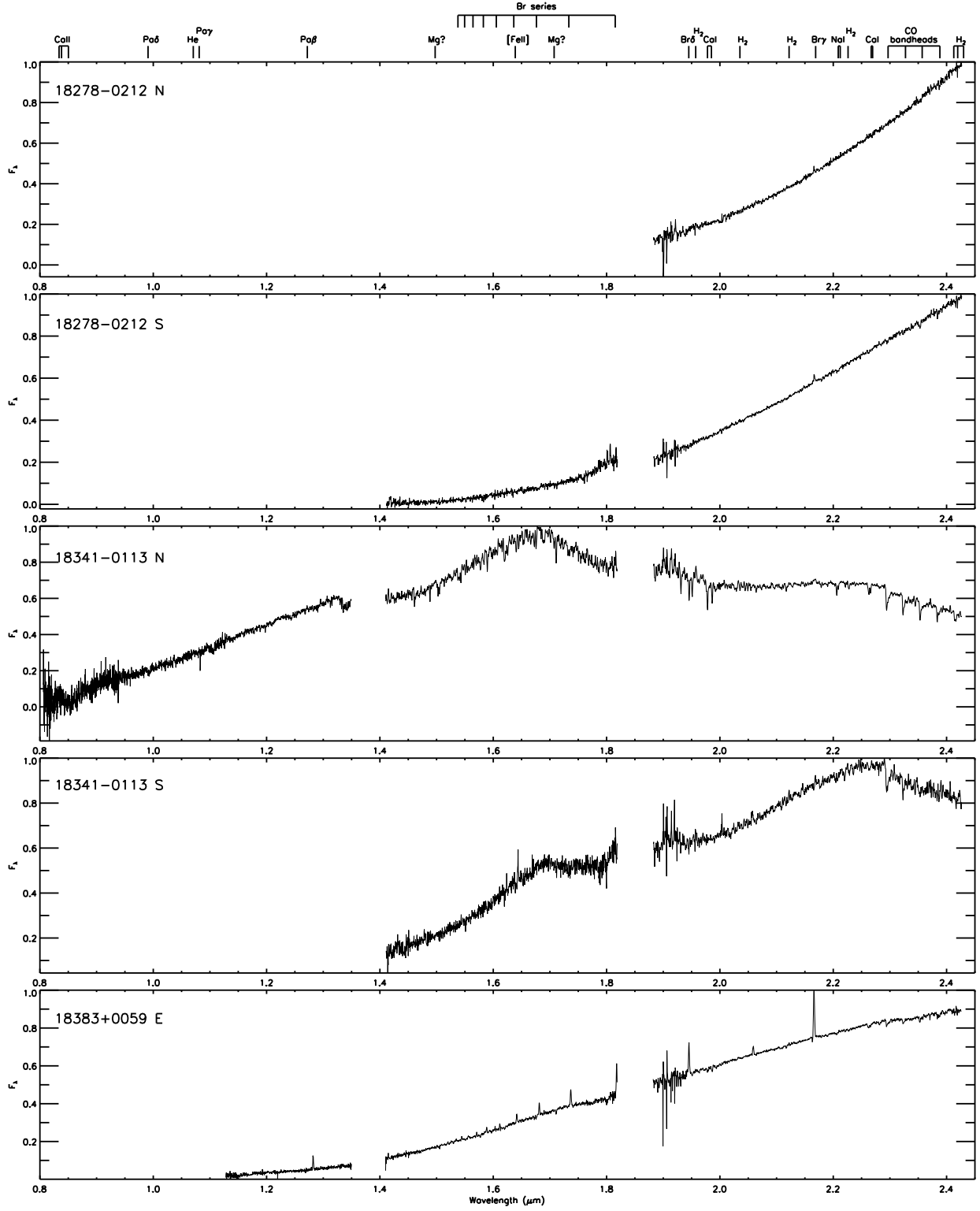


Fig. 13.— 0.80 to 2.43 μm spectra of our sources.

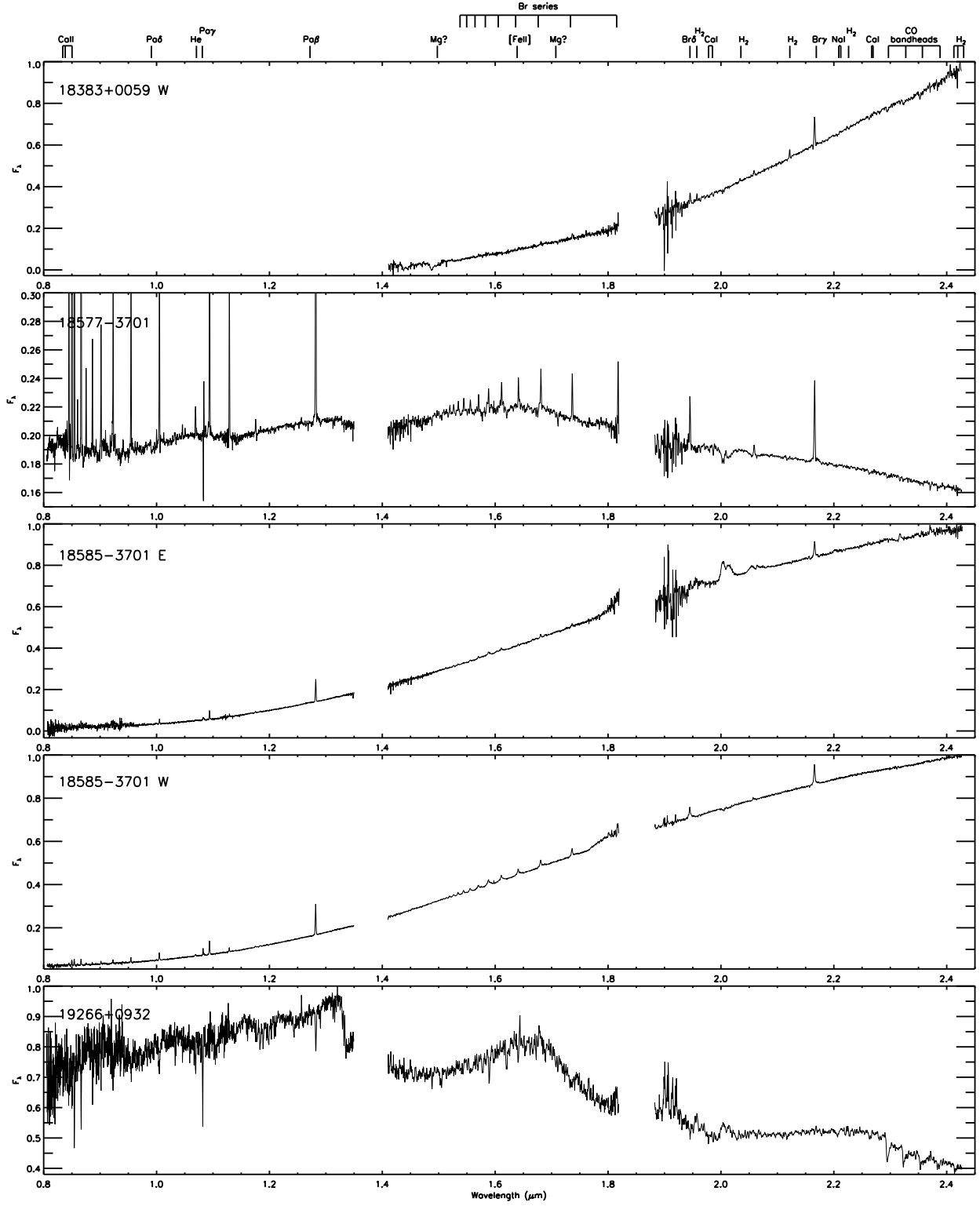


Fig. 13.— 0.80 to 2.43 μm spectra of our sources.

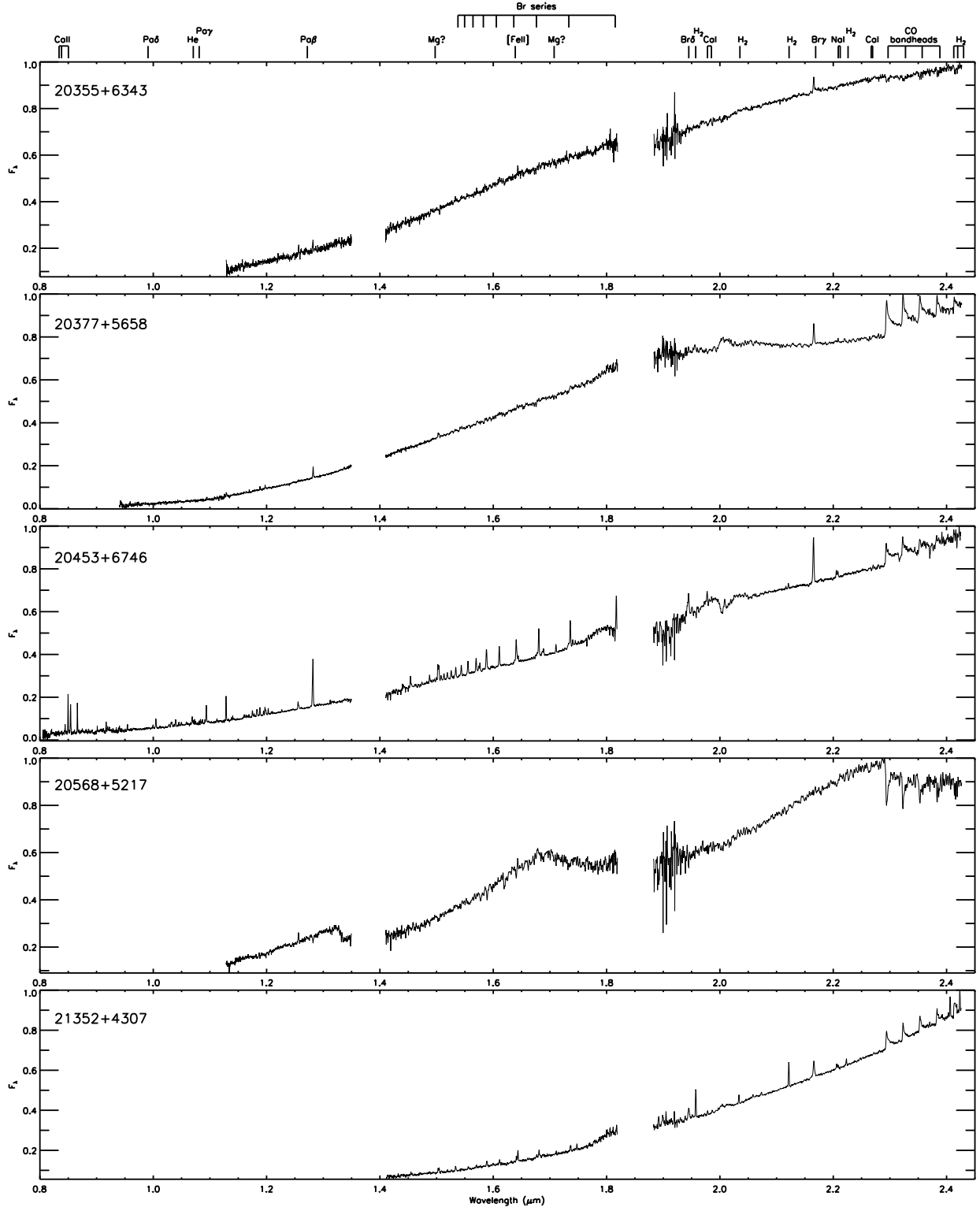


Fig. 13.— 0.8 to 2.45 μm spectra of our sources.

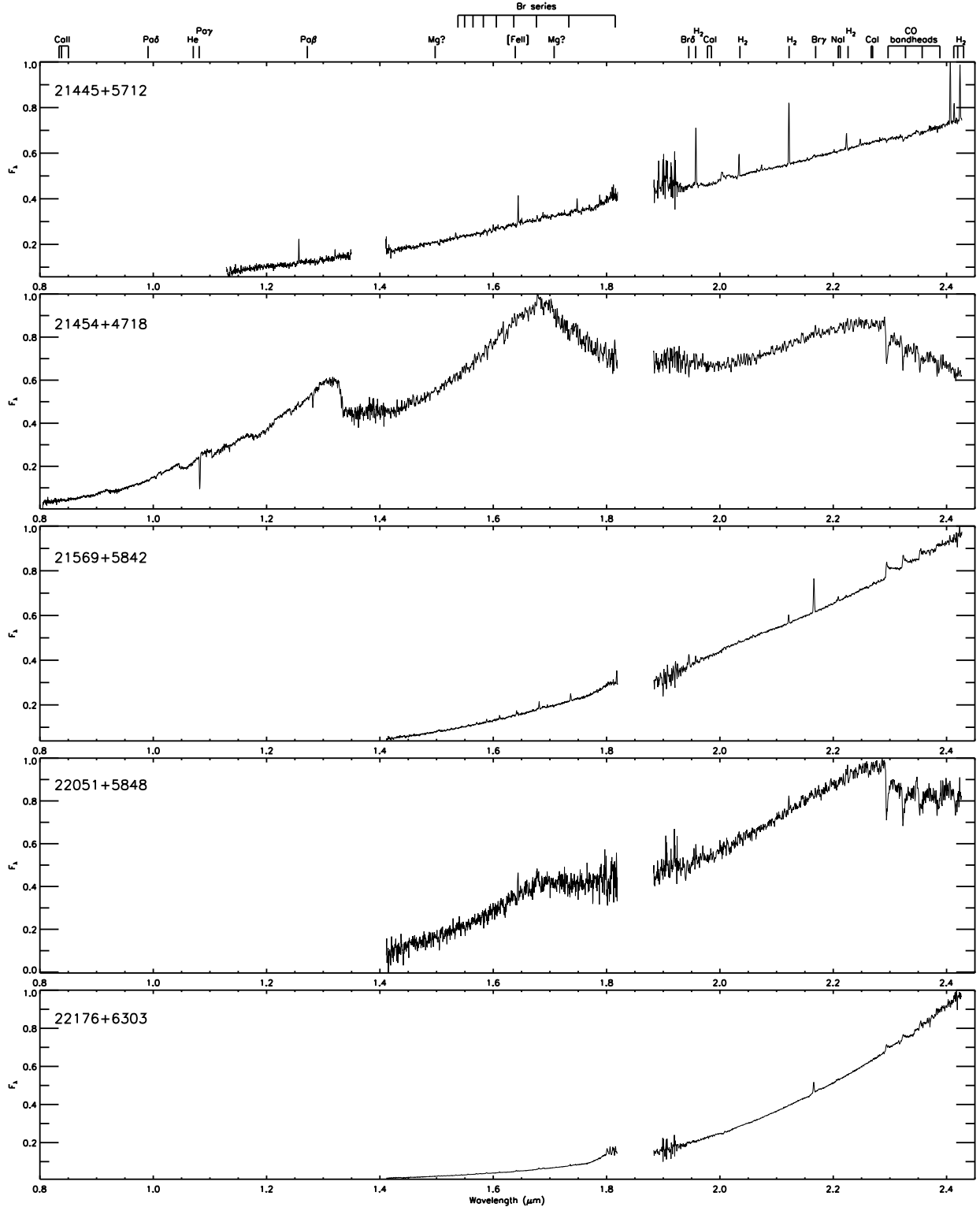


Fig. 13.— 0.8 to 2.45 μm spectra of our sources.

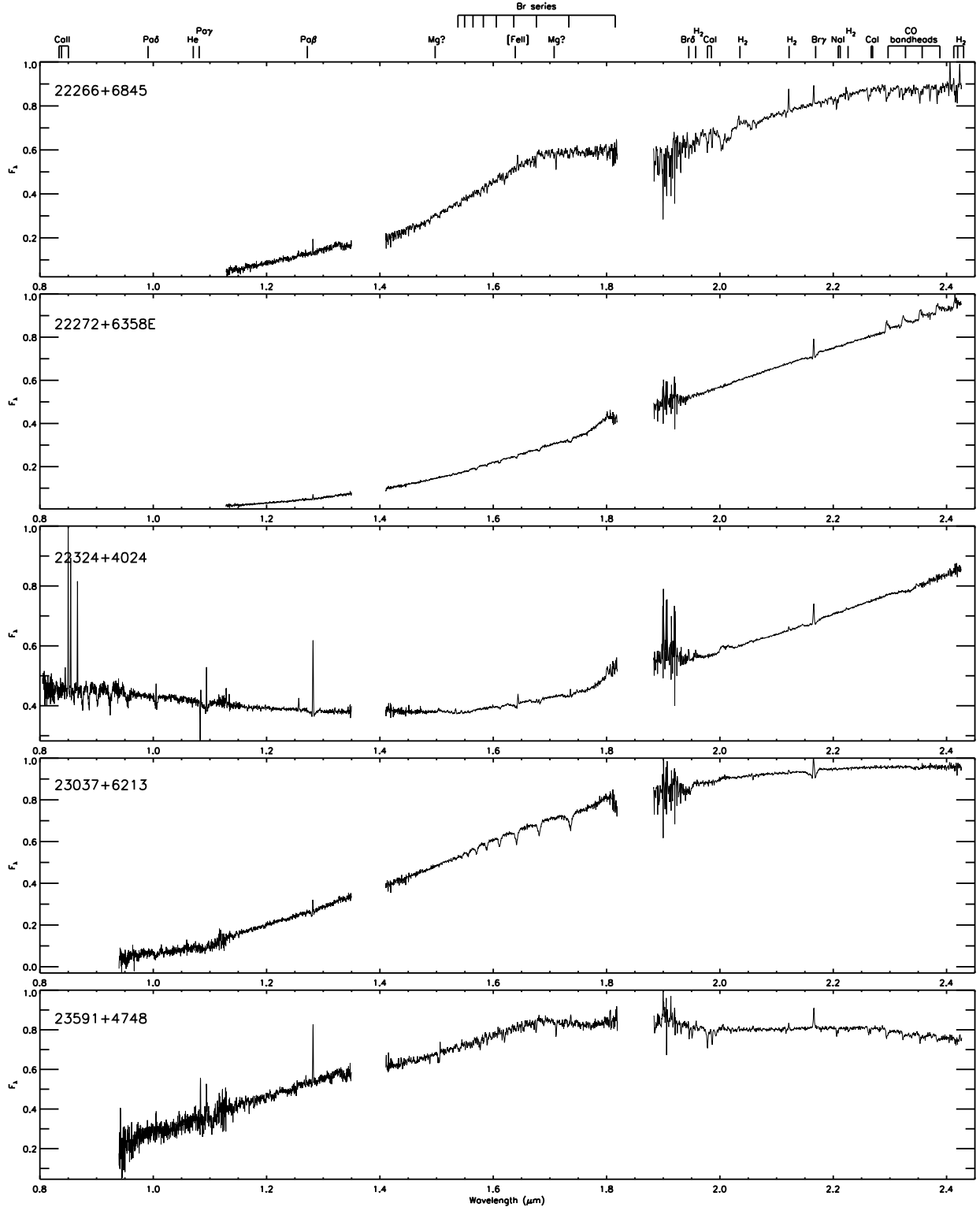


Fig. 13.— 0.8 to 2.45 μm spectra of our sources.

Table 1. Source Characteristics

IRAS	α (J2000) ^a	δ (J2000) ^a	K_s ^b	α^c	L_{bol} (L_\odot)	UT Date	S/N ^d	Time (s) ^e	Flag ^f
03220+3035(N)	03 25 09.43	+30 46 21.6	10.83	0.02	2.0	16 Nov 2006	375	2880	
03220+3035(S)	03 25 09.43	+30 46 21.6	10.57	0.02	...	16 Nov 2006	370	2400	4
F03258+3105	03 28 59.31	+31 15 48.5	10.88	0.59	32.3	11 Oct 2007	270	1440	5
03260+3111(E)	03 29 10.38	+31 21 59.2	7.67	0.58	138.4	10 Oct 2007	720	480	2,3
03260+3111(W)	03 29 07.74	+31 21 57.5	10.12	10 Oct 2007	560	1440	1,5
03301+3111	03 33 12.84	+31 21 24.1	10.58	0.31	4.0	17 Nov 2006	490	1440	4,5
03445+3242	03 47 41.60	+32 51 43.8	11.49	0.16	3.8	15 Nov 2006	430	2880	2,5
03507+3801	03 54 06.19	+38 10 42.5	9.91	0.22	2.5	15 Nov 2006	545	1920	2,4
04016+2610	04 04 43.05	+26 18 56.2	10.39	0.31	3.0	17 Nov 2006	240	2880	1
04073+3800	04 10 41.09	+38 07 54.0	9.05	0.07	22.6	01 Nov 2006	272	1920	2
04108+2803(E)	04 13 54.72	+28 11 32.9	11.06 ¹	-0.15	0.7	02 Mar 2007	90	1920	
04108+2803(W)	04 13 53.39	+28 11 23.4	10.37 ¹	02 Mar 2007	390	1920	4
04113+2758(N)	04 14 26.27	+28 06 03.3	8.20	-0.13	1.1	01 Nov 2006	731	960	
04113+2758(S)	04 14 26.40	+28 05 59.7	8.27	-0.13	1.1	01 Nov 2006	706	960	4
04169+2702	04 19 58.45	+27 09 57.1	11.26	0.53	0.9	11 Oct 2007	305	2880	2
04181+2655(N)	04 21 07.95	+27 02 20.4	10.54 ¹	1.96	...	11 Oct 2007	342	480	4
04181+2655(M)	04 21 10.39	+27 01 37.3	11.08 ¹	13 Oct 2007	288	1920	
04181+2655(S)	04 21 11.47	+27 01 09.4	10.34 ¹	11 Oct 2007	318	1920	
04189+2650(E)	04 22 02.18	+26 57 30.5	8.28	...	140.	14 Oct 2007	580	480	6
04189+2650(W)	04 22 00.70	+26 57 32.5	12.03	-0.04	...	14 Oct 2007	210	3840	2
04223+3700	04 25 39.80	+37 07 08.2	9.93	0.47	2.7	31 Oct 2006	321	1920	2,3
04239+2436	04 26 56.30	+24 43 35.3	10.22	0.09	1.1	31 Oct 2006	380	1920	2,3
04240+2559	04 27 04.70	+26 06 16.3	6.78	-0.26	3.5	03 Mar 2007	723	480	4,6
04248+2612	04 27 57.30	+26 19 18.4	10.62	0.52	0.3	10 Oct 2007	230	2400	1,4
04287+1801	04 31 34.08	+18 08 04.9	9.25 ¹	0.76	20.2	15 Nov 2006	563	2400	1,3
04292+2422(E)	04 32 15.41	+24 28 59.7	7.63	0.01	0.6	01 Nov 2006	934	1200	
04292+2422(W)	04 32 13.27	+24 29 10.8	8.05	01 Nov 2006	942	960	
04295+2251	04 32 32.05	+22 57 26.7	10.54	0.13	0.3	03 Mar 2007	225	2880	
04315+3617	04 34 53.22	+36 23 29.2	9.20	-0.05	1.7	17 Nov 2006	470	960	
04325+2402	04 35 35.39	+24 08 19.4	11.29	1.71	0.7	13 Oct 2007	160	2880	1
04365+2535	04 39 35.19	+25 41 44.7	10.60	0.68	1.9	16 Nov 2006	345	2880	2
04369+2539	04 39 55.75	+25 45 02.0	6.28	-0.49	1.3	01 Nov 2006	480	1200	2
04381+2540	04 41 12.68	+25 46 35.4	11.81	0.64	0.6	16 Nov 2007	165	3600	2
04530+5126	04 56 57.02	+51 30 50.9	7.80	0.05	...	02 Mar 2007	583	720	4
04591-0856	05 01 29.64	-08 52 16.9	10.40	0.62	0.9	02 Mar 2007	260	1920	2
05155+0707	05 18 17.30	+07 10 59.9	11.39	1.55	11.8	01 Nov 2006	127	2880	1
05256+3049	05 28 49.86	+30 51 29.3	10.17	0.16	6417.3	15 Nov 2006	315	4320	
05289-0430(E)	05 31 27.09	-04 27 59.4	9.61	0.38	7.1	16 Nov 2006	320	960	3
05302-0537	05 32 41.65	-05 35 46.1	10.39	0.38	5.4	17 Nov 2006	115	960	2,3
05311-0631	05 33 32.52	-06 29 44.2	10.14	0.23	7.3	31 Oct 2006	365	1920	2
05320-0300	05 34 31.09	-02 58 02.3	10.33	2.12	5.4	13 Oct 2007	280	960	
05327-0457(W)	05 35 13.10	-04 55 52.5	9.30	1.76	920.2	01 Nov 2006	447	960	2
05357-0650	05 38 09.31	-06 49 16.6	7.93 ¹	0.01	10.8	01 Nov 2006	750	480	
05375-0040(1)	05 40 06.79	-00 38 38.1	8.51 ¹	0.62	7.1	10 Oct 2007	380	480	
05375-0040(2)	05 40 06.37	-00 38 37.0	10.28 ¹	14 Oct 2007	263	960	
05375-0040(3)	05 40 05.79	-00 38 43.0	9.46 ¹	14 Oct 2007	402	960	4

Table 1—Continued

IRAS	α (J2000) ^a	δ (J2000) ^a	K_s ^b	α^c	L_{bol} (L_\odot)	UT Date	S/N ^d	Time (s) ^e	Flag ^f
05378–0750(E)	05 40 17.81	–07 48 25.8	9.57	...	8.2	15 Oct 2007	190	2640	
05379–0758(1)	05 40 20.55	–07 56 39.9	9.35 ¹	...	6.4	17 Nov 2006	90	2880	
05379–0758(2)	05 40 20.31	–07 56 24.9	10.86 ¹	17 Nov 2006	315	1920	4
05379–0758(3)	05 40 20.91	–07 56 24.6	12.37 ¹	0.19	...	17 Nov 2006	433	960	
05384–0808(1)	05 40 50.59	–08 05 48.7	11.48	1.03	10.8	13 Oct 2007	202	1920	3
05384–0808(3)	05 40 49.92	–08 06 08.4	11.15	13 Oct 2007	200	1680	2
05391–0841(N)	05 41 30.05	–08 40 09.2	12.13	0.77	3.6	14 Oct 2007	128	1920	
05391–0841(S)	05 41 30.34	–08 40 27.7	11.63	14 Oct 2007	182	2880	
05403–0818	05 42 47.07	–08 17 06.9	11.29	0.40	9.9	11 Oct 2007	158	1920	2
05404–0948	05 42 47.67	–09 47 22.5	9.23	0.76	49.8	14 Oct 2007	304	360	2,3
05405–0117	05 43 03.06	–01 16 29.2	10.25	0.71	4.4	01 Nov 2006	352	1920	2
05427–0116	05 45 17.31	–01 15 27.6	10.92	0.63	2.5	03 Mar 2007	229	2160	3
05450+0019	05 47 36.55	+00 20 06.3	8.78 ¹	1.26	27.6	31 Oct 2006	187	360	1
05513–1024	05 53 42.55	–10 24 00.7	5.96 ¹	0.18	...	01 Nov 2006	1177	1920	2
05555–1405(N)	05 57 49.46	–14 05 27.8	10.62	0.62	4.8	13 Oct 2007	235	960	3
05555–1405(S)	05 57 49.18	–14 06 08.0	10.86	13 Oct 2007	113	1440	
05598–0906(1)	06 02 16.20	–09 06 29.0	10.06	0.43	14.3	15 Nov 2006	373	1920	2,3
06047–1117	06 07 08.50	–11 17 51.0	10.32 ¹	0.64	4.9	01 Nov 2006	325	1920	2
06297+1021(E)	06 32 30.83	+10 18 39.6	9.30	0.32	46.8	16 Nov 2006	346	480	
06297+1021(W)	06 32 26.12	+10 19 18.4	8.14	16 Nov 2006	551	480	
06382+1017	06 41 02.64	+10 15 02.1	12.83	1.00	84.4	15 Oct 2007	16	1080	1,3
06393+0913	06 42 08.13	+09 10 30.0	10.45	1.42	28.9	15 Oct 2007	347	1800	
07018–1005(1)	07 04 13.93	–10 10 13.6	10.80	0.35	30.3	17 Nov 2007	208	1440	
07025–1204(2)	07 04 51.62	–12 09 29.9	11.60	1.29	49.5	17 Nov 2007	138	1920	3
07180–2356	07 20 08.36	–24 02 23.0	11.86	0.81	186.	16 Nov 2007	147	3240	2
16235–2416	16 26 34.17	–24 23 28.3	6.26	1.34	159.7	14 Jul 2007	872	480	6
16240–2430(E)	16 27 09.43	–24 37 18.8	7.16	0.24	25.6	13 Jul 2007	734	480	5
16240–2430(W)	16 27 02.34	–24 37 27.2	7.82	13 Jul 2007	480	480	5
16288–2450(E)	16 32 01.00	–24 56 42.0	10.13	0.70	5.5	14 Jul 2007	196	1920	1,3
16288–2450(W1)	16 31 52.98	–24 56 24.6	7.85	13 Jul 2007	405	480	2,4,5?
16288–2450(W2)	16 31 52.98	–24 56 24.6	8.69	13 Jul 2007	334	480	2,4,5?
16289–4449	16 32 32.19	–44 55 30.7	7.21	–0.04	5.9	13 Jul 2007	369	480	
16316–1540	16 34 29.29	–15 47 01.9	8.28	0.84	11.4	14 Jul 2007	384	480	2
16442–0930	16 46 58.27	–09 35 19.7	10.92 ¹	0.22	0.7	13 Jul 2007	156	1920	2
18250–0351	18 27 39.53	–03 49 52.0	...	0.20	219.7	14 Jul 2007	730	40	
18270–0153(6)	18 29 38.92	–01 51 06.3	11.89	13 Jul 2007	117	960	1
18270–0153(1)	18 29 36.69	–01 50 59.1	10.14	0.49	...	13 Jul 2007	164	1920	2,4
18274–0212	18 30 01.36	–02 10 25.6	11.66	0.12	...	13 Jul 2007	113	1920	2
18275+0040	18 30 06.17	+00 42 33.6	7.72	–0.19	3.4	14 Jul 2007	666	480	
18278–0212(N)	18 30 27.13	–02 10 56.4	11.81	14 Jul 2007	91	2880	
18278–0212(S)	18 30 27.28	–02 11 00.2	11.24	1.62	...	14 Jul 2007	166	1920	
18341–0113(N)	18 36 46.33	–01 10 29.5	9.80	0.91	...	14 Jul 2007	307	960	2,4
18341–0113(S)	18 36 46.49	–01 10 41.6	10.86	13 Jul 2007	124	1920	1
18383+0059(E)	18 40 51.87	+01 02 12.9	9.80	0.50	...	16 Aug 2006	305	960	2
18383+0059(W)	18 40 51.87	+01 02 12.9	10.90	0.50	...	16 Aug 2006	233	1440	2
18577–3701	19 01 08.61	–36 57 20.1	6.11 ¹	–0.18	1.5	14 Jul 2007	675	240	6

Table 1—Continued

IRAS	α (J2000) ^a	δ (J2000) ^a	K_s ^b	α^c	L_{bol} (L_\odot)	UT Date	S/N ^d	Time (s) ^e	Flag ^f
18585–3701(E)	19 01 58.78	–36 57 49.9	6.60 ¹	0.12	44.3	12 Jul 2007	330	420	
18585–3701(W)	19 01 53.68	–36 57 08.2	2.86 ¹	...	44.3	14 Jul 2007	638	80	
19266+0932	19 29 00.86	+09 38 42.9	9.68	0.37	3.4	14 Jul 2007	242	960	1
20355+6343	20 36 22.86	+63 53 40.4	10.40	0.59	2.5	13 Jul 2007	275	960	
20377+5658	20 38 57.48	+57 09 37.6	9.48	0.32	4.8	13 Jul 2007	508	960	2
20453+6746	20 45 53.94	+67 57 38.7	6.47	–0.32	63.7	12 Jul 2007	500	480	2
20568+5217	20 58 21.09	+52 29 27.7	7.90	0.62	45.6	12 Jul 2007	524	960	2
21352+4307	21 37 11.39	+43 20 38.4	11.75	0.17	11.7	14 Jul 2007	294	2400	2
21445+5712	21 46 07.12	+57 26 31.8	10.25	0.54	18.5	13 Jul 2007	264	1440	1
21454+4718	21 47 20.66	+47 32 03.6	7.03	0.70	106.7	13 Jul 2007	555	240	2
21569+5842	21 58 35.90	+58 57 22.8	10.25	0.08	1.0	13 Jul 2007	477	2160	2
22051+5848	22 06 50.37	+59 02 45.9	11.23	1.15	73.	13 Jul 2007	88	1920	1
22176+6303	22 19 20.39	+63 19 38.5	6.13 ¹	0.87	21313.	12 Jul 2007	561	480	1
22266+6845	22 28 02.99	+69 01 16.7	10.49	0.53	1.8	13 Jul 2007	295	1920	2,3
22272+6358(E)	22 28 57.60	+64 13 37.5	8.18	1.76	815.5	14 Jul 2007	473	480	2
F22324+4024	22 34 41.01	+40 40 04.5	9.46	0.08	111.6	12 Jul 2007	544	1920	
23037+6213	23 05 49.76	+62 30 01.2	9.04 ¹	1.23	330.2	14 Jul 2007	332	720	2
F23591+4748	00 01 43.25	+48 05 19.0	10.42	0.60	...	14 Jul 2007	228	1920	

^a2MASS coordinate for candidate YSO.

^bK-band magnitudes from Table 4 from Connelley et al. (2008), and are in the MKO photometric system unless otherwise noted. Magnitudes noted with ¹ are from 2MASS and are in the 2MASS photometric system.

^c α is the spectral index of the source (Lada 1991), and is calculated from the IRAS fluxes of the source.

^dPeak continuum K-band signal to noise ratio.

^eTotal integration time on target.

^fFlags: 1) No point source is seen at K-band. Flux likely dominated by scattered light, which affects near-IR colors; 2) Object associated with a reflection nebula, which may affect near-IR colors; 3) Light from both components of a known binary are in the spectrum; 4) Spectrum has triangular shaped H-band continuum; 5) Identified as a YSO in Table 12 of Evans et al. 2009; 6) Well known as a T Tauri star

Table 2. Spectral Type and Extinction Estimates

IRAS ^a	Type ^b	Colors ^c	Continuum ^d	Extinction (A_v)		H_2 Q(3)/S(1)	$T_{veiling}^d$ (K)	r_k^f
				[Fe II] ^e	Paschen β /Brackett γ			
03220+3035(N)		8.4	$0.6^{+9.0}_{-0.6}$	11.7 ± 0.4	18.4 ± 0.1		1220^{+330}_{-140}	high
03220+3035(S)	M2 $K3_{M4}$	8.4	$9.4^{+4.0}_{-3.0}$...	$0.0^{+0.88}_{-0.0}$
F03258+3105	M2 $M0_{M3}$	37.2	$34.6^{+4.0}_{-4.8}$...	$0.12^{+0.62}_{-0.0}$
03260+3111(E)	F5 $F4_{G0}$	6.5	$12.6^{+1.6}_{-2.3}$...	$0.14^{+0.50}_{-0.14}$
03260+3111(W)			$28.8^{+40.0}_{-28.8}$			$47.82^{+7.57}_{-8.88}$	680^{+700}_{-180}	high
03301+3111	M2 $K0_{M3}$	13.2	$14.7^{+6.2}_{-3.5}$	22.1 ± 5.3	15.6 ± 0.4		...	$0.48^{+0.84}_{-0.3}$
03445+3242		> 18.9	$28.8^{+20.0}_{-22.0}$				1120^{+880}_{-420}	high
03507+3801	G7 $F5_{K0}$	10.8	$10.8^{+5.7}_{-1.3}$	$11.5 \pm 3.9^*$			1370^{+360}_{-570}	$0.6^{+2.16}_{-0.36}$
04016+2610		5.2	$28.8^{+3.2}_{-28.8}$			$30.71^{+3.91}_{-4.23}$	800^{+110}_{-200}	high
04073+3700	FU Ori	-8.4	$44.0^{+11.0}_{-14.0}$				770^{+730}_{-370}	high*
04108+2803(E)	K2 $K0_{M3}$	20.7	$32.4^{+9.6}_{-12.5}$			$8.16^{+3.05}_{-3.24}$...	$0.12^{+1.08}_{-0.0}$
04108+2803(W)	M2 $K0_{M4}$	15.5	$17.6^{+7.5}_{-7.5}$...	$0.24^{+1.20}_{-0.24}$
04113+2758(N)	M2 $M0_{M4}$	14.3	$20.6^{+8.4}_{-3.1}$		24.7 ± 0.4		1340^{+660}_{-640}	$0.6^{+1.94}_{-0.0}$
04113+2758(S)	M2 $M0_{M4}$	10.5	$14.7^{+3.3}_{-2.0}$...	$0.00^{+0.72}_{-0.00}$
04169+2702	M2 $K0_{M4}$	37.1	$39.2^{+13.3}_{-13.0}$...	$0.60^{+1.20}_{-0.24}$
04181+2655(N)	G7 $G0_{M4}$	6.5	$13.2^{+9.5}_{-2.0}$	18.0 ± 4.1	9.2 ± 0.8		1200^{+260}_{-300}	$0.12^{+3.84}_{-0.12}$
04181+2654(M)	M1 $K5_{M4}$	> 50.4	$51.4^{+7.5}_{-2.0}$				2000^{+0}_{-1100}	$0.24^{+0.00}_{-0.24}$
04181+2655(S)	G7 $G0_{M3}$	28.7	$43.8^{+5.2}_{-18.3}$			$24.69^{+2.66}_{-2.82}$...	$0.00^{+1.44}_{-0.00}$
04189+2650(E)	M2 $M1_{M4}$	5.4	$5.2^{+2.5}_{-1.2}$		5.2 ± 0.4		1550^{+220}_{-350}	$0.72^{+1.20}_{-0.00}$
04189+2650(W)		4.7	$6.0^{+6.0}_{-4.5}$	4.6 ± 1.4	11.6 ± 0.3		1000^{+180}_{-220}	$4.92^{+8.0}_{-2.8}$
04223+3700		> 44.7	$48.0^{+4.0}_{-31.0}$				1890^{+110}_{-1050}	high
04239+2436		20.8	$35.2^{+12.0}_{-34.0}$				1270^{+730}_{-770}	high
04240+2559	G3 $G1_{K2}$	0.4	$3.1^{+2.4}_{-2.8}$		8.5 ± 0.4	$-2.26^{+3.71}_{-4.00}$	1630^{+330}_{-500}	$0.00^{+1.68}_{-0.00}$
04248+2612	M3 $M0_{M4}$	8.7	$9.2^{+3.8}_{-4.7}$	9.7 ± 5.4	22.0 ± 1.1		...	$0.00^{+2.76}_{-0.00}$
04286+1801	FU Ori	6.8		19.3 ± 0.7			...	high*
04292+2422(E)	G7 $G0_{M3}$	11.5	$10.9^{+3.7}_{-1.8}$		14.4 ± 0.5		1610^{+390}_{-700}	$0.12^{+2.52}_{-0.90}$
04292+2422(W)	G7 $G0_{M3}$	31.8	$36.8^{+2.0}_{-3.3}$...	$0.00^{+1.74}_{-0.00}$
04295+2251	M2 $K0_{M4}$	22.0	$24.8^{+11.5}_{-3.3}$				1020^{+260}_{-370}	$0.54^{+1.08}_{-0.30}$
04315+3617		7.3	$4.8^{+2.2}_{-2.0}$				1470^{+170}_{-230}	$3.6^{+2.6}_{-2.1}$
04325+2402		52.2	$28.8^{+5.2}_{-28.8}$				2000^{+0}_{-1150}	high
04365+2535		43.8	$30.0^{+9.0}_{-30.0}$				740^{+240}_{-170}	high
04369+4539		17.8	$8.0^{+9.0}_{-2.2}$		25.9 ± 0.3		1220^{+260}_{-120}	high
04381+2540	K5 $K0_{M2}$	27.0	$49.2^{+13.0}_{-12.0}$...	$0.24^{+0.66}_{-0.24}$
04530+5126	M2 $M1_{M3}$	3.4	$4.4^{+1.3}_{-2.1}$		7.5 ± 0.5		...	$0.36^{+1.32}_{-0.00}$
04591-0856	K7 $K4_{M3}$	4.4	$18.5^{+9.2}_{-3.0}$...	$0.18^{+0.06}_{-0.18}$
05155+0707		> 57.6	$28.0^{+13.0}_{-25.0}$				1270^{+730}_{-540}	high
05256+3049		> 11.6	$24.0^{+18.0}_{-24.0}$			29.89 ± 2.81	1500^{+500}_{-780}	high
05289-0430(E)		8.5	$4.8^{+5.0}_{-4.8}$	6.0 ± 1.7	16.8 ± 0.7		920^{+70}_{-80}	$8.0^{+5.0}_{-3.5}$
05302-0537			$24^{+56.0}_{-24.0}$			33.09 ± 1.90	630^{+1370}_{-180}	high
05311-0631	M4 $M2_{M4}$	5.7	$42.8^{+5.7}_{-11.3}$				1890^{+110}_{-840}	$1.32^{+1.32}_{-0.48}$
05320-0300	M2 $K0_{M4}$	12.4	$14.1^{+6.4}_{-3.1}$				1650^{+350}_{-1000}	$0.18^{+1.20}_{-0.00}$
05327-0457(W)	A5 $A0_{F7}$	14.6	$26.6^{+5.0}_{-5.2}$...	$0.48^{+3.36}_{-0.24}$
05357-0650	A0 $A5_{A5}$	-2.1	$6.0^{+1.6}_{-0.6}$				1620^{+140}_{-190}	$5.32^{+0.00}_{-3.78}$
05375-0040(1)	G7 $G3_{K5}$	5.5	$6.4^{+2.7}_{-0.5}$		5.6 ± 0.3		1590^{+340}_{-440}	$0.00^{+1.96}_{-0.00}$
05375-0040(2)	M2 $M1_{M4}$	7.2	$6.2^{+4.3}_{-1.2}$		5.7 ± 0.4		...	$0.42^{+0.70}_{-0.28}$

Table 2—Continued

IRAS ^a	Type ^b	Colors ^c	Continuum ^d	Extinction (A_v)		H_2 Q(3)/S(1)	$T_{veiling}^d$ (K)	r_k^f
				[Fe II] ^e	Paschen β /Brackett γ			
05375–0040(3)	G7 $_{K0}^{F5}$	7.8	9.0 $^{+3.0}_{-0.8}$	$11.4 \pm 3.3^*$			1410 $^{+460}_{-500}$	0.14 $^{+1.26}_{-0.14}$
05378–0750(E)		25.4	28.0 $^{+16.}_{-10.}$				1240 $^{+760}_{-400}$	high
05379–0758(1)		15.2	12.2 $^{+5.0}_{-3.8}$				1410 $^{+270}_{-240}$	5.0 $^{+2.0}_{-5.0}$
05379–0758(2)	K2 $_{M4}^{K0}$	12.7	15.6 $^{+9.6}_{-2.8}$...	0.12 $^{+1.02}_{-0.12}$
05379–0758(3)		53.9	32.0 $^{+7.0}_{-32.0}$			
F05384–0807(1)	M2 $_{M4}^{K0}$	> 15.0	50.4 $^{+6.8}_{-8.4}$	13.0 ± 0.6	22.8 ± 1.4		...	0.30 $^{+1.02}_{-0.30}$
F05384–0807(3)	M2 $_{M4}^{K0}$	> 2.0	36.8 $^{+7.4}_{-13.3}$...	0.54 $^{+1.50}_{-0.06}$
F05391–0841(N)		> 4.5	53.2 $^{+9.}_{-46.}$				1060 $^{+940}_{-400}$	high
F05391–0841(S)		> 2.0	42.0 $^{+10.}_{-24.}$				1120 $^{+880}_{-380}$	high
05403–0818		13.1	3.2 $^{+16.0}_{-3.2}$				1040 $^{+560}_{-140}$	high
05404–0948	F0 $_{F3}^{A5}$	2.5	9.1 $^{+1.2}_{-1.0}$	11.9 ± 3.8			...	0.24 $^{+0.84}_{-0.12}$
05405–0117	M2 $_{M4}^{G3}$	19.3	25.6 $^{+8.9}_{-6.1}$...	1.56 $^{+1.08}_{-1.56}$
05427–0116	M2 $_{M3}^{K0}$	18.5	20.7 $^{+5.6}_{-5.7}$...	0.36 $^{+1.08}_{-0.24}$
05450+0019	FU Ori	13.5	31.5 $^{+4.2}_{-11.0}$...	high*
05513–1024	F0 $_{F3}^{F0}$	11.2	3.6 $^{+1.8}_{-2.4}$				1420 $^{+110}_{-120}$	8.8 $^{+4.8}_{-3.2}$
05555–1405(N)		5.3	4.0 $^{+5.1}_{-4.0}$	-1.1 ± 3.5	7.6 ± 0.8		1410 $^{+290}_{-360}$	4.9 $^{+4.4}_{-4.9}$
05555–1405(S)	M2 $_{M3}^{G3}$	3.5	7.8 $^{+3.3}_{-1.0}$				1100 $^{+400}_{-290}$	0.54 $^{+1.14}_{-0.48}$
05598–0906(1)		16.0	14.4 $^{+18.1}_{-12.}$				1530 $^{+470}_{-600}$	high
06047–1117		3.6	33.6 $^{+10.4}_{-33.6}$				1780 $^{+220}_{-1030}$	high
06297+1021(E)		15.9	7.2 $^{+13.0}_{-4.0}$				1130 $^{+470}_{-100}$	high
06297+1021(W)	FU Ori	5.0	8.4 $^{+1.8}_{-3.2}$	$2.6 \pm 3.4^*$	16.4 ± 1.3	24.69 ± 1.35	940 $^{+510}_{-240}$	high*
06382+1017		–5.4	5.0 $^{+73.0}_{-5.0}$				570 $^{+1430}_{-100}$	high
06393+0913	G7 $_{M0}^{G0}$	30.6	30.2 $^{+2.9}_{-9.2}$...	0.00 $^{+2.04}_{-0.00}$
07018–1005(1)		11.7	9.6 $^{+19.4}_{-9.6}$				1240 $^{+760}_{-440}$	high
07025–1204(2)			25.6 $^{+10.}_{-25.6}$				1210 $^{+790}_{-460}$	high
07180–2356		> 11.6	4.8 $^{+41.}_{-4.8}$	8.8 ± 2.0			790 $^{+1210}_{-120}$	high
16235–2416	F0 $_{F4}^{A3}$	8.8	16.2 $^{+2.2}_{-2.5}$...	0.36 $^{+0.06}_{-0.06}$
16240–2430(E)		49.3	57.8 $^{+30.}_{-18.}$				1100 $^{+900}_{-300}$	high
16240–2430(W)	A0 $_{F3}^{A0}$	29.5	45.4 $^{+6.0}_{-13.4}$...	0.8 $^{+0.4}_{-0.8}$
16288–2450(E)		> 18.9	30.8 $^{+26.}_{-30.8}$				840 $^{+1160}_{-300}$	high
16288–2450(W1)	M2 $_{M4}^{K0}$	13.5	17.0 $^{+10.5}_{-3.0}$	$-1.0 \pm 6.7^*$	22.3 ± 0.6		...	1.20 $^{+1.08}_{-1.08}$
16288–2450(W2)	M2 $_{M4}^{K0}$	13.5	21.4 $^{+1.6}_{-7.4}$...	0.0 $^{+0.84}_{-0.0}$
16289–4449		3.9	5.6 $^{+4.1}_{-3.7}$				1200 $^{+170}_{-220}$	6.3 $^{+4.0}_{-4.3}$
16316–1540	K0 $_{M3}^{G7}$	2.7	16.0 $^{+9.0}_{-4.0}$...	0.00 $^{+1.32}_{-0.00}$
16442–0930		8.6	18.0 $^{+7.5}_{-8.2}$				1290 $^{+710}_{-590}$	1.4 $^{+1.4}_{-1.2}$
18250–0351		7.3	7.2 $^{+3.3}_{-7.2}$	5.5 ± 0.03	14.9 ± 0.5	23.30 ± 0.93	1240 $^{+220}_{-400}$	3.2 $^{+6.6}_{-2.0}$
18270–0153(6)	FU Ori		29.4 $^{+1.5}_{-26.0}$...	high*
18270–0153(1)		12.6	14.0 $^{+5.0}_{-6.0}$				1270 $^{+730}_{-600}$	1.1 $^{+0.7}_{-0.8}$
18274–0212			14.4 $^{+50.0}_{-14.4}$				700 $^{+1300}_{-250}$	high
18275+0040		1.3	3.6 $^{+3.2}_{-3.6}$				1410 $^{+120}_{-140}$	11.2 $^{+25.}_{-5.}$
18278–0212(N)			57.6 $^{+7.5}_{-57.6}$				2000 $^{+0}_{-1500}$	high
18278–0212(S)			40.0 $^{+5.}_{-40.}$				1500 $^{+500}_{-900}$	high
18341–0113(N)	M2 $_{M4}^{K0}$	11.6	11.4 $^{+1.6}_{-4.4}$...	0.12 $^{+2.16}_{-0.00}$
18341–0113(S)	FU Ori	12.2	19.2 $^{+5.0}_{-9.2}$...	high*
18383+0059(E)		23.0	23.3 $^{+4.2}_{-11.8}$				1960 $^{+40}_{-760}$	high

Table 2—Continued

IRAS ^a	Type ^b	Colors ^c	Continuum ^d	Extinction (A_v)		H_2 Q(3)/S(1)	$T_{veiling}$ ^d (K)	r_k ^f
				[Fe II] ^e	Paschen β /Brackett γ			
18383+0059(W)		23.0	$41.0^{+3.5}_{-32.3}$				2000^{+0}_{-1300}	high
18577–3701		1.3	$0.00^{+2.1}_{-0.0}$		5.5 ± 0.1		1490^{+80}_{-140}	$4.8^{+0.5}_{-2.9}$
18585–3701(E)		1.06	$9.6^{+4.5}_{-3.9}$		17.1 ± 0.5		1280^{+170}_{-230}	high
18585–3701(W)		4.2	$8.4^{+2.1}_{-5.9}$		16.8 ± 0.2		1250^{+90}_{-180}	high
19266+0932	G3 ^{F5} _{K2}	–3.7	$0.0^{+4.8}_{-0.0}$	$7.0 \pm 3.8^*$...	$0.00^{+2.28}_{-0.00}$
20355+6343		12.1	$13.0^{+5.0}_{-10.3}$	9.6 ± 4.5	21.5 ± 1.3		1410^{+590}_{-260}	$3.9^{+30}_{-3.9}$
20377+5658		19.7	$15.0^{+4.6}_{-11.}$		25.8 ± 0.5		1940^{+60}_{-800}	high
20453+6746		19.3	$4.0^{+17.0}_{-4.0}$	$-1.1 \pm 1.9^*$	17.2 ± 0.1		1040^{+960}_{-140}	high
20568+5217	FU Ori	5.6	$14.8^{+4.7}_{-5.3}$	$1.2 \pm 4.1^*$...	high*
21352+4307			$4.2^{+15.}_{-4.2}$				770^{+800}_{-100}	high
21445+5712		6.8	$10.0^{+6.0}_{-7.0}$	11.0 ± 1.6		7.27 ± 0.95	1050^{+200}_{-170}	$5.1^{+2.6}_{-3.3}$
21454+4718	FU Ori	11.3	$11.1^{+1.5}_{-1.6}$...	high*
21569+5842		11.7	$24.0^{+10.}_{-18.}$				1290^{+780}_{-460}	high
22051+5848	FU Ori	4.7	$24.0^{+3.7}_{-7.}$...	high*
22176+6303		10.9	$16.8^{+13.}_{-12.8}$				690^{+160}_{-150}	high
22266+6845	K2 ^{G0} _{M4}	21.8	$23.4^{+1.2}_{-2.2}$	8.2 ± 3.9	23.7 ± 0.6		...	$0.12^{+1.56}_{-0.12}$
22272+6358(E)	F3 ^{A0} _{G3}	22.6	$38.0^{+8.0}_{-1.5}$		32.2 ± 0.6		...	$0.0^{+4.44}_{-0.0}$
22324+4024	F3 ^{A0} _{F4}	–5.6	$4.1^{+1.1}_{-2.1}$	$9.3 \pm 2.0^*$	8.5 ± 0.5		920^{+100}_{-100}	$8.4^{+2.2}_{-1.3}$
23037+6213	F3 ^{A0} _{F4}	13.2	$23.8^{+7.7}_{-1.6}$...	$0.60^{+4.44}_{-0.12}$
23591+4748	M2 ^{G7} _{M4}	8.7	$8.2^{+5.8}_{-2.7}$		11.6 ± 0.6		1500^{+500}_{-750}	$0.84^{+1.32}_{-0.84}$

^aA number in parenthesis after the IRAS designation specifies the source on the findercharts in Connelley et al. 2008a

^bBased on matching photospheric absorption lines. Given as best fit spectral class, then the range of well fit spectral classes as the uncertainty range in the superscript and subscript. “FU Ori” designates objects with a spectrum characteristic of FU Orionis-like objects and/or is a known FU Orionis-like object.

^cBased on dereddening the 2MASS colors to the T Tauri locus as defined by Meyer et al. 1997 AJ 114 1

^dBased on continuum fitting with the best fit spectral type as the input (when available, otherwise M2V was used). Maximum allowed veiling temperature is 2000 K, which often limits the upper error bar. A veiling temperature is presented only if spectral fitting reasonably constrains the veiling temperature.

^eBased on the ratio of the [Fe II] 1.257 μ m and 1.644 μ m lines. * designates targets where the 1.644 μ m line is on the edge of a comparatively strong absorption feature or is partially blended with the Brackett 12 emission line.

^fBased on either photospheric absorption lines or continuum fitting. “High” designated objects where we could not establish an upper limit on r_k because the veiling is too high. * designates FU Orionis-like spectra where the veiling is much higher than the result of the continuum fitting. The dearth of photospheric lines shows that the actual extinction is likely to be much higher.

Table 3. Common Circumstellar Lines

ID	λ (μm)	Emission	Absorption	Comment ^a
Ca II	0.850, 0.854, 0.866	20/33	0/33	...
He I	1.083	27/67	24/67	...
Fe II	1.644	44/107	0/67	...
H ₂	2.122	47/110	0/110	1
Br γ	2.166	83/110	8/110	2
CO	2.293, 2.322, 2.352, 2.383, 2.414	25/110	63/110	2

^a1) The $2.122\mu\text{m}$ H₂ line is the strongest of several H₂ lines observed in the K-band;
2) Emission is circumstellar, absorption often photospheric but can also be circumstellar

Table 4. Emission Line Equivalent Widths

IRAS	CaII (0.866 μ m)	He I (1.083 μ m) ^a	Pa β (1.282 μ m)	[Fe II] (1.644 μ m)	H ₂ (2.122 μ m)	Br γ (2.166 μ m)	CO (2.293 μ m)
03220+3035(N)	-37.57 \pm 10.57	-25.43 \pm 1.85	-37.39 \pm 1.57	-12.82 \pm 0.41		-17.70 \pm 0.19	-30.01 \pm 1.15
03220+3035(S)						-1.71 \pm 0.29	9.97 \pm 0.61
F03258+3105						2.25 \pm 0.40	7.11 \pm 0.48
03260+3111(E)		0.94 \pm 0.08				4.04 \pm 0.33	0.74 \pm 0.54
03260+3111(W)					-1.30 \pm 0.06	-2.04 \pm 0.11	-1.62 \pm 0.44
03301+3111			-5.25 \pm 0.29		-2.92 \pm 0.08	-2.31 \pm 0.08	5.80 \pm 0.43
03445+3242				-9.70 \pm 0.36	-2.22 \pm 0.07	-6.34 \pm 0.15	-16.25 \pm 0.73
03507+3801		1.24 \pm 0.30			-0.24 \pm 0.07	-0.64 \pm 0.57	1.07 \pm 0.45
04016+2610					-2.77 \pm 0.16	-2.30 \pm 0.08	
04073+3800					-0.64 \pm 0.14	0.42 \pm 0.18	26.73 \pm 1.40
04108+2803(E)					-6.57 \pm 0.26	-4.07 \pm 0.29	4.68 \pm 0.60
04108+2803(W)						-1.72 \pm 0.41	11.74 \pm 0.88
04113+2758(N)		1.19 \pm 0.33, -3.53 \pm 0.39	-7.85 \pm 0.30			-3.22 \pm 0.16	1.86 \pm 0.27
04113+2758(S)						-1.45 \pm 0.20	10.40 \pm 0.97
04169+2702				-2.89 \pm 0.63	-1.57 \pm 0.05	-1.50 \pm 0.09	1.19 \pm 0.25
04181+2655(N)		-4.08 \pm 0.78			-0.72 \pm 0.17	-0.89 \pm 0.06	2.51 \pm 0.63
04181+2655(M)					0.46 \pm 0.12		10.42 \pm 0.67
04181+2655(S)					-1.87 \pm 0.09	-8.41 \pm 0.14	4.18 \pm 0.35
04189+2650(E)	-2.15 \pm 0.33	1.53 \pm 0.12, -3.43 \pm 0.21			-1.31 \pm 0.16	-1.74 \pm 0.06	4.13 \pm 0.50
04189+2650(W)		-90.27 \pm 16.16	-25.23 \pm 2.05	-7.57 \pm 0.70	-5.15 \pm 0.09	-6.48 \pm 0.21	0.63 \pm 0.62
04223+3700						-2.36 \pm 0.09	-11.09 \pm 1.16
04239+2436				-9.64 \pm 0.65	-1.68 \pm 0.05	-13.66 \pm 0.24	-11.60 \pm 1.13
04240+2559	-32.62 \pm 0.89	-13.47 \pm 0.31	-14.43 \pm 0.33		-0.73 \pm 0.03	-7.78 \pm 0.07	1.20 \pm 0.22
04248+2612		-2.99 \pm 0.75	-1.32 \pm 0.21		-4.89 \pm 0.17	-2.75 \pm 0.25	8.59 \pm 0.30
04287+1801				-13.77 \pm 0.61	-1.60 \pm 0.24	-3.32 \pm 2.04	19.43 \pm 2.08
04292+2422(E)	-7.62 \pm 0.48	0.89 \pm 0.15, -1.04 \pm 0.1	-6.04 \pm 0.54			-2.62 \pm 0.11	2.31 \pm 0.31
04292+2422(W)						0.84 \pm 0.16	9.02 \pm 1.18
04295+2251				-4.17 \pm 0.70	-6.85 \pm 0.17	-1.10 \pm 0.08	5.02 \pm 1.45
04315+3617	-58.21 \pm 2.61				-0.14 \pm 0.08	-10.22 \pm 0.43	
04325+2402				-4.55 \pm 0.69	-1.54 \pm 0.10	-3.01 \pm 0.12	
04365+2535				-9.96 \pm 0.71	-1.65 \pm 0.07	-4.49 \pm 0.16	3.24 \pm 1.14
04369+2539		2.24 \pm 0.28, -3.74 \pm 0.25	-12.26 \pm 0.60			-5.59 \pm 0.10	-13.80 \pm 0.44
04381+2540				-13.81 \pm 3.33	-6.65 \pm 0.49	-2.30 \pm 0.18	6.02 \pm 0.61
04530+5126	-12.42 \pm 0.18	3.17 \pm 0.07, -0.93 \pm 0.05	-3.89 \pm 0.14			-2.47 \pm 0.10	7.97 \pm 0.52
04591-0856					-2.12 \pm 0.09	-1.41 \pm 0.21	10.88 \pm 0.91

Table 4—Continued

IRAS	CaII (0.866 μm)	He I (1.083 μm) ^a	Pa β (1.282 μm)	[Fe II] (1.644 μm)	H ₂ (2.122 μm)	Br γ (2.166 μm)	CO (2.293 μm)
05155+0707				-7.35 \pm 1.48	-7.63 \pm 0.23	-3.62 \pm 0.16	
05256+3049				-8.03 \pm 0.60	-8.66 \pm 0.23	-6.87 \pm 0.34	-38.83 \pm 1.51
05289–0430(E)	-16.58 \pm 2.87	-6.15 \pm 1.17	-10.52 \pm 0.94	-3.99 \pm 0.36	-0.98 \pm 0.14	-2.85 \pm 0.08	
05302–0537					-17.63 \pm 0.19	-2.90 \pm 0.16	-2.39 \pm 0.49
05311–0631						-2.79 \pm 0.10	1.17 \pm 0.30
05320–0300						0.89 \pm 0.28	7.78 \pm 0.99
05327–0457(W)						6.32 \pm 0.49	1.35 \pm 0.46
05357–0650		0.68 \pm 0.07, -0.42 \pm 0.09				-0.72 \pm 0.04	
05375–0040(1)	-3.09 \pm 0.30	3.74 \pm 0.30, -4.11 \pm 0.58	-8.86 \pm 0.30			-2.59 \pm 0.07	2.43 \pm 0.17
05375–0040(2)	-6.64 \pm 1.16	0.87 \pm 0.21, -2.56 \pm 0.20	-4.91 \pm 0.27			-1.61 \pm 0.08	5.58 \pm 0.36
05375–0040(3)	-13.27 \pm 1.30	2.38 \pm 0.35, -1.73 \pm 0.27				-5.77 \pm 0.07	2.09 \pm 0.42
05378–0750(E)				-5.80 \pm 0.92		-3.39 \pm 0.13	-7.51 \pm 1.04
05379–0758(1)					-0.47 \pm 0.12	-6.10 \pm 0.10	-6.67 \pm 0.83
05379–0758(2)						-2.35 \pm 0.19	7.76 \pm 0.69
05379–0758(3)						-0.87 \pm 0.23	
05384–0808(1)						-1.80 \pm 0.14	5.49 \pm 0.59
05384–0808(3)					-0.93 \pm 0.20	-2.73 \pm 0.15	5.27 \pm 0.58
05391–0841(N)						-4.73 \pm 0.15	3.25 \pm 0.79
05391–0841(S)						-3.23 \pm 0.09	
05403–0818			-11.21 \pm 2.09	-26.46 \pm 1.43	-3.09 \pm 0.09	-5.28 \pm 0.13	-18.67 \pm 1.54
05404–0948						6.99 \pm 0.31	2.28 \pm 0.71
05405–0117					-1.11 \pm 0.12	-3.06 \pm 0.20	0.94 \pm 0.91
05427–0116						-0.26 \pm 0.28	8.28 \pm 1.19
05450+0019							29.21 \pm 1.22
05513-1024	-1.65 \pm 0.12	3.62 \pm 0.10	-4.92 \pm 0.08			-2.02 \pm 0.10	-5.64 \pm 0.83
05555–1405(N)	-13.16 \pm 2.27	-6.07 \pm 0.94	-15.92 \pm 0.34		-0.61 \pm 0.10	-8.14 \pm 0.13	
05555–1405(S)	-6.17 \pm 0.77	-14.56 \pm 0.81	-3.49 \pm 0.34	-1.77 \pm 0.44	-0.58 \pm 0.09	-1.09 \pm 0.08	3.93 \pm 0.63
05598–0906(1)			-20.75 \pm 3.67		-0.27 \pm 0.07	-10.54 \pm 0.09	-10.44 \pm 0.71
06047–1117				-4.89 \pm 0.57	-1.56 \pm 0.44	-10.45 \pm 0.16	-62.73 \pm 3.48
06297+1021(E)			-5.97 \pm 0.71	-1.40 \pm 0.34	-0.22 \pm 0.08	-2.14 \pm 0.07	-2.17 \pm 1.13
06297+1021(W)	-7.65 \pm 0.54	12.37 \pm 0.23				-3.44 \pm 0.26	-10.65 \pm 0.50
06382+1017					-21.92 \pm 1.33		1.64 \pm 6.33
06393+0913						0.70 \pm 0.26	19.87 \pm 1.52
07018–1005(1)					-1.55 \pm 0.39	-3.70 \pm 0.15	-49.27 \pm 2.62
07025–1204(2)							1.21 \pm 0.64

Table 4—Continued

IRAS	CaII (0.866 μm)	He I (1.083 μm) ^a	Pa β (1.282 μm)	[Fe II] (1.644 μm)	H ₂ (2.122 μm)	Br γ (2.166 μm)	CO (2.293 μm)
07180–2356				-34.36 \pm 2.32	-7.01 \pm 0.21	-1.46 \pm 0.19	-22.60 \pm 1.37
16235–2416						4.62 \pm 0.21	2.46 \pm 0.44
16240–2430(E)					-0.25 \pm 0.04	-3.85 \pm 0.19	
16240–2430(W)			-7.59 \pm 1.77			-8.09 \pm 0.08	-51.70 \pm 2.06
16288–2450(E)					-0.66 \pm 0.17	-1.13 \pm 0.18	2.50 \pm 0.52
16288–2450(W1)			-6.29 \pm 0.57			-2.71 \pm 0.18	1.89 \pm 0.26
16288–2450(W2)						-1.57 \pm 0.45	10.90 \pm 0.77
16289–4449	-10.68 \pm 1.41	14.72 \pm 0.48			-0.91 \pm 0.14	-2.26 \pm 0.11	-16.76 \pm 0.68
16316–1540		-4.29 \pm 0.33			-0.84 \pm 0.08	-0.64 \pm 0.07	6.13 \pm 0.47
16442–0930				-5.92 \pm 0.71	-1.83 \pm 0.07	-2.99 \pm 0.34	1.69 \pm 0.74
18250–0351		2.90 \pm 0.24, -3.95 \pm 0.23	-127.74 \pm 1.09			-23.20 \pm 0.06	
18270–0153(6)				-11.39 \pm 1.56		0.35 \pm 0.11	3.47 \pm 1.08
18270–0153(1)					-1.08 \pm 0.46	0.58 \pm 0.23	32.17 \pm 2.80
18274–0212					-50.41 \pm 0.73	-4.35 \pm 0.25	-17.92 \pm 1.57
18275+0040	-3.22 \pm 0.62	-6.65 \pm 0.46	-4.18 \pm 0.15			-1.83 \pm 0.08	
18278–0212(N)						-1.16 \pm 0.27	
18278–0212(S)						-2.12 \pm 0.35	0.77 \pm 0.93
18341–0113(N)		2.65 \pm 0.40				-1.66 \pm 0.55	13.54 \pm 1.48
18341–0113(S)				-3.79 \pm 1.19	-0.72 \pm 0.28		7.03 \pm 1.59
18383+0059(E)						-8.11 \pm 0.16	1.70 \pm 0.64
18383+0059(W)					-1.27 \pm 0.20	-4.83 \pm 0.20	1.33 \pm 0.60
18577–3701	-31.14 \pm 0.39	1.52 \pm 0.07, -1.45 \pm 0.09	-18.50 \pm 0.24			-6.50 \pm 0.07	0.73 \pm 0.48
18585–3701(E)		-5.60 \pm 1.02	-11.79 \pm 0.23			-2.27 \pm 0.17	
18585–3701(W)	-14.39 \pm 1.28	-5.44 \pm 0.33	-14.06 \pm 0.29			-2.93 \pm 0.08	
19266+0932		3.36 \pm 0.56				-0.18 \pm 0.28	14.74 \pm 1.94
20355+6343			-3.79 \pm 0.67	-1.06 \pm 0.21		-1.65 \pm 0.10	1.57 \pm 0.89
20377+5658			-4.70 \pm 0.24			-2.73 \pm 0.12	-23.32 \pm 1.27
20453+6746	-38.56 \pm 4.06		-31.98 \pm 1.05		-0.48 \pm 0.13	-6.40 \pm 0.13	-14.14 \pm 0.95
20568+5217							23.61 \pm 1.20
21352+4307				-6.29 \pm 0.77	-3.70 \pm 0.08	-4.07 \pm 0.19	-7.59 \pm 1.00
21445+5712				-5.04 \pm 0.39	-7.99 \pm 0.07	-0.63 \pm 0.12	0.78 \pm 0.31
21454+4718		10.41 \pm 0.30				-0.94 \pm 0.34	29.03 \pm 1.57
21569+5842					-1.18 \pm 0.06	-5.12 \pm 0.08	-7.84 \pm 0.52
22051+5848				-6.47 \pm 1.21	-1.51 \pm 0.50		36.67 \pm 1.69
22176+6303				-1.20 \pm 0.30		-2.70 \pm 0.15	-4.36 \pm 0.77

Table 4—Continued

IRAS	CaII (0.866 μm)	He I (1.083 μm) ^a	Pa β (1.282 μm)	[Fe II] (1.644 μm)	H ₂ (2.122 μm)	Br γ (2.166 μm)	CO (2.293 μm)
22266+6845			-5.06 \pm 0.60	-1.77 \pm 0.38	-2.15 \pm 0.09	-1.82 \pm 0.08	2.72 \pm 0.85
22272+6358(E)			-8.76 \pm 0.77			-2.42 \pm 0.09	-5.04 \pm 0.68
F22324+4024	-6.59 \pm .21	3.01 \pm 0.14, -0.92 \pm 0.14		-1.64 \pm 0.18	-0.42 \pm 0.08	-2.19 \pm 0.06	
23037+6213					-0.32 \pm 0.08	-2.90 \pm 0.09	
F23591+4748		-6.95 \pm 1.36	-6.57 \pm 0.43		-0.70 \pm 0.14	-2.81 \pm 0.19	4.58 \pm 0.48

^aThe He I line is often seen in emission and absorption simultaneously, in which case positive and negative equivalent width values are given for the absorption and emission components.

Table 5. Nebulosity and Spectral Category

	#	% ^a
Group 1: Strong Nebulosity		
Low veiling	1/15	6.7% ^{+13.6%} _{−5.5%}
High veiling	8/15	53.3% ^{+15.2%} _{−15.8%}
FU Ori	6/15	40.0% ^{+16.1%} _{−14.5%}
Group 2: Some Nebulosity		
Low veiling	19/41	46.3% ^{+8.9%} _{−8.7%}
High veiling	19/41	46.3% ^{+8.9%} _{−8.7%}
FU Ori	3/41	7.3% ^{+6.6%} _{−3.9%}
Group 3: No Nebulosity		
Low veiling	29/54	53.7% ^{+7.5%} _{−7.7%}
High veiling	24/54	44.4% ^{+7.7%} _{−7.5%}
FU Ori	1/54	1.9% ^{+4.1%} _{−1.5%}

^a1 σ uncertainties are presented, derived using binomial statistics with the calculator at <http://statpages.org/confint.html>

Table 6. FU Ori and FU Ori-like Objects, and Objects with Excess CO Absorption

IRAS	CO (\AA) ^a	L_{bol} (L_{\odot})	Notes
04073+3800	26.73	22.6	known FU Ori
04108+2803W	11.74	0.7	known YSO, no association as an FU Ori
04286+1801W	19.43	20.2	known FU Ori
04292+2422W	9.02		excess CO absorption for G0-M3 star
04591-0856	10.87	0.90	excess CO absorption for K4-M3 type
05327-0457W	1.19		excess CO absorption for A0-F7 star
05404-0948	2.29		excess CO absorption for A5-F3 star
05450+0019	29.20	27.6	new FU Ori
06393+0913	19.86	8.9	excess CO absorption for G0-M0 star
16235-2416	2.46		excess CO absorption for A3-F4 star
16289-4449	-17.45	5.9	known FU Ori
18270-0153W	32.17		new FU Ori
18341-0113N	13.54		excess CO absorption for K0-M4 type
18341-0113S			new FU Ori?
19266+0932	14.74	3.4	known FU Ori
20568+5217	23.61	45.6	known FU Ori
21454+4718	29.03	106.7	known FU Ori
22051+5848	36.67	73.0	known FU Ori

^aCO equivalent width in Angstroms

Table 7. Binary Properties

IRAS	D(pc)	r('')	r(AU) ^a	ΔK	Veiling
03220+3035	290	1.37	397	0.26	mixed
F04108+2804	140	21.64	3029	0.69	low
F04113+2758	140	3.97	555	0.07	low
F04189+2650	140	19.75	2765	3.75	mixed
05375-0040	470	6.40	3008	1.77	low
				0.94	low
F05391-0841	480	9.49	4555	0.05	high
16288-2450	160	2.98	476	0.84	low
18278-0212	600	4.47	2682	0.57	high
18383+0059		2.15		1.11	high

^aProjected separation on the sky